Physik-Department

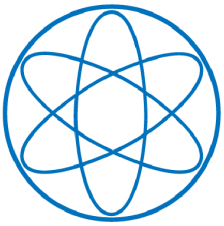

The neutrino experiment Double Chooz and data analysis with the near detector

Dissertation

von

Michael Franke

Technische Universität München

Technische Universität München
Physik-Department
Lehrstuhl für Experimentalphysik und Astroteilchenphysik
Univ.-Prof. Dr. Lothar Oberauer

The neutrino experiment Double Chooz and data analysis with the near detector

Michael Werner Franke

Vollständiger Abdruck der von der Fakultät für Physik der Technischen Universität München zur Erlangung des akademischen Grades eines

Doktors der Naturwissenschaften (Dr. rer. nat.)

genehmigten Dissertation.

Vorsitzender:		Univ.-Prof. Dr. Alejandro Ibarra
Prüfer der Dissertation:	1.	Univ.-Prof. Dr. Lothar Oberauer
	2.	Univ.-Prof. Dr. Peter Fierlinger

Die Dissertation wurde am 01.02.2016 bei der Technischen Universität München eingereicht und durch die Fakultät für Physik am 07.03.2016 angenommen.

Zusammenfassung

Während der letzten Jahre gab es beachtliche Fortschritte auf dem Gebiet der Neutrinophysik. Neutrinooszillationen sind nachgewiesen und fast alle zugehörigen Parameter sind präzise bestimmt. Nur eine mögliche CP-verletzende Phase ist noch unbekannt. Ein Experiment, das den Mischungswinkel θ_{13} präzise vermessen hat, ist das Reaktorneutrino-Experiment Double Chooz. Die Reaktorneutrinos werden mit Hilfe des inversen Betazerfalls in zwei Detektoren nachgewiesen. Noch vor ein paar Jahren war für θ_{13} nur eine obere Grenze bekannt. Double Chooz war das erste Reaktorneutrino-Experiment, das einen endlichen Wert für θ_{13} präsentieren konnte. Der Wert für $\sin^2 2\theta_{13}$ aus der aktuellsten Publikation beträgt $0{,}090^{+0{,}032}_{-0{,}029}$.
Im Rahmen dieser Arbeit wurde eine Infrastruktur für das Füllen des nahen Double Chooz Detektors eingerichtet und 190 m^3 Detektorflüssigkeit erfolgreich vorbereitet. Der Füllprozess wurde optimiert um einen effizienten Ablauf zu gewährleisten. Die Fülldauer konnte auf nur 22 Tage reduziert werden. Verglichen mit der Fülldauer von 2 Monaten für den fernen Detektor, stellt dies eine deutliche Verbesserung dar. Die Entwicklung eines neuartigen Füllstandsmesssystems war ebenso Teil dieser Arbeit. Wegen der Leistungsfähigkeit des Füllstandsmesssystems wurden die strengen Grenzwerte, die die Sicherheit des Double Chooz Detektors garantierten, während allen Phasen des Füllprozesses eingehalten. Mehrere Ausfälle der Stromversorgung und der Netzwerkverbindung bereiteten dem System keine Probleme und keine Daten gingen verloren. Diese Vorfälle und die Möglichkeit einfacher Wartung und Reparatur, beweisen den Erfolg des Designkonzepts für das neue Füllstandsmesssystem.
Für diese Arbeit wurden Daten des nahen Detektors, mit einer Gesamtdauer von 110,4 Tagen, verwendet. Mit Hilfe von BiPo-Koinzidenzen konnten die Massenkonzentrationen von Uran und Thorium bestimmt werden. BiPo-Koinzidenzen sind Ereignisse, die durch den Betazerfall von ^{214}Bi und ^{212}Bi, gefolgt von einem Alphazerfall von ^{214}Po und ^{212}Po, ausgelöst werden. Diese beiden Zerfälle formen eine schnelle, räumlich zusammenhängende Koinzidenz und sind damit einfach von anderen Untergrundereignissen zu unterscheiden. Da eine konstante Rate von BiPo-Koinzidenzen gefunden wurde, ist vom radioaktiven Gleichgewicht in der Uran- und Thorium-Zerfallsreihe auszugehen. Des Weiteren wurden die α-Quenchingfaktoren für den Gamma Catcher und den Neutrino Target Flüssigszintillator bestimmt. Für eine α-Energie von 7,687 MeV beträgt der Wert $12{,}27 \pm 0{,}02$ im Gamma-Catcher und $9{,}63 \pm 0{,}04$ im Neutrino Target. Schlussendlich wurden die Massenkonzentrationen von Uran und Thorium im nahen Double Chooz Detektor berechnet. Im inneren Teil des Detektors beträgt die Massenkonzentration von Uran $(1{,}09 \pm 0{,}03) \cdot 10^{-14}\,\mathrm{g/g}$ und die von Thorium $(9{,}76 \pm 0{,}27) \cdot 10^{-14}\,\mathrm{g/g}$. Die berechneten Werte können in eine (α,n)-Untergrundrate umgerechnet werden. Es konnte festgestellt werden, dass dieser Betrag deutlich kleiner ist als alle weiteren Untergrundbeiträge. Dies beweist die radioaktive Reinheit des nahen Double Chooz Detektors.

Abstract

During the last years there has been a huge progress in the field of neutrino physics. Neutrino oscillations are well established and almost all parameters, except a possible CP-violating phase, are determined to high precision. One experiment providing a precise measurement of the neutrino mixing angle θ_{13} is the Double Chooz reactor antineutrino experiment. The reactor antineutrinos are detected via the inverse beta decay in two identical liquid scintillator based detectors. A few years ago, the value of θ_{13} was unknown and only an upper limit existed. Double Chooz was the first reactor antineutrino experiment presenting a result for a nonzero value of θ_{13}. The value for $\sin^2 2\theta_{13}$ from the latest Double Chooz publication is $0.090^{+0.032}_{-0.029}$.

As part of this thesis, an infrastructure for filling the Double Chooz near detector was established and 190 m^3 of detector liquids were prepared successfully. The filling process was optimized to allow an efficient filling of the near detector. The total operation time was reduced to only 22 days. Compared to the far detector filling time of 2 months, this is a great improvement. The development of a completely new level measurement system was as well part of this thesis. Due to the excellent performance of the level measurement system, the hard restrictions for the safety of the Double Chooz detector were met during the entire filling process. Several power glitches and network failures did not harm the system and did not result in any loss of data. These irregularities and the simple maintenance and repair possibilities certify the success of the design concept for the new level measurement system.

For this thesis, data from the Double Chooz near detector with a total live time of 110.4 days was used. The mass concentrations of uranium and thorium in the near detector were determined using BiPo coincidences. These events originate from the β-decay of ^{214}Bi and ^{212}Bi followed by the α-decay of ^{214}Po and ^{212}Po respectively. This technique provides a fast coincidence between β^- and α signals, which is also spatially correlated and can easily be distinguished from other background. A constant rate of BiPo coincidences was found in both cases, indicating radioactive equilibrium in the uranium and thorium decay chains. Furthermore, the α quenching factors for the gamma catcher and the neutrino target liquid scintillator were calculated. The determined values for an α energy of 7.687 MeV are 12.27 ± 0.02 in the gamma catcher and 9.63 ± 0.04 in the neutrino target. Finally, the mass concentrations of uranium and thorium in the Double Chooz near detector were calculated. For the inner detector the uranium concentration was found to be $(1.09 \pm 0.03) \cdot 10^{-14}$ g/g, while for thorium the corresponding value is $(9.76 \pm 0.27) \cdot 10^{-14}$ g/g. These numbers can be translated into an (α,n) background rate which is found to be far below all other background contributions. This proves the high radiopurity of the Double Chooz near detector.

Contents

Chapter 1

1 Introduction into neutrino physics

1.1 Prediction and discovery of neutrinos

In 1930, Wolfgang Pauli predicted a particle, which was unknown at this time. The particle is needed to preserve energy- and momentum-conservation during the β-decay

$$n \rightarrow p + e^- + \bar{\nu}_e$$

process [Pau30]. On December 4th, 1930 Pauli wrote an open letter to his colleagues, which he addressed to as the "group of radioactives". They participated at a conference in Tübingen and he explained the necessity of an extra particle. The extra particle is needed to explain the measured continuous spectra instead of the expected discrete spectra of two-body decay in the case of β-decay.

> *"... es könnten elektrisch neutrale Teilchen, die ich Neutronen nennen will, in den Kernen existieren, welche den Spin 1/2 haben [...] und sich von Lichtquanten ausserdem noch dadurch unterscheiden, dass sie nicht mit Lichtgeschwindigkeit laufen."* [Pau30]

Enrico Fermi, who worked on a theory for properties and interaction of neutrons at this time, coined the name "neutrino" for the particle postulated by Pauli. The name is coming from the Italian diminutive *-ino* for small neutron [Lan07]. The term postulated by Pauli persisted for the nuclear component found in 1932.
It took time until the year 1933, before Pauli discussed his idea of neutrinos in public after a talk from Werner Heisenberg at the 7th Solvay conference in Brussels [Rec33]. For another period of 23 years later, in 1956, the electron antineutrino $\bar{\nu}_e$ was found in an experiment at the first big nuclear power reactor. Clyde Cowan and Frederick Reines were able to prove the existence using the inverse β-decay [Rei56]. In 1995, Reines was awarded with the nobel price in physics for this achievement.

1st generation	2nd generation	3rd generation
ν_e electron neutrino	ν_μ muon neutrino	ν_τ tau neutrino
e electron	μ muon	τ tau

Table 1.1: Group of leptons in the standard model of nuclear and particle physics: Neutrinos have no electrical charge and no mass. Electron, muon and tau particles have charge number -1 respectively.

The discovery of the muon neutrino ν_μ followed 1963 [Dan62] at Brookhaven National Laboratory. It took time until 2000 before the experimental discovery of the tau neutrino ν_τ followed by the DONUT experiment at Fermilab [Don01].
The standard model of nuclear and particle physics classifies the neutrinos as massless particles in the group of leptons (see table 1.1) [Hal84]. There are three groups of leptons (called generations) which are ordered by increasing mass. All of them are fermions with spin $1/2$ and are described with Fermi-Dirac statistics. For every lepton there is the corresponding antiparticle with inverted electrical charge.
During the sixties, there were hints of an incomplete description, provided by the standard model: An experiment by Raymond Davis, who measured the flux of solar neutrinos with a chloride detector at Homestake mine, showed a deficit in the solar neutrino flux. The flux of electron neutrinos ν_e coming from fission processes in the sun had less then half of the expected intensity compared to expectation [Dav68].
The most reasonable explanation for the solar flux deficit were errors in models describing the sun and its fission processes. On the other hand, if one assumes a nonzero neutrino mass, in conflict to the standard model, there is the possibility for changes in the neutrino flavor during propagation (see section 1.2 for a detailed explanation). Since the total number of neutrinos is conserved, more than half of the emitted solar electron neutrinos have changed to muon or tau neutrinos, in the case of Davis' experiment. A first experimental evidence for neutrino oscillations was presented on the NEUTRINO '98 conference [Kaj99] and was finally confirmed by the SNO collaboration in 2002 [Sno02]. The Nobel Prize in physics was awarded in 2015 to Takaaki Kajita and Arthur B. McDonald for this achievements [Nob15].

1.2 Theory of neutrino oscillations

A possible theoretical description of neutrino oscillations is a method from Pontecorvo, Maki, Nakagawa and Sakata (abbreviated PMNS) [Mak62]. The neutrinos $(\nu_e, \nu_\mu, \nu_\tau)$ in the group of leptons mentioned above are eigenstates of the weak interaction, so called flavor eigenstates. Flavor eigenstates are important for production

or detection of neutrinos, because they are, besides gravitational interaction, only weakly interacting. They can travel long distances in matter, which makes the detection in neutrino experiments difficult. Furthermore there are the mass eigenstates (ν_1, ν_2, ν_3), which are important for the propagation of neutrinos. Experiments have shown that there is a difference between flavor and mass eigenstates of neutrinos [Ber12]. This suggests to introduce a mixing matrix[1] for the correlation between mass and flavor eigenstates:

$$\begin{pmatrix} \nu_e \\ \nu_\mu \\ \nu_\tau \end{pmatrix} = \begin{pmatrix} U_{e1} & U_{e2} & U_{e3} \\ U_{\mu 1} & U_{\mu 2} & U_{\mu 3} \\ U_{\tau 1} & U_{\tau 2} & U_{\tau 3} \end{pmatrix} \begin{pmatrix} \nu_1 \\ \nu_2 \\ \nu_3 \end{pmatrix} \tag{1.1}$$

In the case of three different flavors, the 3×3 mixing matrix can be described with three mixing angles $\theta_{12}, \theta_{13}, \theta_{23}$ with the properties $0 \leq \theta_{ij} \leq \frac{\pi}{2}$, one CP-violating phase δ and two Majorana-Phases α_1, α_2. For the three mixing angles, one can choose the three Euler-Angles of a rotation in $\mathbb{R}^3$ space. This leads to the following representation of the PMNS-Matrix [Eid04]:

$$\begin{aligned} \begin{pmatrix} U_{e1} & U_{e2} & U_{e3} \\ U_{\mu 1} & U_{\mu 2} & U_{\mu 3} \\ U_{\tau 1} & U_{\tau 2} & U_{\tau 3} \end{pmatrix} &= \begin{pmatrix} 1 & 0 & 0 \\ 0 & \cos\theta_{23} & \sin\theta_{23} \\ 0 & -\sin\theta_{23} & \cos\theta_{23} \end{pmatrix} \begin{pmatrix} \cos\theta_{13} & 0 & \sin\theta_{13} e^{-i\delta} \\ 0 & 1 & 0 \\ -\sin\theta_{13} e^{i\delta} & 0 & \cos\theta_{13} \end{pmatrix} \\ &\times \begin{pmatrix} \cos\theta_{12} & \sin\theta_{12} & 0 \\ -\sin\theta_{12} & \cos\theta_{12} & 0 \\ 0 & 0 & 1 \end{pmatrix} \begin{pmatrix} e^{\frac{i}{2}\alpha_1} & 0 & 0 \\ 0 & e^{\frac{i}{2}\alpha_2} & 0 \\ 0 & 0 & 1 \end{pmatrix} \end{aligned} \tag{1.2}$$

In the following the two Majorana-Phases α_1, α_2 will be neglected, because they have no effect on the oscillation probablility. This gives a reduced representation for the mixing matrix:

$$U_{\alpha i} = \begin{pmatrix} c_{12}c_{13} & s_{12}c_{13} & s_{13}e^{-i\delta} \\ -s_{12}c_{23} - c_{12}s_{23}s_{13}e^{i\delta} & c_{12}c_{23} - s_{12}s_{23}s_{13}e^{i\delta} & s_{23}c_{13} \\ s_{12}s_{23} - c_{12}c_{23}s_{13}e^{i\delta} & -c_{12}s_{23} - s_{12}c_{23}s_{13}e^{i\delta} & c_{23}c_{13} \end{pmatrix} \tag{1.3}$$

Here, $\sin(\theta_{ij})$ and $\cos(\theta_{ij})$ are abbreviated as s_{ij} and c_{ij} respectively. The flavor eigenstates (indices $\alpha = \mathrm{e}, \mu, \tau$) are consisting of a linear combination of mass eigenstates (indices $i = 1, 2, 3$). Therefore equation 1.1 can be written as:

$$|\nu_\alpha\rangle = \sum_{i=1}^{3} U_{\alpha i} |\nu_i\rangle \tag{1.4}$$

For antineutrinos one needs the complex conjugated matrix $U^*_{\alpha i}$ accordingly:

$$\overline{|\nu_\alpha\rangle} = \sum_{i=1}^{3} U^*_{\alpha i} |\nu_i\rangle \tag{1.5}$$

[1] PMNS-Matrix, similar to the CKM-Matrix for quark mixing

In the following, natural units will be used[2]. The time evolution of mass eigenstates can be written as [Bil03]:

$$|\nu_i(t)\rangle = e^{-iE_i t}\,|\nu_i(t=0)\rangle \tag{1.6}$$

The neutrino energy E_i can be approximated under the assumption of a low mass m_i which leads to $m_i \ll |\vec{p}_i|$ and $|\vec{p}_i| \approx E_{\nu_i}$:

$$E_i = \sqrt{\vec{p}_i{}^2 + m_i^2} \approx |\vec{p}_i| + \frac{m_i^2}{2|\vec{p}_i|} \approx E_{\nu_i} + \frac{m_i^2}{2E_{\nu_i}} \tag{1.7}$$

Inserting equation 1.6 in equation 1.4 leads to the time propagation of flavor eigenstates:

$$|\nu_\alpha(t)\rangle = \sum_{i=1}^{3} U_{\alpha i} e^{-iE_i t}\,|\nu_i(t=0)\rangle \tag{1.8}$$

For the transition $\nu_\alpha \to \nu_\beta$, the transition amplitude is the projection of the time propagated state $|\nu_\alpha(t)\rangle$ to the state $\langle\nu_\beta|$:

$$A_{\alpha\to\beta} = \langle\nu_\beta|\nu_\alpha(t)\rangle = \sum_{i,j=1}^{3} U_{\alpha i} U^*_{\beta j}\delta_{ij} e^{-iE_i t} = \sum_{i=1}^{3} U_{\alpha i} U^*_{\beta i} e^{-iE_i t} \tag{1.9}$$

This is possible because the eigenstates $|\nu_i\rangle$ form a orthonormal basis, that means $\langle\nu_i|\nu_j\rangle = \delta_{ij}$. The transition probability $P_{\nu_\alpha\to\nu_\beta}$ is defined by the absolute square of the transition amplitude. After some transformations, the probability can be written as:

$$\begin{aligned} P_{\nu_\alpha\to\nu_\beta} = |A_{\alpha\to\beta}|^2 = \delta_{\alpha\beta} &- 4\sum_{k>j} \mathrm{Re}\left(U_{\alpha k}U^*_{\beta k}U^*_{\alpha j}U_{\beta j}\right)\sin^2(\Delta_{kj}) \\ &- 2\sum_{k>j} \mathrm{Im}\left(U_{\alpha k}U^*_{\beta k}U^*_{\alpha j}U_{\beta j}\right)\sin(2\Delta_{kj}) \end{aligned} \tag{1.10}$$

with

$$2\Delta_{ij} = (E_i - E_j)t = \frac{m_i^2 - m_j^2}{2E}t = \Delta m^2_{ij}\frac{L}{2E} \tag{1.11}$$

which is true for $L = t$ and under the assumption that all mass eigenstates have the same momentum $|\vec{p}_i| \approx E_{\nu_i} \approx E$. There are two independent squared mass differences $\Delta m^2_{31}, \Delta m^2_{21}$:

$$\begin{aligned} \Delta m^2_{31} &= m_3^2 - m_1^2 \\ \Delta m^2_{21} &= m_2^2 - m_1^2 \end{aligned} \tag{1.12}$$

[2] that means $c = \hbar = k_B = 1$

The third squared mass difference Δm^2_{32} can be expressed by Δm^2_{31} and Δm^2_{21}:

$$\Delta m^2_{32} = \Delta m^2_{31} - \Delta m^2_{21} \tag{1.13}$$

$\Delta_{32} = \Delta_{31} - \Delta_{21}$ from equation 1.10 can be eliminated with this definition. Now one can calculate the survival probability $\bar{\nu}_e \to \bar{\nu}_e$, that means the probability to detect electron antineutrinos $\bar{\nu}_e$ with energy E still as electron antineutrinos $\bar{\nu}_e$ after traveling the distance L:

$$\begin{aligned} P_{\bar{\nu}_e \to \bar{\nu}_e} = 1 &- 4|U_{e2}|^2(1-|U_{e2}|^2)\sin^2\Delta_{21} - 4|U_{e3}|^2(1-|U_{e3}|^2)\sin^2\Delta_{31} \\ &+ 2|U_{e2}|^2|U_{e3}|^2\left(4\sin^2\Delta_{21}\sin^2\Delta_{31} + \sin 2\Delta_{21}\sin 2\Delta_{31}\right) \end{aligned} \tag{1.14}$$

After inserting the PNMS-Matrix elements, the oscillation formula reads as follows:

$$\begin{aligned} P_{\bar{\nu}_e \to \bar{\nu}_e} = 1 &- \sin^2(2\theta_{13})\left(c^2_{12}\sin^2\frac{\Delta m^2_{31}L}{4E} + s^2_{12}\frac{\Delta m^2_{32}L}{4E}\right) \\ &- c^4_{13}\sin^2(2\theta_{12})\sin^2\left(\frac{\Delta m^2_{21}L}{4E}\right) \end{aligned} \tag{1.15}$$

Obviously oscillations are only possible for $\Delta m_{ij} \neq 0$. In other words, if neutrino oscillations are observed, this is a proof for at least one mass eigenstate having a nonzero mass.
Further conclusions from the oscillation formula 1.15:

- The mixing angles are defining the oscillation amplitude.
- The squared mass differences are defining the oscillation length.

The current best experimental values for the neutrino oscillation parameters are summarized in table 1.2. Measured or detected are the following properties [Alt14]:

- existence of three neutrino flavors
- neutrino mixing, respectively oscillation of these three flavors
- request of nonzero neutrino masses
- value of the two independent squared mass differences
- $m_2 > m_1$ known due to the MSW-Effect[3] in the sun
- values of all three mixing angles

Open questions and part of current research are:

[3] Mikheyev-Smirnov-Wolfenstein-Effect, refer to [Aha00]

parameter	value	source
$\sin^2(2\theta_{12})$	$0.846^{+0.021}_{-0.021}$	KamLAND [Gan13]
Δm^2_{21}	$7.53^{+0.18}_{-0.18} \cdot 10^{-5}\,\mathrm{eV}^2$	
$\sin^2(2\theta_{23})$	$0.999^{+0.001}_{-0.018}$	T2K [Abe14a]
$\lvert\Delta m^2_{32}\rvert$	$2.44^{+0.06}_{-0.06} \cdot 10^{-3}\,\mathrm{eV}^2$	PDG [Oli14]
$\sin^2(2\theta_{13})$	$0.093^{+0.008}_{-0.008}$	

Table 1.2: Current values for the neutrino oscillation parameters [Oli14]. For $\sin^2(2\theta_{23})$ and $|\Delta m^2_{32}|$ the values for normal hierarchy are quoted. The positive sign of Δm^2_{21}, i.e. $m_2 > m_1$, is known due to the MSW-Effect [Aha00] in the sun. The CP-violating phase δ and the sign of Δm^2_{32} remain unknown.

- hierarchy of neutrino masses (see figure 1.1),
- angle octant of θ_{23}, i.e. if θ_{23} is lower or higher than 45°
- absolute value of neutrino masses
- possible violation of CP symmetry, i.e. $\delta \neq 0°$ or 180°
- question of the Majorana or Dirac character of neutrinos
- possibility for the existence of sterile neutrinos as a consequence of the possible existence of more than three mass eigenstates [Aba12]

The parameters of neutrino oscillation have partly strongly different values (two orders of magnitude between Δm^2_{21} und Δm^2_{32}). Therefore one has to expect different properties for different scales of oscillation length and experiment type, which will be discussed in the following.
If one assumes $\delta = 0°$ for the CP violating phase and uses the current values for the mixing angles from table 1.2

mixing angle	value
θ_{12}	33.4°
θ_{13}	8.9°
θ_{23}	44.1°

for the PMNS-Matrix, the following values are obtained:

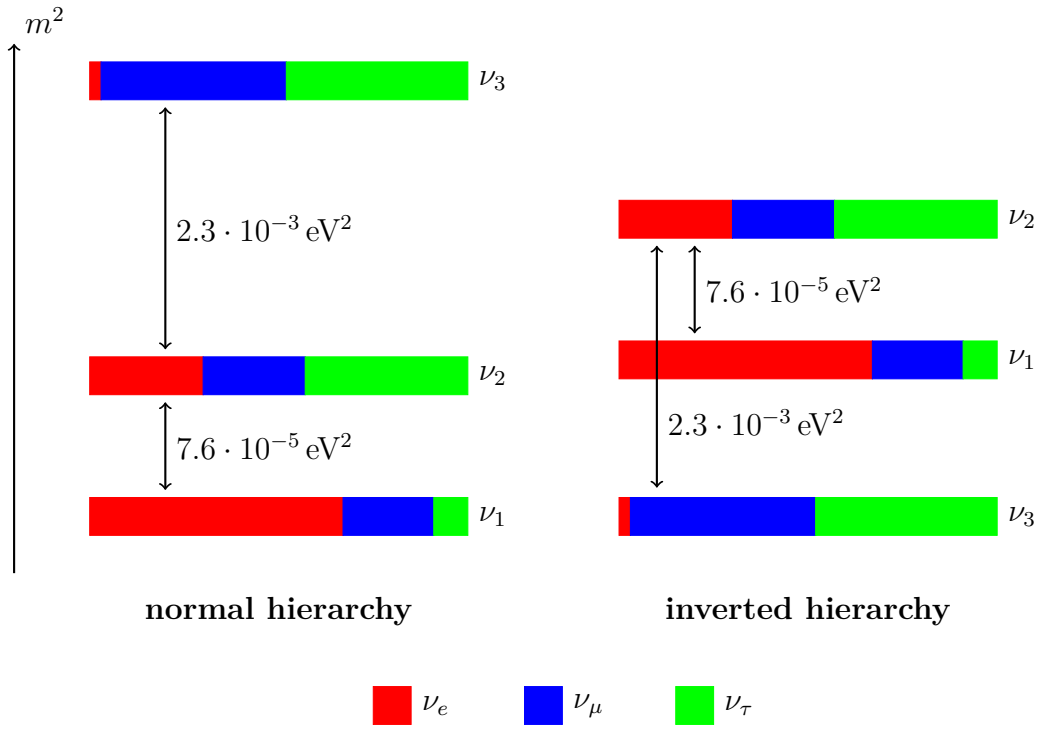

Figure 1.1: Normal and inverted hierarchy for the mass eigenstates of neutrinos. Because of the MSW-effect in the sun [Aha00] it is known that $m_2 > m_1$, whereas the sign of Δm^2_{32} is still unknown. Therefore two solutions for the mass hierarchy are existing. Also the absolute values of the eigenstates are still unknown. Since the mass eigenstates are linear combinations of the flavor eigenstates, the composition of every mass eigenstate is depicted with colors.

$$\begin{pmatrix} \nu_e \\ \nu_\mu \\ \nu_\tau \end{pmatrix} = \begin{pmatrix} 0.82 & 0.54 & 0.15 \\ -0.49 & 0.54 & 0.69 \\ 0.29 & -0.64 & 0.71 \end{pmatrix} \begin{pmatrix} \nu_1 \\ \nu_2 \\ \nu_3 \end{pmatrix} \tag{1.16}$$

In figure 1.1 the composition of every mass eigenstate (ν_1, ν_2, ν_3) as a linear combination of the flavor eigenstates $(\nu_e, \nu_\mu, \nu_\tau)$ is shown. Because of the unknown sign of the squared mass difference Δm^2_{32}, two solutions are possible. One solution is called normal mass hierarchy with $m_3 > m_2$ and the other one is called inverted mass hierarchy with $m_2 > m_3$.
Because of the huge difference between Δm^2_{21} and Δm^2_{32}, the following simplification can be made:

$$\Delta m^2_{\mathrm{atm}} = \Delta m^2_{32} \approx \Delta m^2_{31} \tag{1.17}$$

This squared mass difference causes oscillations on the scale of $10^3\,\mathrm{m/MeV}$. For

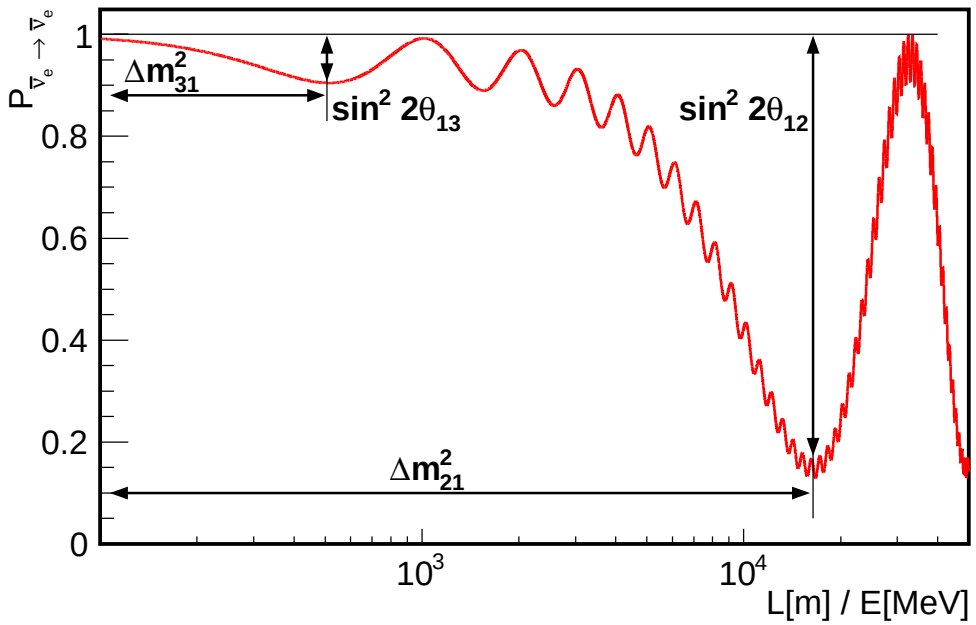

Figure 1.2: Survival probability of electron antineutrinos $P_{\bar{\nu}_e \to \bar{\nu}_e}$ (see equation 1.15) with parameters from table 1.2. Δm^2_{21} is causing the oscillation with a maximum at $1.6 \cdot 10^4$ m/MeV. The smaller oscillation caused by Δm^2_{31} is modulated onto the bigger one. The oscillation amplitudes are proportional to $\sin^2(2\theta_{12})$ and $\sin^2(2\theta_{13})$.

the first time it was measured in experiments detecting atmospheric neutrinos (like Super-Kamiokande [Tos01]), therefore it is also called "atmospheric squared mass difference" Δm^2_{atm}.
The other squared mass difference Δm^2_{21} is responsible for oscillations on the scale of 10^5 m/MeV and is called the "solar squared mass difference" $\Delta m^2_{\odot}$ because of the first determination in experiments with solar neutrinos (like radiochemical experiments [Dav68], [Alt05], [Sno02]).

$$\Delta m^2_{\odot} = \Delta m^2_{21} \tag{1.18}$$

With the example of the survival probability of electron antineutrinos $P_{\bar{\nu}_e \to \bar{\nu}_e}$, calculated in equation 1.15, the effects of neutrino oscillations can be seen in figure 1.2: The smaller oscillation caused by Δm^2_{31} is modulated onto the bigger oscillation caused by Δm^2_{21}.

1.3 Reactor neutrino oscillations

During nuclear fission in nuclear power plants, a huge amount of reactor neutrinos is produced. After the fission of fuel, neutron rich fission products undergo β-decay. So, exclusively electron antineutrinos $\bar{\nu}_e$ with a maximal energy of several MeV are

produced [Oli14]. The reactor neutrino production, using the example of ^{235}U, is shown in detail in figure 1.3. Besides neutrino production one can also see the chain reaction and the enrichment of uranium to plutonium.

In the case of the Double Chooz experiment, the electron antineutrino source consists of two nuclear power cores with a thermal power P_{th} of 4 250 MW each. In average, every nuclear fission process produces an energy of $E_{\text{fis}} = 210\,\text{MeV}$ and $\langle N \rangle = 6$ electron antineutrinos [Ams07]. The neutrino production rate $\dot{N}_\nu$ can be estimated with the nuclear fission rate $\dot{N}_{\text{fis}}$:

$$\dot{N}_\nu = \dot{N}_{\text{fis}} \cdot \langle N \rangle = \frac{P_{\text{th}}}{E_{\text{fis}}} \cdot \langle N \rangle = 2 \cdot 10^{21}\,\text{s}^{-1} \tag{1.19}$$

Because of the short baseline between source and detector ($\sim 1\,\text{km}$) in common reactor neutrino experiments, L/E is of the order of $10^3\,\text{m/MeV}$. With this ratio, one can see in figure 1.2 that only the smaller oscillation length from Δm^2_{13} and the amplitude from θ_{13} is important in this case. Therefore, the neutrino mixing for short baselines can be described as a two flavor system which leads to the following survival probability:

$$P_{\bar{\nu}_e \to \bar{\nu}_e} = 1 - \sin^2(2\theta_{13}) \sin^2\left(\frac{\Delta m^2_{31} L}{4E}\right) \tag{1.20}$$

It is important to remember that the expression is valid for using natural units. To express the length in units of meters instead of eV^{-1}, one has to deal with the constants which were set to one. The final expression for the survival probability of reactor neutrinos reads as follows:

$$P_{\bar{\nu}_e \to \bar{\nu}_e} = 1 - \sin^2(2\theta_{13}) \sin^2\left(1.27 \frac{\Delta m^2_{13}[\text{eV}^2] \cdot L[\text{m}]}{E[\text{MeV}]}\right) \tag{1.21}$$

1.4 Neutrino experiments with accelerators

Another possibility to study the physics of neutrino oscillations are experiments with particle accelerators. An intense beam of (anti)neutrinos can be produced with accelerators. For example, electron antineutrinos $\bar{\nu}_e$ can be produced out of a β-beam. Or accelerated pions can be produced which are decaying mainly into muon neutrinos ν_μ. Typically neutrino energies up to the GeV range can be reached with accelerators [Oli14].

The probability to detect a muon neutrino ν_μ as an electron neutrino ν_e in a detector at a distance L is

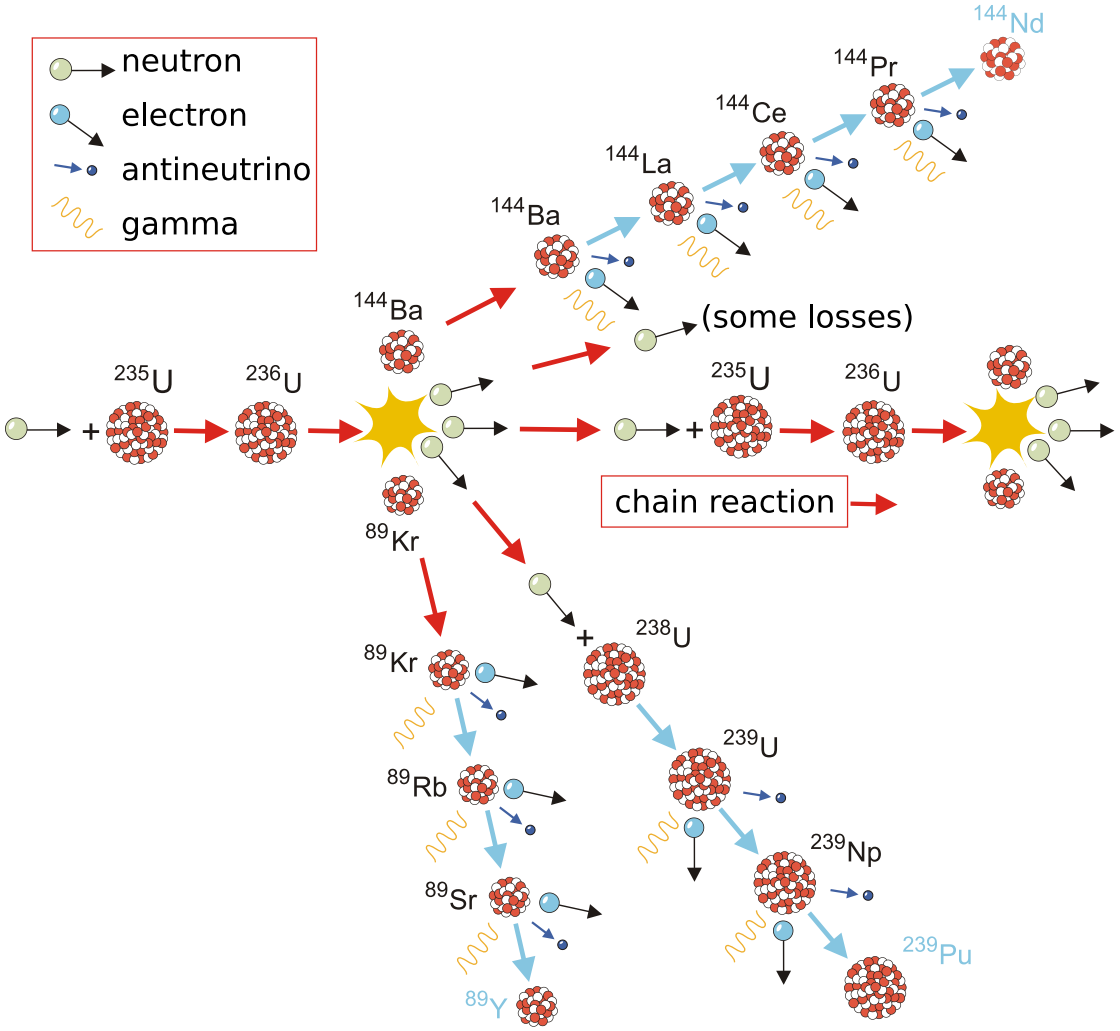

Figure 1.3: Reactor neutrino production during nuclear fission using the example of the fission of ^{235}U to ^{89}Kr and ^{144}Ba (other producing elements are ^{239}Po, ^{238}U, ^{241}Po, ordered by the fraction of produced reactor power; other fission products are also possible): The nuclear fission is induced by a neutron. The fission products are neutron rich and prefer to emit these neutrons. Furthermore the fission products undergo several β^--decays, each converting a neutron into a proton, an electron and an electron antineutrino. In average, six electron antineutrinos are produced in every nuclear fission process [Ams07].

$$
\begin{aligned}
P_{\nu_\mu \to \nu_e} \simeq & \sin^2(2\theta_{13}) \sin^2\theta_{23} \sin^2\left(\frac{\Delta m^2_{31} L}{4E}\right) \\
& \pm \alpha \sin(2\theta_{13}) \sin\delta_{\mathrm{CP}} \cos\theta_{13} \sin(2\theta_{12}) \sin(2\theta_{23}) \sin^3\left(\frac{\Delta m^2_{31} L}{4E}\right) \\
& - \alpha \sin(2\theta_{13}) \cos\delta_{\mathrm{CP}} \cos\theta_{13} \sin(2\theta_{12}) \sin(2\theta_{23}) \cos\left(\frac{\Delta m^2_{31} L}{4E}\right) \sin^2\left(\frac{\Delta m^2_{31} L}{4E}\right) \\
& + \alpha^2 \cos^2\theta_{23} \sin^2(2\theta_{12}) \sin^2\left(\frac{\Delta m^2_{31} L}{4E}\right)
\end{aligned}
\tag{1.22}
$$

with $\alpha = \frac{\Delta m^2_{21}}{\Delta m^2_{31}}$ [Hub03]. Accelerator experiments offer the possibility to study the CP-violating phase and to fix the mass hierarchy, i.e. determine the sign of Δm^2_{31}. But, the measurement depends on many parameters which are strongly correlated. Equation 1.22 shows the complex relations. A determination of the CP-violating phase δ is only possible if all other parameters are well known. Also it is important to note that a neutrino beam usually travels through earth for distances up to several 100 km until reaching the detector. Hence, effects due to oscillation in matter can't be neglected anymore.

Chapter 2
The Double Chooz experiment

The reactor neutrino experiment Chooz [Apo03] [Apo99] with only one detector is the predecessor of Double Chooz. The Chooz experiment provided with $\sin^2(2\theta_{13}) < 0.19$ at 90 % C.L. (for $|\Delta m^2_{\text{atm}}| = 2.0 \cdot 10^{-3}\,\text{eV}^2$) the most accurate upper limit on the mixing angle θ_{13} for a long period of time [Nak11]. With Double Chooz [Ard04] [Ard06] as succeeding experiment, θ_{13} was measured for the first time by a reactor neutrino experiment. Two identical detectors are located approximately 400 and 1 050 meters away from two nuclear power reactors at the Chooz power plant in France (see figure 2.1). The two 4.25 GW thermal power pressurized water reactors are operated by EDF (Électricité de France).
At the position of the near detector, oscillations coming from Δm^2_{31} can be neglected (see figure 2.2). Therefore, it is possible to measure the original reactor energy spectrum and flux of reactor neutrinos. At the location of the far detector, oscillation effects are already present. With the spectral deformation of the energy spectrum measured here, the oscillation amplitude and as a result the mixing angle θ_{13} can be determined. With data from both detectors it is possible to actually measure the produced reactor neutrino flux including its energy spectrum, instead of simulating it. The biggest contribution to the systematic uncertainty is therefore canceled and allows an improvement of the sensitivity on $\sin^2(2\theta_{13})$ in the order of one magnitude compared to the Chooz Experiment [Ard06].

2.1 Double Chooz detector design

Figure 2.3 shows the design of the Double Chooz far detector as 3D model. The Double Chooz near detector is constructed in an identical way to suppress systematic uncertainties due to differences between near and far detector. One major difference between both detectors is the rock overburden: While the far detector has a shielding

Figure 2.1: The Double Chooz experiment is located at the nuclear power plant in Chooz, a french village in the Ardennes. Each of the two reactors Chooz A and Chooz B has a thermal power of 4 250 MW. The average distance between the reactors and the neutrino detectors is approximately 400 and 1 050 meters respectively. The far detector is located in the same laboratory as the detector used in the Chooz experiment. Figure taken from [Cea10].

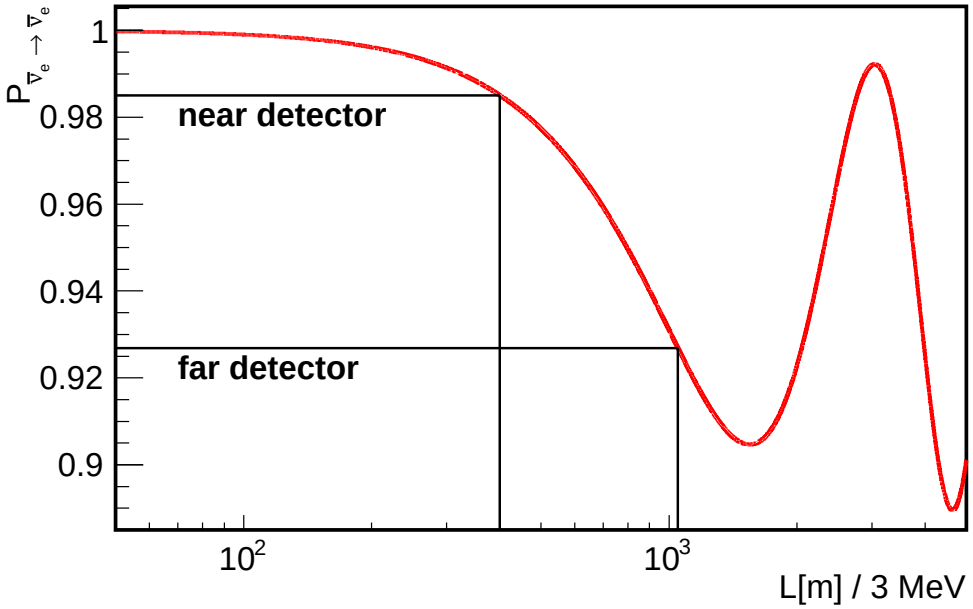

Figure 2.2: Survival probability for electron antineutrinos with an energy of 3 MeV (see equation 1.15) with parameters from table 1.2. At the location of the near detector almost no oscillation because of Δm^2_{31} occur. At the location of the far detector oscillation effects are clearly present.

of 300 m.w.e[1], the near detector has a shielding of only 120 m.w.e [Ard06].
The different volumes of the calorimetric liquid scintillator detector will be discussed in the following. From inside to outside the volumes are: Neutrino target (NT), gamma catcher (GC), buffer (BF) and muon veto (MV). The three innermost volumes are together also called inner detector (ID). The MV is also called inner veto (IV) to distinguish between this veto included in the detector and the outer veto (OV) which is mounted on top of the detector.

Neutrino target (NT)

The NT is the innermost part of the detector and consists of 10.3 m^3 of Gd-loaded liquid scintillator. It is contained in an acrylic vessel with a diameter of 2.3 m and a heigth of 2.5 m. The vessel is built out of 8 mm thick acrylics and is transparent for photons above 400 nm. The NT scintillator is a mixture of PXE (phenyl xylyl ethane, $C_{16}H_{18}$) and dodecane ($C_{12}H_{26}$). For an efficient detection of electron antineutrinos in the liquid scintillator by the inverse beta decay as described in section 2.2, a high number of protons in the target region is required. Furthermore, the NT scintillator is doped with gadolinium (about 1 g/l) to separate the neutron capture with a total energy of 8 MeV from other signals (see section 2.2).

[1] meter water equivalent, 1 m.w.e. = 100 g cm^{-2}

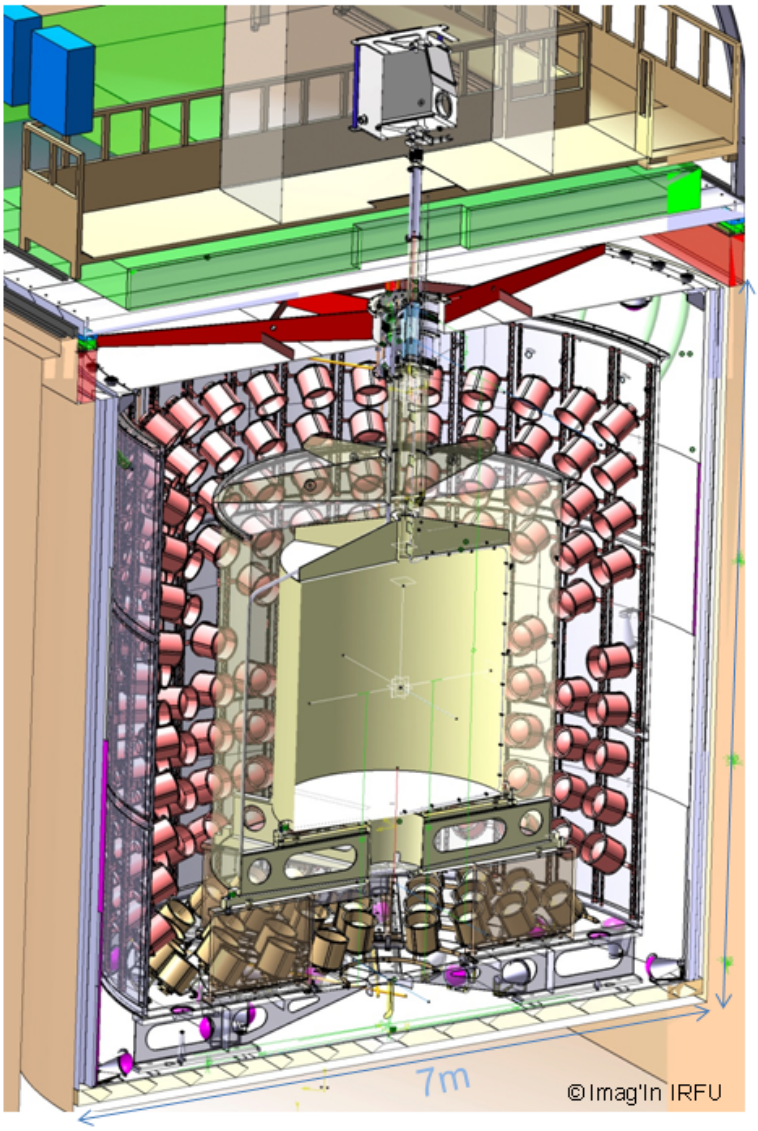

Figure 2.3: 3D Model of the Double Chooz far detector. The different volumes from inside to outside are: Neutrino target (NT), gamma catcher (GC), buffer (BF) and muon veto (MV). The three innermost volumes are together also called inner detector (ID). The MV is also called inner veto (IV) to distinguish between this veto included in the detecter and the outer veto (OV), which is mounted on top of the detector (painted in green). A more detailed description of the volumes can be found in the text. Picture taken from [Cea11].

Gamma catcher (GC)

22.5 m^3 of Gd-free liquid scintillator with a thickness of 55 cm surround the NT. The vessel containing this volume called GC has a diameter of 3.4 m and a height of 3.6 m. For the analysis with neutron captures on Gd, the NT is the fiducial volume. γ-rays of the detection reaction in the NT are detected in both NT and GC. This allows an efficient detection of the produced gammas, even for events which occur at the edges of the NT. For an analysis with neutron captures on hydrogen, the combination of NT and GC with a total volume of $\sim 33\,m^3$ is used as fiducial volume. This decreases the detection efficiency a bit, but increases the target volume by a factor of 3.

Buffer (BF)

To shield the inner part of the detector against natural radioactivity coming from the surroundings (e.g. the photomultipliers) the BF was installed. It forms a 105 cm thick layer of non-scintillating mineral oil with a total volume of 100 m^3. The liquids are contained in a stainless steel vessel with a diameter of 5.5 m and a height of 5.8 m. It also supports 390 low background 10-inch photomultiplier tubes (PMTs) [Mat11, Bau11]. With this set of PMTs the scintillation light produced in the inner part of the detector is measured.

Muon veto (MV), also inner veto (IV)

Although the detector is located in an underground laboratory, cosmic muons can enter or pass the detector and create background events. To detect muons passing the detector or muons which are stopped inside, a stainless steel vessel with a diameter of 6.5 m and a height of 6.7 m is installed. It is filled with 90 m^3 of scintillating organic liquid and is equipped with 78 PMTs to detect the produced light. They are only sensitive to light produced in the MV since it is optically separated from the ID. Thus, muon events can be removed from the data set while searching for neutrinos or can be used for other studies.

Shielding

For the far detector, a layer of demagnetized steel plates with a thickness of 15 cm is installed around and on top of the detector. It has a total weight of 300 t and suppresses radioactivity from the rock around the detector. At the near detector, the steel shielding around the detector is replaced by a water shielding with a thickness of about 90 cm. Again, it is combined with steel plates on top of the detector.

Outer veto (OV)

To cover the chimney, a feedtrough which crosses all detector volumes, another active veto was installed. Plastic scintillator plates on top of the detecter and under the ceiling of the laboratory form the OV.

2.2 Detection of reactor neutrinos

To detect the electron antineutrinos $\bar{\nu}_e$ coming from the reactor, a reaction called inverse beta decay (IBD) is used. The electron antineutrinos are captured on protons and a positron and a neutron are produced in every reaction:

$$\bar{\nu}_e + \mathrm{p} \longrightarrow \mathrm{e}^+ + \mathrm{n}$$

This reaction has a relatively high cross section of $10^{-43}\,\mathrm{cm}^2$. For the calculation of the mass difference in this reaction, the neutrino mass can be neglected:

$$(m_e + m_n) - m_p = 0.51\,\mathrm{MeV} + 939.6\,\mathrm{MeV} - 938.3\,\mathrm{MeV} = 1.8\,\mathrm{MeV} \tag{2.1}$$

The energy threshold for the reaction is therefore 1.8 MeV. In Double Chooz, both the positron and the neutron are detected to identify IBD events. To increase the reaction rate, the Double Chooz target scintillator is rich of protons to increase the number of reaction targets. Furthermore, the scintillator is doped with gadolinium to distinguish the neutron signal from the positron signal. After neutron capture on gadolinium, 3-4 gammas with a total energy of 8 MeV are emitted:

$$\mathrm{Gd} + \mathrm{n} \longrightarrow \mathrm{Gd}^* \longrightarrow \mathrm{Gd} + \sum_{\gamma}$$

The total gamma energy is well above the positron signal or low energy background events[Ard06]. Another benefit from the doping with gadolinium is an increased cross section for neutron capture compared to hydrogen and carbon in the liquid scintillator [Vog99].

Signature of the positron signal

- e^+ will deposit its energy through ionization
- e^+ will annihilate with e^- and will produce two gammas with an energy of 511 keV each

→ prompt signal with a minimal energy of 1.022 MeV

Signature of the neutron signal

- neutron will thermalize through collisions (life time $\tau \approx 30\,\mu\mathrm{s}$)
- production of 3-4 gammas due to neutron capture on gadolinium

→ delayed signal with an energy of about 8 MeV

The expected IBD signal can be seen in a schematic view in figure 2.4. To calculate the neutrino energy $E_{\bar{\nu}_e}$, the visible energy E_{vis} due to radiation from positron

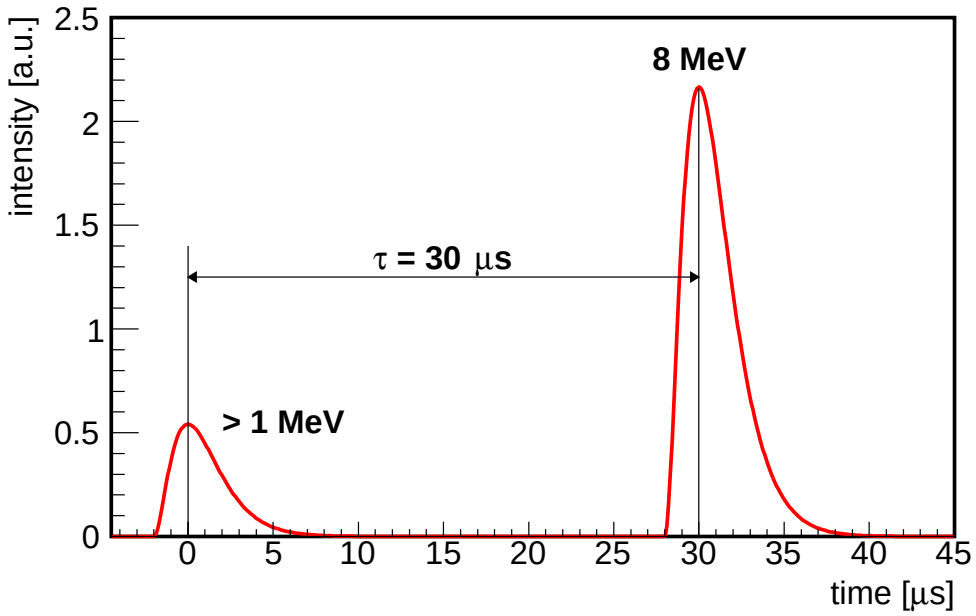

Figure 2.4: Schematic view of the coincidence signal of the detection reaction. First, the prompt signal comes from the positron and has at least an energy of 1 MeV. In average 30 μs later, neutron capture on gadolinium produces a second delayed signal with an energy of 8 MeV. This coincidence signal allows a significant reduction of background.

annihilation has to be taken into account. First, the energy balance of the IBD for a neutrino with kinetic energy $E_{\bar{\nu}_e}$ and a proton at rest is calculated:

$$E_{\bar{\nu}_e} + m_{\bar{\nu}_e} + m_p = E_{e^+} + m_{e^+} + E_n + m_n \tag{2.2}$$

The produced positron with energy E_{e^+} will annihilate with an electron and will create two gammas with a total visible energy E_{vis}:

$$E_{e^+} + m_{e^+} + m_{e^-} = E_{\text{vis}} \tag{2.3}$$

If one neglects the neutron recoil and the neutrino mass, which is very small compared to the other masses, the last two equations can be combined into the following energy balance equation:

$$E_{\bar{\nu}_e} \simeq E_{\text{vis}} - m_{e^-} + (m_n - m_p) = E_{\text{vis}} + 0.8\,\text{MeV} \tag{2.4}$$

Thus the energy of the initial electron antineutrino $\bar{\nu}_e$ can be reconstructed from the visible energy measured for the respective prompt positron signal.

2.3 Status of the experiment

The data taking with the Double Chooz far detector started in 2011. Since then, the Double Chooz experiment was able to release several publications. With every publication, a better understanding of the background contributions and new analysis methods could be presented. The live time and the number of IBD coincidences for the different publications are summarized in table 2.1. A summary of measured values for the mixing angle θ_{13} from the publications can be found in table 2.2.
Double Chooz published the first measurement of a nonzero value for θ_{13} in 2012 [Abe12a]. The presented analysis uses neutron capture on gadolinium and is therefore referred to as Gd-I analysis. A total live time of 96.8 days was used for this first analysis. Within the same year an updated analysis, referred to as Gd-II, was published [Abe12b]. At total live time of 228 days provided a significant reduction of the statistical uncertainty of the measurement. Instead of using neutron capture on gadolinium in the NT, the neutron capture on hydrogen in both NT and GC can be used for an analysis. This will increase the fiducial volume by a factor of 3, but on the other hand, it increases the accidental background contribution. Anyways this provides a different approach for the θ_{13} measurement. A publication with this method using the same dataset as for Gd-II was released in 2013 [Abe13a]. Because of changes in the applied selection cuts, the live time was slightly increased to 240 days.
The Double Chooz experiment was able to measure 7.53 days with both reactors off. This is an unique feature among all reactor neutrino experiments. Data from this reactor off-off period allows to put a constraint on the total background rate and provides a test for the background model [Abe13b]. This data was also important for a dedicated analysis published in 2013. The advantage of variations in the thermal power of both reactors was used to perform the so called reactor rate modulation (RRM) analysis [Abe14b]. There is a linear correlation between observed and expected neutrino candidate rate at different reactor power levels, which can be used for a background independent determination of θ_{13}. This approach is different to all previous analysis methods, but it showed good agreement with the values from other Double Chooz publications.
In 2014 an improved analysis with neutron capture on gadolinium and 468 days of live time was published [Abe14c]. This analysis is referred to as Gd-III and includes several improvements. For example, the reactor off-off data and a measured spectrum of ^{238}U was included in the analysis. Together with new analysis methods, the signal to noise ratio was improved from 15.6 to 22 compared to the Gd-II analysis. Some further results of this analysis will be shown in section 2.4.
Data taking with the Double Chooz near detector started at the beginning of 2015 and first data is available for analysis. A study addressing the radiopurity of the near detector using this data will be presented in section 5.1. Data from both Double Chooz detectors will enable a significant reduction of both reactor and detector related systematic uncertainties. The projected sensitivity for Double Chooz in the case of $\sin^2 2\theta_{13} = 0.1$ is shown in figure 2.5. A precision of 0.015 on the measurement

	live time	IBD coincidences	prediction
Gd-I [Abe12a]	96.8 d	4 121	$4\,344 \pm 165$
Gd-II [Abe12b]	227.9 d	8 249	$8\,937 \pm 161$
Gd-III [Abe14c]	467.9 d	17 351	$18\,290^{+370}_{-330}$
H-II [Abe13a]	240.1 d	36 284	$36\,680 \pm 520$

Table 2.1: Live time, number of found IBD coincidences and prediction for the number of events in case of the no oscillation hypothesis for different Double Chooz publications. Gd-I, Gd-II and Gd-III are analyses using neutron capture on gadolinium, H-II is an analysis using neutron capture on hydrogen.

	result on $\sin^2 2\theta_{13}$	background rate
Gd-I [Abe12a]	$0.086 \pm 0.041(\text{stat}) \pm 0.030(\text{syst})$	3.46 ± 1.26
Gd-II [Abe12b]	$0.109 \pm 0.030(\text{stat}) \pm 0.025(\text{syst})$	2.18 ± 0.58
Gd-III [Abe14c]	$0.090^{+0.032}_{-0.029}$	$1.68^{+0.41}_{-0.17}$
H-II [Abe13a]	$0.097 \pm 0.034(\text{stat}) \pm 0.034(\text{syst})$	79.1 ± 1.3
RRM [Abe14b]	$0.102 \pm 0.028(\text{stat}) \pm 0.033(\text{syst})$ (Gd+H combined)	0.9 ± 0.4 (Gd) 9.0 ± 1.5 (H)

Table 2.2: Measured value for $\sin^2 2\theta_{13}$ and total background rate for different Double Chooz publications. Gd-I, Gd-II and Gd-III are analyses using neutron capture on gadolinium, H-II is an analysis using neutron capture on hydrogen and RRM is the so called reactor rate modulation analysis.

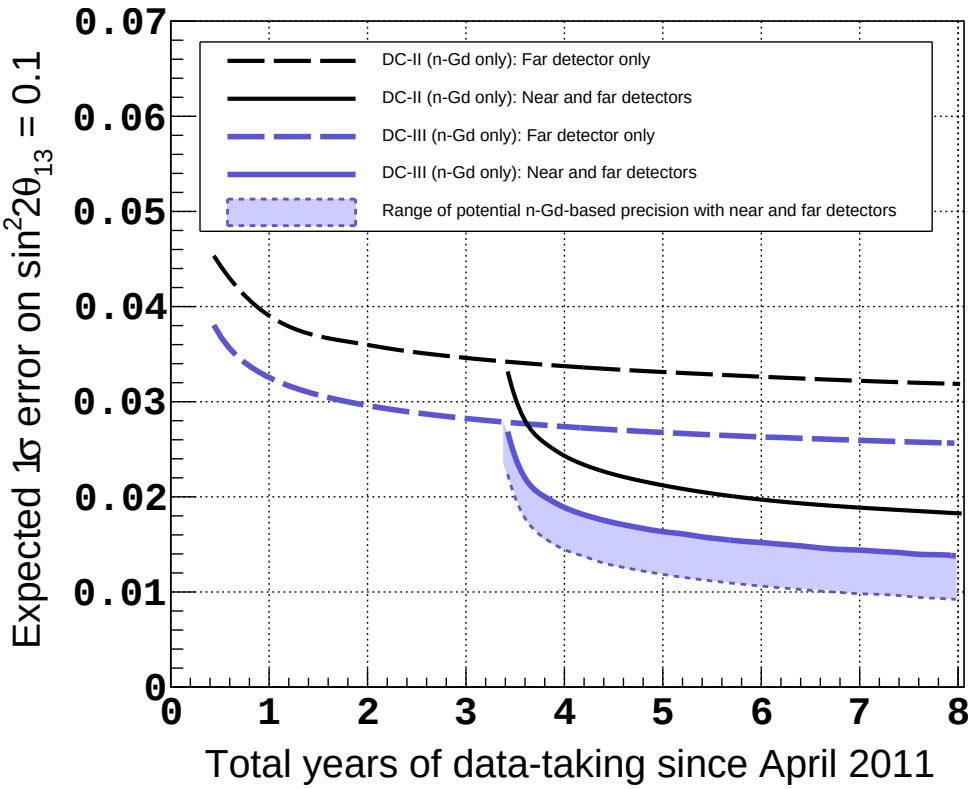

Figure 2.5: Projected sensitivity for the Double Chooz experiment in the case of $\sin^2 2\theta_{13} = 0.1$. With only the far detector (dashed lines), the precision of the θ_{13} measurement is limited by the systematic uncertainty of the flux prediction. With using both near and far detector (solid lines), uncertainties on the background should be dominant. The plot also shows the improvements due to new analysis methods introduced with the Gd-III analysis. The improved sensitivity between the black and blue curves depicts this achievement. Figure taken from [Abe14c].

of $\sin^2 2\theta_{13}$ can be reached after three years of data taking with both detectors. Improvements in the analysis techniques could presumably lower the precision of the Double Chooz experiment to 0.01 in further studies.

2.4 Latest results from Double Chooz

The latest publication of the Double Chooz experiment presents independent analysis methods to improve the measurement of θ_{13} [Abe14c]: A combined rate and spectral shape analysis as well as a background-model-independent analysis based on reactor power variations. An unique feature of the Double Chooz experiment is that it was able to take data during a time period with both reactors off. This provides access to the background only measurement, allowing to cross check the

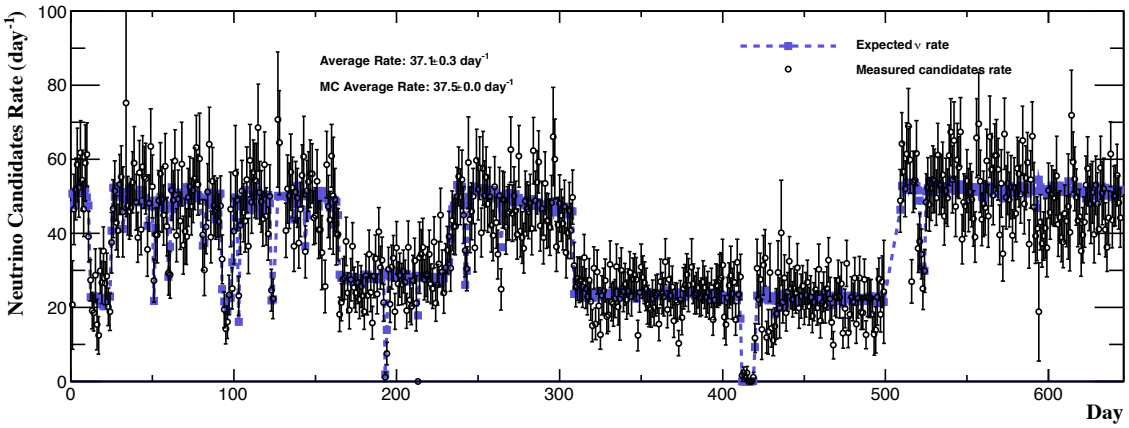

Figure 2.6: Measured and expected neutrino rate for the data taking period from April 2011 to January 2013 with the far detector. In total this corresponds to 66.5 GW-tons of exposure and 17 351 IBD candidates. Unique among all reactor neutrino experiments are 7.24 days with both reactors off. Plot taken from [Nov15a].

background models used in the oscillation analysis. The new analysis based on 467.90 live days with 66.5 GW-ton-years of exposure with far detector only, leads to a value of $\sin^2 2\theta_{13} = 0.090^{+0.032}_{-0.029}$. A short overview over some results will be shown in this section.

In the latest publication only data of the Double Chooz far detector is used. Hence, an accurate reactor flux simulation was needed to obtain a $\bar{\nu}_e$ prediction. The location and composition of reactor fuel as well as the instantaneous thermal power for each reactor is provided by EDF, the operator of the Chooz nuclear power plant. The evolution of both fission rates and fuel composition, including their uncertainties, is done with MURE [Mep05, Nea09] code. The reference electron antineutrino spectra for ^{235}U, ^{239}Pu and ^{241}Pu are computed from their β-spectrum [Sch85, Fei82, Hah89], while the ^{238}U spectrum [Haa14] is used for the first time. To improve the suppression of normalization uncertainties in the $\bar{\nu}_e$ prediction, Double Chooz uses the $\bar{\nu}_e$ rate measurement from Bugey4 [Dec94]. The systematic uncertainty on the IBD signal rate associated with the flux prediction is evaluated to be 1.7 % of which the dominant component is an uncertainty of 1.4 % in the Bugey4 measurement. Figure 2.6 shows expected ν rate and measured IBD candidate rate for the whole data taking period from April 2011 to January 2013.

During the data taking period, Double Chooz was able to collect 460.67 days of live time, with at least one reactor on. In this time 17 351 IBD candidates were observed, compared to the prediction without oscillation of $18\,290^{+370}_{-330}$ events. This deficit is due to the non-vanishing value of θ_{13} and the presence of neutrino oscillations. In addition, 7.24 days with both reactors off were collected, which is unique amongst all reactor neutrino experiments. 7 ± 2.6 (stat.) IBD candidates were found during the

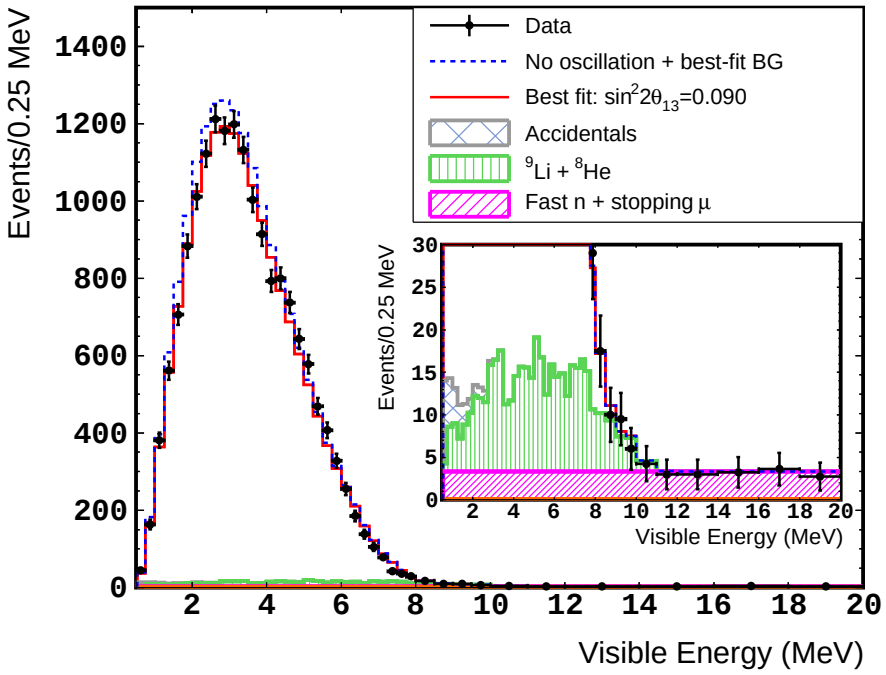

Figure 2.7: The measured energy spectrum of the prompt signal (black points) superimposed on the prediction without neutrino oscillation (blue dashed line) and the best-fit with $\sin^2 2\theta_{13} = 0.090$ (red line). Background components after the fit are also shown with different colors: accidental (grey, cross-hatched); ^{9}Li + ^{8}He (green, vertical-hatched); and fast neutron + stopping muons (magenta, slant-hatched). Figure taken from [Abe14c].

off-off period, whereas the prediction was $12.9^{+3.1}_{-1.4}$. This allows to put a constraint on the total background rate and provides a test for the background model.
In the Rate+Shape analysis the measured energy spectrum of the IBD candidates is compared to the prediction coming from the Monte Carlo simulation (see figure 2.7). A scan of χ^2 is carried out over a wide range of $\sin^2 2\theta_{13}$, minimizing it with respect to eight fit parameters for each value of $\sin^2 2\theta_{13}$. The minimum χ^2 value, χ^2_{min}/d.o.f. $= 52.2/40$, is found at $\sin^2 2\theta_{13} = 0.090^{+0.032}_{-0.029}$, where the error is given as the range which gives $\chi^2 < \chi^2_{\text{min}} + 1.0$. Figure 2.7 shows the energy spectrum of the prompt signal superimposed on the best-fit prediction and the background components. Assuming the inverted hierarchy with $|\Delta m^2_{31}| = 2.38^{+0.09}_{-0.10} \times 10^{-3}\,\text{eV}^2$ [Ada14], the best-fit is found at $\sin^2 2\theta_{13} = 0.092^{+0.033}_{-0.029}$ with χ^2_{min}/d.o.f. $= 52.2/40$.
A new precise measurement of θ_{13}, based on several independent analysis methods, was presented in the last Double Chooz publication. Consistent values for $\sin^2 2\theta_{13}$ are found for all presented methods. For a complete discussion, please refer to the latest Double Chooz publication [Abe14c].

Chapter 3
3 Near detector integration

For the Double Chooz near detector integration several tasks had to be performed. Besides the installation of several systems, the liquids for MV and BF were prepared on-site. The liquids were mixed and stored in the liquid storage area (LSA) facility, which was already used for the far detector. For the far detector integration there was a connection between LSA and detector through the tunnel to the laboratory. This time, the liquids had to be transported to an unloading area close to the near detector laboratory tunnel entrance. The transport was done using two trailers with a nominal carrying capacity of 35 m^3 each. From the unloading area, a connection to the near detector laboratory, called trunk line, with a total length of 200 m was installed. In the laboratory, the near detector filling and operating system (DFOS) was used to fill the detector in a safe way with the liquids and nitrogen coming through the trunk line. Because of the experience from the filling process of the far detector and due to improvements in the filling procedure, the near detector filling was very efficient. Although the filling process had to be interrupted for refilling the trailers, the whole procedure was completed in less than 4 weeks.

3.1 Preparation of MV and BF liquids

Six storage tanks are available in the LSA for the liquid preparation. Three tanks with a volume of 33 m^3 each are installed for MV liquids, and three tanks with a volume of 40 m^3 each are installed for BF liquids. The liquids and the tanks are strictly separated, for each group there is a particular liquid handling station. Every station contains a pump, a liquid filter and nitrogen supply for the tanks. Details on the LSA and the pumping station can be found in [Pfa12].
Seven trucks delivered the main components for the MV and BF liquids with a total volume of 175 m^3 with trailers. The two main components of the MV liquid scintillator are n-paraffine and LAB (linear alkylbenzene). For the BF liquid the two main components are n-paraffine and Dinol, a mineral oil. Each trailer was

connected to the dedicated pumping station of the MV or BF system. The liquids were evenly distributed among the corresponding tanks and were filtered during unloading. Depending on the liquid temperature and type, a rather low unloading rate between 1 and 2 m^3/h was possible. To support the unloading, the trailers were pressurized with nitrogen. The remaining components of MV and BF liquids were delivered in several intermediate bulk containers (IBCs). Besides the delivered liquids, some left leftovers from the far detector filling could be reused.
After the delivery, the liquids were circulated through the system to get a blending between the three tanks of a group. In parallel the tanks were bubbled with nitrogen to mix the liquids inside the tanks. After this procedure, the density of the liquids was measured and readjusted to match exactly the target density of 0.804 g/cm^3 for all liquids. It took one week of circulation before the liquids formed a homogeneous mixture and the final density test could be performed. In total 90 m^3 of MV liquid scintillator and 100 m^3 of BF liquid have been prepared.

3.2 Infrastructure at near detector site

At the entrance to the near laboratory tunnel, a large area for the handling of the detector supplies is available. In this area called unloading area, three huge retention pits were arranged. The big size of the pits allowed a truck to place a whole container with a holding capacity of 35 m^3 on a trailer inside the retention pits. A container with 25 m^3 of GC liquid scintillator was placed permanently inside one of the retention pits. The NT liquid scintillator was stored directly inside the near detector laboratory. Furthermore a liquid nitrogen plant has been installed next to the unloading area. The nitrogen supply was needed for liquid handling in the unloading area as well as for the near detector.
To transfer the liquids and the nitrogen from the unloading area to the near detector laboratory, a supply connection called trunk line was installed. For each of the four detector volumes[1] a ¾" pipe and for the nitrogen supply a ½" pipe were needed. A metallic channel with a cross section of 30 cm × 30 cm was installed during the construction of the laboratory, so only a fixation for the pipes was needed (see figure 3.1, left). 75 holders made out of aluminium were produced by the workshop at TUM. Each holder has a pipe clamp for the nitrogen supply and four pre-assembled cable ties for the liquid pipes. The inner dimension of the metallic channel showed big variations, therefore the holder has a length of only 28 cm and can be adjusted to the inner dimension of the channel by simply bending the brackets on the outside. Figure 3.1, right shows a holder after it was fixed with rivets inside the trunk line channel and with the first two supply pipes mounted.
For the handling of the liquids in the near laboratory a DFOS module for each detector volume was used. The modules for MV, BF and GC liquids are equipped with stainless steel components whereas the module for the NT liquid scintillator only

[1] The NT liquid scintillator was stored in the laboratory inside a weighing tank during filling, the trunk line connection was used to transport the liquids into the laboratory beforehand.

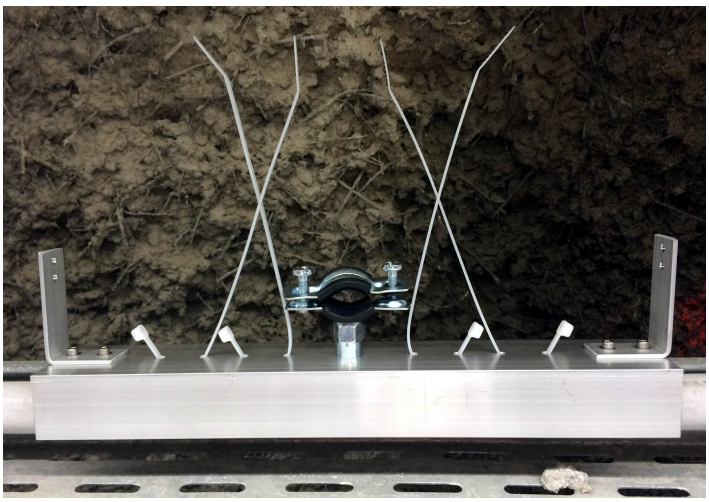


Figure 3.1: Pictures of a holder used for the fixation of the trunk line pipes (left). In the middle of the holder there is a pipe clamp for the $^1/_2$" nitrogen supply pipe. The four liquid pipes were fixated using cable ties. The brackets on the outside were used to adjust to the changing inner dimension of the trunk line channel. The holders were fixated at the channel walls using rivets (right).

contains Polytetrafluoroethylene (PTFE) components due to material compatibility (see figure 3.2). During the filling process, the liquids were filtered again before entering the detector and a mass flow meter enabled the precise determination of the amount of filled detector liquids. For the filling of the chimney, a fine filling system was included in the BF, GC and NT modules to release a predefined amount of liquid step-by-step into the corresponding detector volume. The design of the MV, BF and GC modules is a reduced version of the far detector design. Because of the experiences made during far detector filling, even this reduced design allowed a secure filling of the Double Chooz near detector. The NT module is the same as the one used for the far detector filling, it was moved to the near laboratory before the start of the filling process. Any details about the DFOS design can be found in [Pfa12].

3.3 Transport of liquid scintillator

As mentioned before, it was necessary to move the MV and BF detector liquids from the LSA to the unloading area at the near detector site. Two swap body tanks with a nominal holding capacity of 35 m^3 each were used for this purpose. They were mounted on a trailer and were moved by a rental truck (see figure 3.3).
The number of movements had to be minimized, because every time the swap body tanks had to be disconnected from the trunk line at the unloading area, moved

Figure 3.2: Picture of the near detector DFOS. The three modules on the left side with stainless steel components are for BF, GC and MV liquids respectively. The module on the right side with PTFE components is used for the NT liquid handling. Every module has a membrane pump, a liquid filter, intermediate tanks and a mass flow meter. The switchboard on the very left side is used to control selected valves and to start or stop the pumps included in every module. A leakage detection system will shut all valves and turn off the pumps if any liquid is detected in the white trays below each module.

Figure 3.3: Picture of a trailer with a swap body tank used for detector liquids transportation from the LSA to the unloading area. Two swap body tanks with a nominal holding capacity of 35 m^3 each were used for the transportation of the MV and BF liquids. The picture shows the placing of the container inside a retention pit on the unloading area.

one by one by a rental truck and connected to the pumping stations in the LSA and vice versa. This caused a delay of several hours for every movement because of the security restrictions inside the area of the nuclear power plant and due to the shift of equipment and shifters. Furthermore, the refilling process had to be optimized because the detector filling has to be interrupted during refilling the swap body tanks. The nitrogen supply at the LSA is not able to support both pumping stations at full output. But it possible to fill both swap body tanks in parallel with one pumping station at full output and the other one at 60-70 % of its maximum output. By preferring the swap body tank with the higher target liquid load and running its pumping station at maximum output the total loading time can be reduced.

3.4 Near detector filling process

Due to the restriction, that the filling process may not be interrupted during the filling of the NT volume and during filling in the chimney region, three filling steps with previous swap body tank filling were defined:

1. filling until the bottom of the NT vessel is reached
2. filling till the liquid level is 5 cm below the start of the NT vessel lid slope

3. filling until the expansion tank operating system (XTOS) is communicating with the detector

The amount of BF liquid needed for the second filling step exceed the loading capacity of a swap body tank. Therefore $2\,m^3$ of BF liquid were stored in IBCs in the unloading area after filling step 1. Another restriction was the access to the area of the nuclear power plant. The access to the LSA was only permitted from Monday to Friday. Hence, the refill process of the swap body tanks had to be fitted to this period. With starting the first swap body tank filling on Monday, this restriction was fulfilled for all further filling steps. An overview of the duty roster can be found in table 3.1.
During filling steps 1 and 2 and swap body tank filling, two shifts a day covered 15 hours of work per day. During filling with a liquid level inside one or more chimney regions it was not possible to interrupt the filling process to ensure the detector safety. Hence, during filling step 3, the whole day was divided into three shifts. The filling process was completed successfully on October 6th 2014 (day 22). Although the filling process was interrupted by the filling of the swap body tanks, it took less than four weeks to fill the Double Chooz near detector. Compared to the far detector filling time of 2 month, this is a great improvement.

day	weekday	liquid storage area (LSA)	detector / unloading area
1	Mon	swap body tank filling	
2	Tue	swap body tank filling	
3	Wed		purity test after rinsing
4	Thu		filling step 1
5	Fri		filling step 1
6	Sat		filling step 1
7	Sun		filling step 1
8	Mon		filling step 1
9	Tue		backup / free time
10	Wed	swap body tank filling	
11	Thu	swap body tank filling	
12	Fri		filling step 2
13	Sat		filling step 2
14	Sun		filling step 2
15	Mon		filling step 2
16	Tue		backup / free time
17	Wed	swap body tank filling	
18	Thu	swap body tank filling	
19	Fri		filling step 3
20	Sat		filling step 3
21	Sun		filling step 3
22	Mon		filling step 3
23	Tue		backup / free time

Table 3.1: Reduced duty roster for near detector filling. The filling of the swap body tanks was only permitted from Monday to Friday. Until day 18 two shifts a day were scheduled, three shifts covered 24 h per day during filling step 3. The filling process was completed successfully on day 22.

Chapter 4

4 Level measurement system

The level measurement (LM) system for the Double Chooz detectors is a crucial part for operating the detector filling systems and monitoring the detectors during the several years of their life time. Because of the rigid but fragile inner structure of a detector with its two acrylic vessels, both gas pressure and liquid level have to stay within strict margins. A tolerable amount of stress can be translated into 3 mbar differential gas pressure or 3 cm of difference in liquid levels. To ensure a secure filling of the detectors the allowed difference was set to 1 mbar differential gas pressure and 1 cm difference in liquid level.
To stay within these strict margins, a measurement system with high precision and accuracy was needed. Several measurement devices were put together into one system to fulfill the constraints and to provide redundancy. Measured values and the different measurement systems are summarized in table 4.1 and will be explained section 4.1.
For the far detector, the sensors were connected to a National Instruments computer and were monitored with a LabVIEW program. The parts and the computer from National Instruments are very expensive ($> 10\,000$ €) and the measurement devices need special software and drivers for the operating system (Windows XP). Therefore the measurement system is vulnerable to problems of the operating system and can be misused as work station computer. During several years of operating in the far laboratory, the measurement computer also suffered from several hardware issues and one breakdown, which required a complete replacement. All maintenance and repair operations require a huge effort to get to France and to access the computer. As part of this thesis, a completely new measurement system was designed and built for the Double Chooz near detector. All measurement electronics are specially designed for each purpose and custom-made. Because of the low costs, it was possible to have spare parts ready for repairs or even for a complete replacement of the far detector system. Due to the modular design of the whole system, each part can be changed even by a person unfamiliar with the measurement system. The different electronic modules will be explained in section 4.2.

measurement device	measured value	type	monitored volumes MV	BF	GC	NT
hydrostatic pressure sensor	liquid level	absolute	✓	✓	✓	
laser sensor	liquid level	absolute	✓	✓	✓	
cross reference system	liquid level	differential	✓	✓	✓	✓
critical point sensor	liquid level	point			✓	✓
Tamago	liquid level	absolute				✓
pressure sensor	gas pressure	absolute	✓	✓	✓	✓
pressure sensor	gas pressure	differential	✓	✓	✓	✓
XTOS weighing cell	liquid level	calculated	–	✓	✓	✓
XTOS pressure sensor	gas pressure	absolute	–	✓	✓	✓

Table 4.1: Measurement devices of the level measurement (LM) system. In the detector, liquid level is measured by four different systems: hydrostatic pressure sensors (HPSs), laser sensors, a cross reference system (XRS) and a so called Tamago. For critical liquid levels, e.g. bottle necks, critical point sensors (CPSs) are installed as well as sensors for absolute and differential gas pressure. In the expansion tank operating system (XTOS), weighing cells under the tanks and sensors for absolute gas pressure are installed.

In section 4.3 the software which was developed during this thesis will be explained. Besides the firmware needed for the microcontrollers and scripts running on the measurement computer, two software packages were developed. During the filling process, a program running on a desk computer connected to the measurement system, provided a fast rate of measurement data, plots and some basic tools for the shifter. After the filling, for the several years of detector operation, the desk computer was removed and the measurement data for monitoring the detector is provided through a web interface.
The measurement computer, a credit card sized computer called Raspberry Pi [Ras13] and which costs less than 50 $, will be addressed in section 4.4. It controls the electronic modules and provides access to the measurement data. The operating system (linux distribution with customized kernel) runs completely from a SD memory card. Downloading the recent linux distribution, recompiling the linux kernel, installing all measurement software from a software repository and configuring the measurement system can be achieved by running a single script on a host computer. Therefore the memory card with the operating system including the newest software can be built from scratch by anyone available in case of maintenance or repair of the system.
Additionally, a concept for a completely remote maintenance of the measurement system and regular data and system configuration backups was established. A functional description of the electronic modules will be provided in section 4.2, whereas a technical description can be found in appendix A.

4.1 Level measurement sensors

For controlling the filling process and monitoring the detector, several distinct sensors were used. The most relevant sensors for the detector and their positions are illustrated in figure 4.1. Besides the shown sensors, other sensors for the lab environment and XTOS are used. A complete list of monitored parameters is shown below:

- barometric pressure and temperature in the laboratory
- detector liquid levels and temperatures
- gas pressure in detector volumes
- liquid masses and gas pressure in the XTOS tanks
- supply voltage levels of all sensor modules

4.1.1 Hydrostatic pressure sensors (HPSs)

The HPS system measures liquid level and temperature for MV, BF and GC volumes. Figure 4.1 illustrates the positions of the sensors, for each volume the lowest

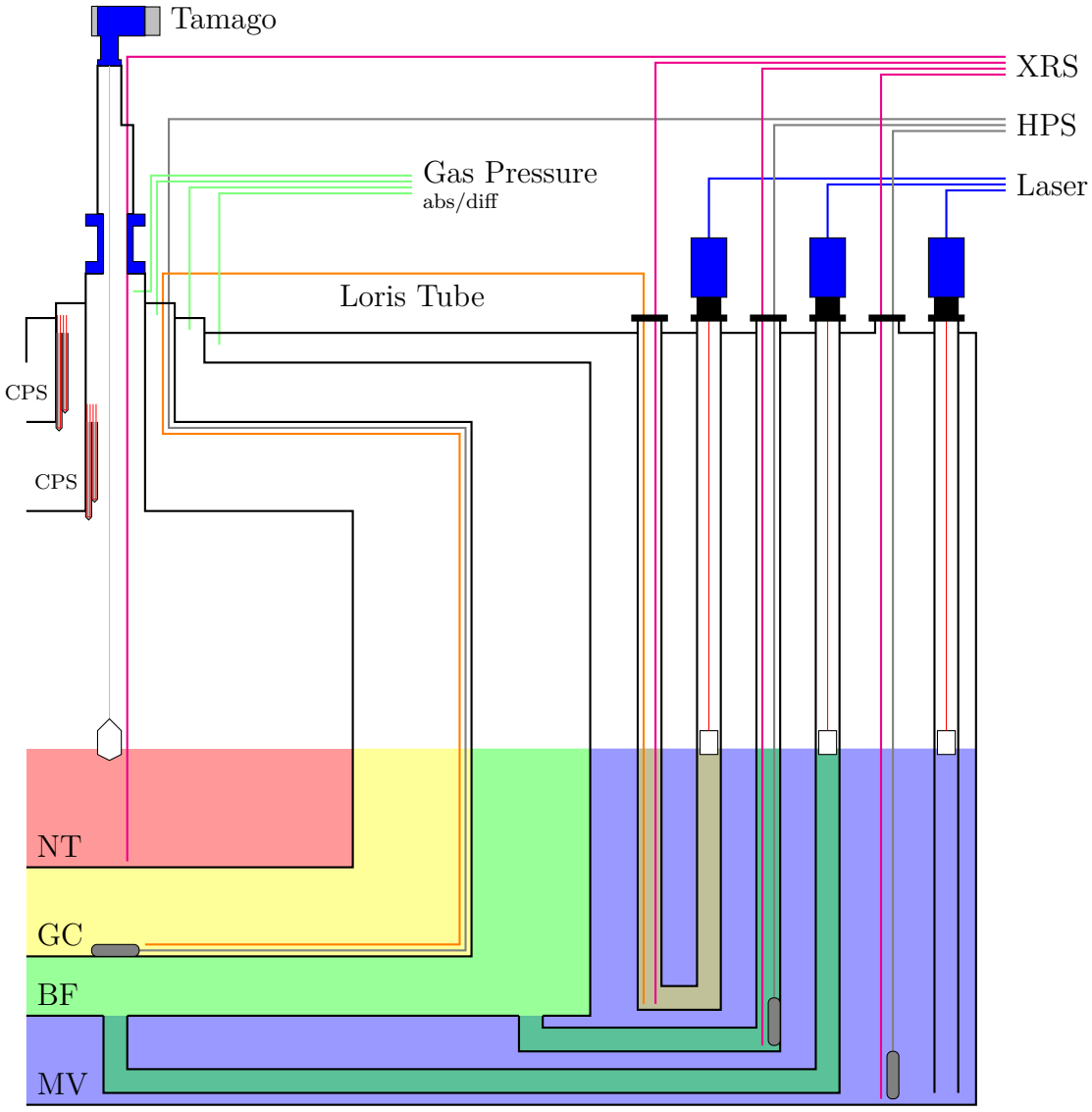

Figure 4.1: Schematic view of the LM system with the positions of the sensors. The NT is only accessible through a chimney and due to material compatibility the Tamago system replaced a hydrostatic pressure sensor (HPS). The GC hydrostatic pressure sensor (HPS) and a pipe connected to an inverted syphon (called Loris Tube) was installed during the detector construction. All further GC sensors are installed in a side tube also connected to the Loris Tube. The BF has two tubes connected to the middle and the edge of the volume, which contain all BF sensors. The MV volume is directly accessible through flanges at the detector top lid. Filling into the NT and the GC chimney is a delicate operation due to the reduced surface. So called critical point sensors (CPSs) have been installed to cross check the liquid level around the chimney edges.

Figure 4.2: Picture of a hydrostatic pressure sensor (HPS) (left). The housing is completely made of stainless steel and the supply cable is coated with PTFE to ensure material compatibility with the liquid scintillator. It has a reader for hydrostatic pressure and temperature measurement. The sensor is able to compensate changes in liquid temperature or gas pressure above the liquid. All three sensors (MV, BF and GC) were calibrated simultaneously using an acrylic tube with a pipe filled with water at several liquid levels to ensure a proper calibration before installation in the detector (right).

possible point was chosen for installation. The sensor is manufactured by STS Sensors [Sts15] and is completely made out of stainless steel and has a cable coated with PTFE for power supply and readout (see figure 4.2, left). At the bottom of the device, a sensor head with a stainless steel membrane is welded to the housing. Inside, a piezo crystal measures the pressure difference between the outside of the sensor and the pressure in a small capillary, which is hidden in the cable. Before the cable leaves the detector, the capillary was extracted from the cable and is exposed to the gas phase above the liquid. It is important to use the gas pressure in the detector and not the one in the laboratory. The detector has typically an overpressure of 1-2 mbar, which corresponds to a difference in the liquid level measurement of more than 1 cm compared to a measurement with the capillary at laboratory pressure.

Together with the sensor, the manufacturer sent a calibration protocol with only a few data points. To ensure a high accuracy, all sensors have been calibrated again with a custom setup at TUM (see figure 4.2, right). The sensors were placed in an acrylic tube with a long but much thinner tube connected. The calibration setup was installed in a stairwell to have at least 7 meters of height. Then, water was filled step by step into the tube and the analog-to-digital converter (ADC) value for each

sensor was recorded several times. The liquid level in each measurement was defined by a laser distance measurement device and cross checked with a tape measure. To calculate from the measured liquid level at the calibration site in Garching, to the liquid level at the detector in Chooz, one has to consider liquid density and changes in the gravitational constant[1]:

$$h_{Chooz} = \frac{\rho_{Garching}}{\rho_{Chooz}} \frac{g_{Garching}}{g_{Chooz}} \cdot h_{Garching} \tag{4.1}$$

h_p is the liquid level at Garching or Chooz respectively, $\rho_{Garching}$ the liquid density during calibration, ρ_{Chooz} the final liquid scintillator density and g_p the gravitational constant at each site. While the uncertainty on the gravitational constants can be neglected, the uncertainty for h_{Chooz} is

$$\delta h_{Chooz} = \frac{g_{Garching}}{g_{Chooz}} \sqrt{\left(\frac{1}{\rho_{Ch}} h_{Ga} \delta\rho\right)^2 + \left(\frac{\rho_{Ga}}{\rho_{Ch}^2} h_{Ga} \delta\rho\right)^2 + \left(\frac{\rho_{Ga}}{\rho_{Ch}} \delta h_{Ga}\right)^2} \tag{4.2}$$

with $\delta\rho = 0.001\,\mathrm{g/cm^3}$ the uncertainty for liquid density measurements in Garching and $\delta h_{Ga} = 2\,\mathrm{mm}$ the estimated uncertainty of the laser distance measurement. The uncertainly of the ADC value (± 1 systematical plus statistical uncertainty from multiple records) is taken into account in the final linear fit to the recorded data.

The described calibration procedure was done first with water in the stairwells to a height up to 6 m. For a cross-check, the same calibration has been repeated with mineral oil, which had a similar density as the liquid scintillator in Chooz. Here, up to a maximal height of 1.8 m, the same procedure was applied. Both calibration liquids showed a good agreement between the final fit values. In the example of the MV sensor and calibration with oil, the results are shown in figure 4.3. On the left side, the calculated liquid level in Chooz from equation 4.1 over the recorded ADC values is plotted, while the errors are too small to be visible. To make them visible, the difference between fit function and calculated data points is shown on the right side. All values are well below the required precision of 1 cm.

As described above, the HPS is able to compensate changes in liquid temperature. The needed temperature sensor for this compensation is included and can be read out separately. All HPSs were put together in a heated water bath to calibrate the temperature sensors against a thermometer. The uncertainty on temperature calibration is below 0.3 °C which allows observation of the evolution of liquid temperature in the detector over the year.

To allow an absolute and differential measurement between the detector volumes, the relative height difference between the sensors had to be determined. This was done during filling of the detector by cross checking with other level measurement devices (e.g. Laser) and comparing the measured value to an expected value. This value was calculated by the amount of filled liquid and the geometry of the detector.

[1] values taken from Gravity Information System provided by Physikalisch Technische Bundesanstalt [Ptb14]

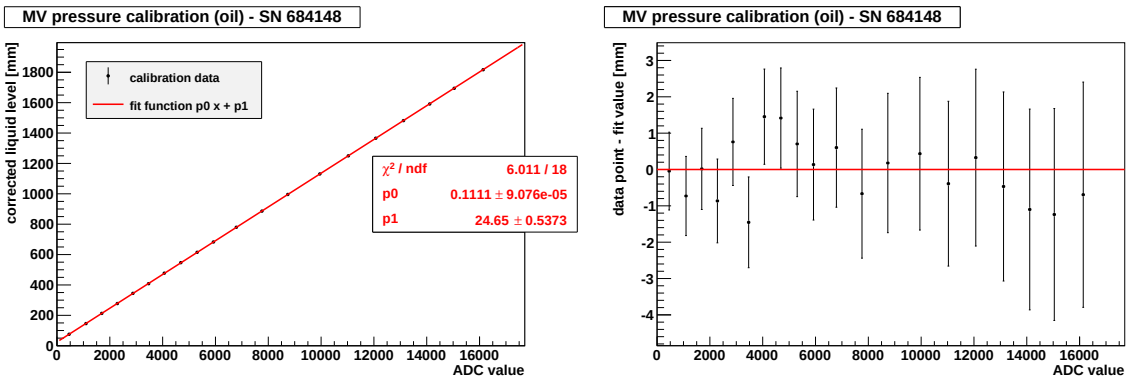

Figure 4.3: HPS calibration data in the example of the MV sensor. The ADC value of the electronics and the corresponding liquid level was recorded. The measured ADC values can be translated into detector liquid level by a linear function, extracted by a fit to the calibration data (left). To evaluate the goodness of the calibration, the differences between fit and data together with the calculated systematic errors are shown (right).

The GC HPS had to be installed during the construction because there is no direct access to the GC volume after the end of detector construction. Hence, the sensor was glued to the bottom of the GC vessel before it was mounted into the detector (see figure 4.4).

4.1.2 Gas pressure sensors

For the gas pressure measurement in the detector, a AP-47 sensor head [Key15a] and suitable amplifier from Keyence was used. The sensor itself has two inputs, one for high pressure and one for low pressure (see figure 4.5, left). It is designed to measure a positive difference between high and low input, but it is also capable of measuring a negative difference of a few millibars, too, which is enough for normal gas pressure in the Double Chooz detector. The connected amplifier has a display which shows the measured gas pressure. Since the calibration of the amplifier is unknown, an own calibration with the analog output of the amplifier was done and will be described below.
To monitor the gas pressure in the detector carefully, two kinds of measurement were performed. Each of the four detector volumes provided two access points to the gas phase. One was connected to the high pressure input of an AP-47 sensor, while the low pressure input was left open to the environmental pressure in the laboratory. In this way, the absolute pressure of each volume can be measured. The second gas pressure access was split right in front of the sensors, one was connected to low pressure input and one to the high pressure input of the next AP-47 sensor. This connection scheme is illustrated in figure 4.6. The pressure difference between adjacent detector volumes and, as a cross-check, the pressure difference between MV and NT are measured.

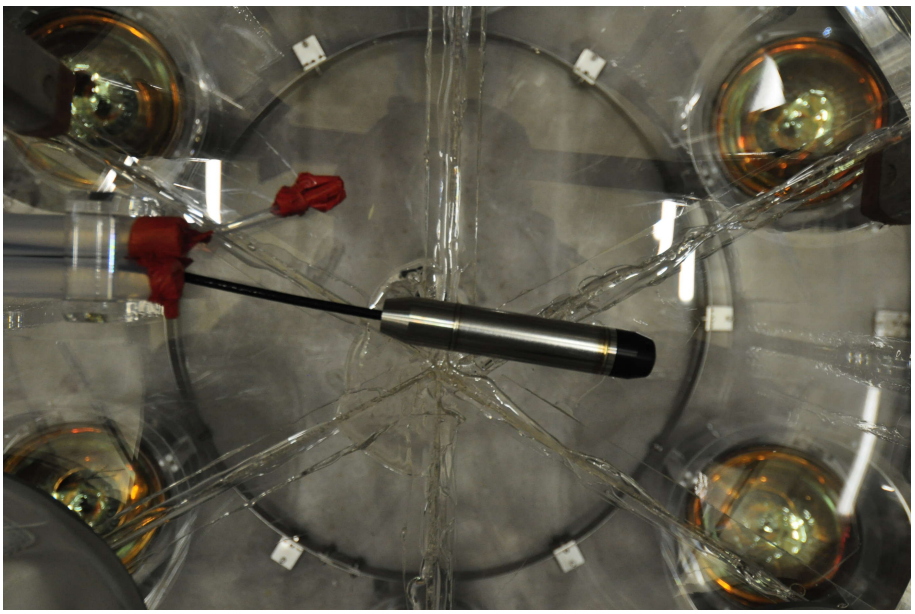

Figure 4.4: Picture of the GC HPS after installation. The sensor is glued to the bottom center of the acrylic vessel. On the left side one can see two PTFE tubes, filling tube and Loris Tube (see figure 4.1), together with a smaller tube for the cross reference system (see section 4.1.6).

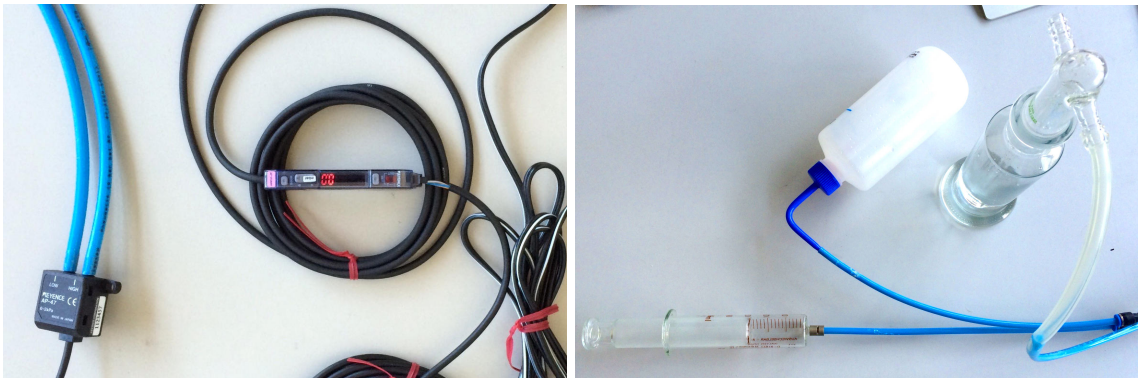

Figure 4.5: Picture of a AP-47 gas pressure sensor and its amplifier (left). The sensor has two connections for 1/4" pipes. One is for high pressure and one for low pressure. All eight sensors (4 absolute, 4 differential) were calibrated together. To cross check the pressure shown in the display of the amplifier and the measured gas pressure, the sensors were connected to a piston, a buffer volume and a bubbler (right). The pressure can be adjusted with the piston and the water level in the bubbler shows the actual value.

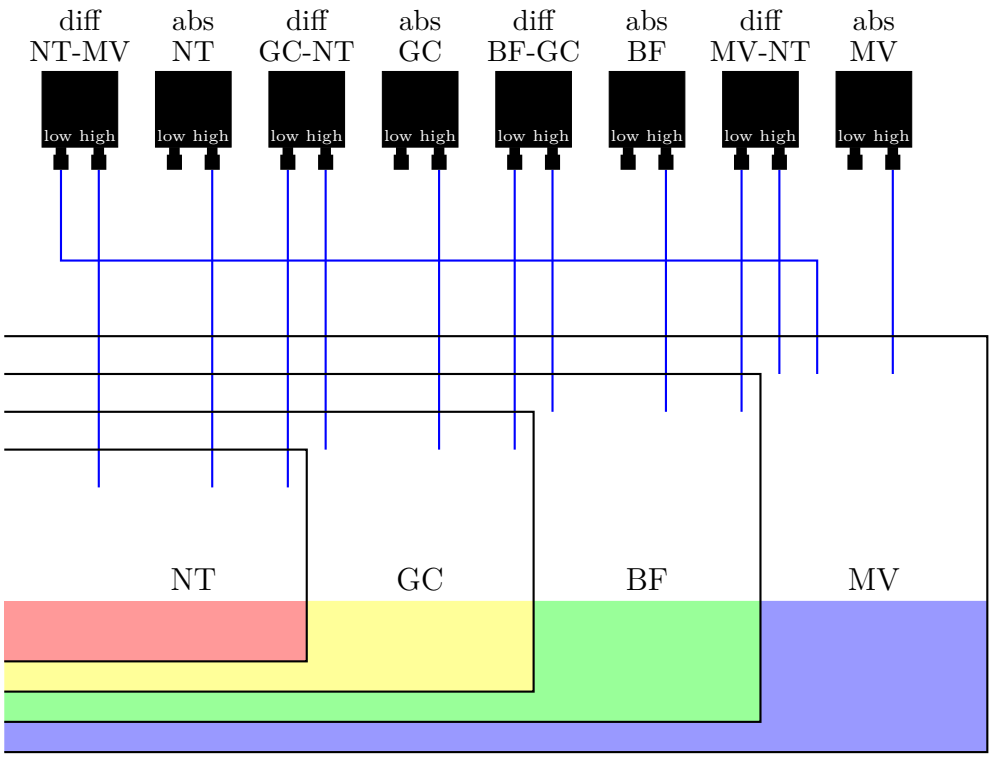

Figure 4.6: Schematic view of the gas pressure measurement in the detector. For each volume there is one AP-47 sensor measuring absolute gas pressure with high pressure connected to the volume and low pressure open to laboratory pressure. Four AP-47 sensors are connected to adjacent volumes to provide a differential gas pressure measurement across the detector: MV-BF, BF-GC, GC-NT and NT-MV.

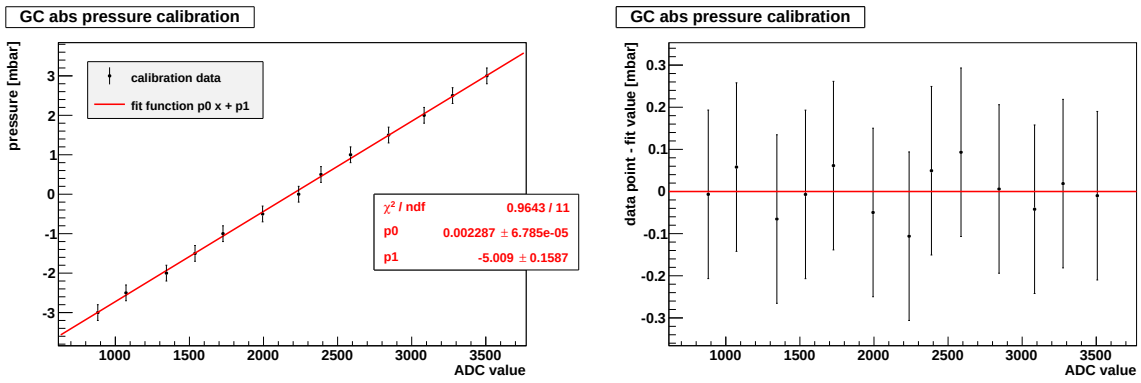

Figure 4.7: Gas pressure calibration data in the example of the GC absolute pressure sensor. The ADC value of the electronics and the corresponding calibration pressure was recorded and a linear fit was applied (left). To evaluate the goodness of the calibration, the difference between fit and data together with the calculated systematic errors is shown (right).

For the gas pressure measurement, the same high accuracy as for the HPS system is needed to ensure the security of the detector. Therefore a dedicated calibration was accomplished before installing the system at the near detector in Chooz. The high pressure input of all eight AP-47 sensors was connected to a piston, a buffer volume and a bubbler (see figure 4.5, right). With the piston the calibration pressure can be adjusted. Because of the sensitivity of the sensors, a buffer volume was connected. Without the buffer volume, a proper manual adjustment would not be possible. The bubbler was filled with water and had ticks written on the inner tube. Starting with a zero reference (calibration system open to environmental pressure), different values of over- and underpressure were compared to the analog output of the amplifiers connected to the sensors. To ensure a linear response of the sensor through the point with zero pressure, the same calibration was repeated with the calibration system connected to the low pressure input of the sensors.

High pressure input and low pressure input calibration showed good agreement. It was found that the uncertainty for every sensor is around 0.2 mbar at maximum, which is well below the required precision of 1 mbar for the gas pressure measurement. A calibration data example for the AP-47 sensor which is used to measure the absolute gas pressure in the GC volume is shown in figure 4.7.

Besides the detector there is the XTOS, which consists of three expansion tanks with a gas phase separated from the corresponding one in the detector[2]. Additional three AP-47 sensors and their amplifiers are connected to measure absolute gas pressure of each volume. The calibration method and the uncertainties described above apply for these sensors, too.

[2] XTOS and detector gas phases are indirectly connected over a gas exhaust system. But due to the length of the tubes and unforeseen circumstances, pressure differences can occur and harm the detector. This requires monitoring of the XTOS gas phases.

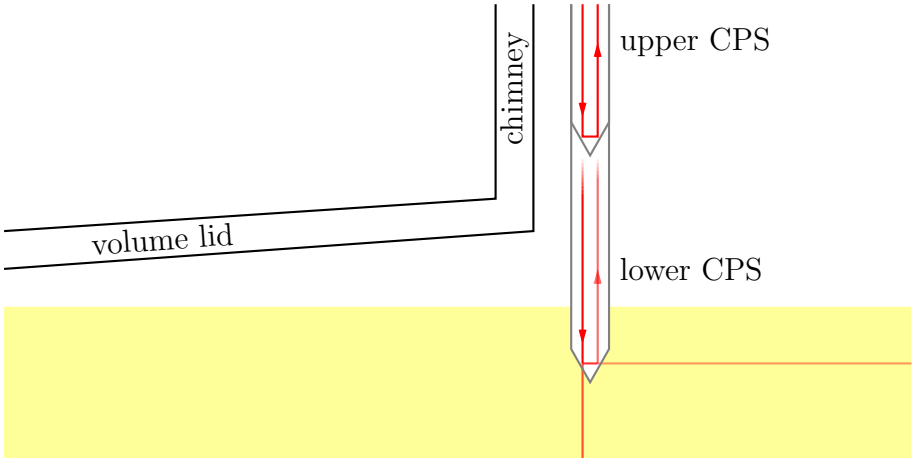

Figure 4.8: Schematic view of the critical point sensors (CPSs) in the detector for the inner two volumes, NT and GC. At the transition to the chimney, where the cross-section of the volumes decreases sharply, two sensors are mounted. One sensor 30 mm below the edge as prewarning and liquid level crosscheck and another one 10 mm above the edge. When liquid reaches the tip of the sensor, transmission increases which can be measured by the sensor over two optical fibers.

4.1.3 Critical point sensors (CPSs)

The access to the inner volumes of the Double Chooz detector is only possible trough a narrow chimney at the central axis of the detector. Because of this geometry, the transition between the cylindrical shaped NT volume and its chimney on top of it is very critical. The amount of liquid, which is needed to increase the liquid level for one volume by 1 cm, is directly proportional to the cross-section at this liquid level. In the NT volume roughly 40 l/cm are needed and in the NT chimney only 200 ml/cm, a reduction by a factor of 200. In other words, after filling 10 m^3 of NT liquid scintillator a batch of only 100 ml liquid will exceed the restriction of 1 cm difference in liquid levels. The second critical transition has to be resolved between the GC volume to the GC chimney.

To have a cross-check against the liquid level reading from other measurement systems and as a prewarning, a so called critical point sensor (CPS) was installed 30 mm below the transitions from NT volume to NT chimney. This sensor is referred to as lower CPS or CPS I. A second sensor was installed 10 mm above the transition, providing a clear mark that the critical transition was passed. The second sensor is referred to as upper CPS or CPS II. Figure 4.8 shows a schematic view and figure 4.9 a photograph to illustrate the positioning of the two CPSs. Again, the same applies for the transition from GC volume to GC chimney. The position of all four sensors is also illustrated in figure 4.1.

The model of the used sensor is FU-93Z, provided by Keyence [Key15b]. It consists of

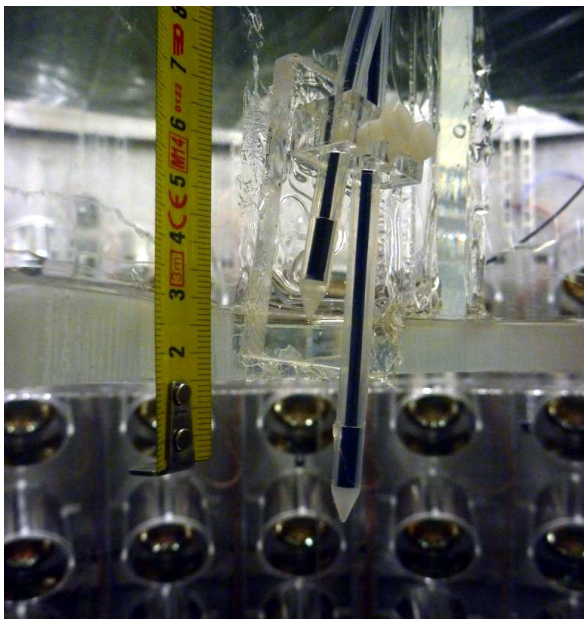

Figure 4.9: Picture of both GC CPSs after the GC chimney was mounted. The sensors are fixed in a holder made out of acrylics and PTFE screws. The lower sensor is mounted 30 mm below the edge as prewarning and liquid level cross-check and the upper one 10 mm above the edge.

a teflon tube with an outer diameter of 6 mm and a cone-shaped tip with 7 mm total height. Two optical fibers are fed through the teflon tube and are glued to the inner surface of the tip at the end of the teflon tube. While light is sent through one fiber towards the tip, one can measure the intensity of reflected light trough the second fiber. This is done by four corresponding amplifiers from Keyence connected to each CPS. If the refraction index of the medium around the sensor tip is changed, the intensity of reflected light will change due to changing reflection and transmission relation at the surface between sensor tip and surrounding medium. This is also illustrated in figure 4.8.
Since the intensity of reflected light also depends on the environment, no calibration is possible, nor is it needed for the critical point purpose. Thus, the sensors and the attached amplifiers were only tested for their functionality before installation at the detector site. After installation and still no liquids close to the sensors, the intensity of reflected light for all four sensors was measured and defined as 100 % intensity. After a CPS tip is surrounded completely by liquid, the light coming through the first fiber will be transmitted into the liquid almost completely. Almost no light will be reflected into the second fiber. This case is defined as 0 % intensity. In good approximation the range between 100 % and 0 % intensity corresponds to 0 and 7 mm liquid level relative to the pinnacle of the tip.
For a demonstration of the good resolution of a CPS within the dimension of the tip, data which was taken during the filling of the near detector is shown as an example.

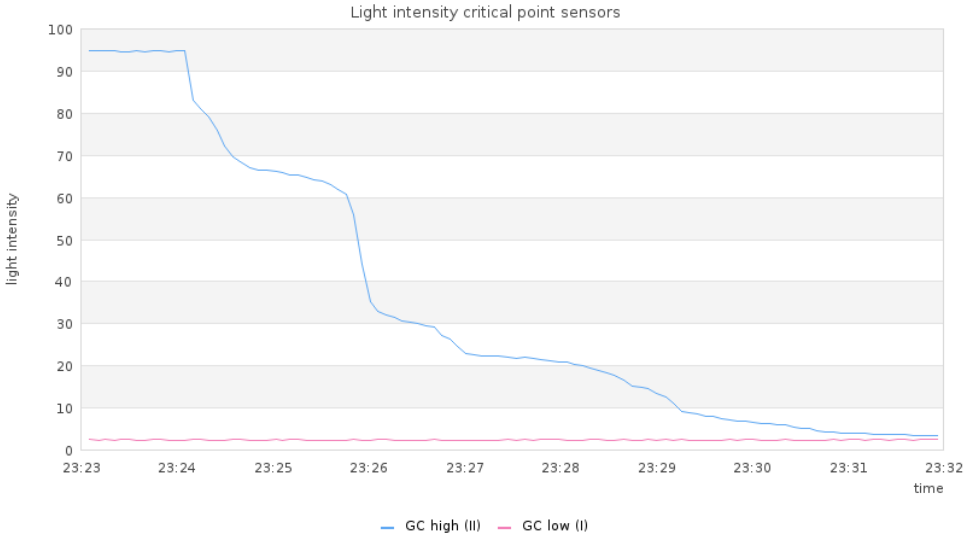

Figure 4.10: CPS transition in the example of the upper GC sensor. The data was taken during filling of the detector. The drop in intensity corresponds to a liquid level between 10 and 17 mm inside the GC chimney. One can see the good resolution of the CPS and the consecutive filling steps around this critical transition. For the filling of the chimney, only a predefined amount of liquid is step-by-step released into the volume.

In figure 4.10 the transition of the upper GC CPS is plotted. One can clearly see consecutive filling steps of the first liquid scintillator in the GC chimney. In contrast to the continuous filling of the GC volume, the chimney is filled in a so called fine filling mode. This means only a predefined amount of liquid is step-by-step released into the volume.

4.1.4 Laser sensors

Another direct measurement of liquid level for all volumes, except for the NT volume, is done with a laser distance measurement. For this kind of measurement, commercial products are available which are suited for the use in the Double Chooz LM system. The used sensor is M10L/100 from MEL [Mel15]. To measure distances up to 100 m, the M10L/100 uses comparative phase measurement with amplitude modulation. With this technique it is possible to detect unwanted reflections or other irregularities. The sensor has a serial RS422 interface for readout and configuration of the device. Several measurement modes and the startup conduct are selectable and there is also an error log.
To get a good target with high contrast for the M10L/100, a floater was used inside the detector. The floater was produced as turning workpiece made out of PTFE. To avoid flooding or even drowning, the floater was closed with a cap. On the outside several strips ensured low friction when the floater touches the wall (see

Figure 4.11: Floater as a target for the liquid level laser measurement. The turning workpiece is made out of PTFE and has very low mass due to its thin walls. It is closed with a cap to avoid flooding of the floater and has three strips on the outside to reduce friction in the guide tube (left). The upper surface for laser measurement is 40 mm above liquid level (right).

figure 4.11, left). The weight was only a few grams, therefore the waterline was very low. To determine the offset between liquid level and the upper surface for the laser measurement, the offset was measured in a glass filled with oil of the same density as the Double Chooz liquid scintillator (see figure 4.11, right). The upper surface was found to be 40 mm above the liquid level.

Of course, a floater with such low waterline needs guidance inside the detector. For all three volumes with laser distance measurement, MV, BF and GC, a guide tube was installed. For the MV volume the guide tube has direct access to the liquids, hence it is open at the bottom end. The BF laser guide tube was installed in the MV volume, too, but it was connected to the bottom of the corresponding volume. The same for the GC laser guide tube, but this time no connection to the bottom of the GC volume was possible. It would cross the BF volume and would have been connected to the acrylics vessel, both would be a technical difficulty. As a solution, an inverted syphon, called Loris Tube, was used to translate the GC liquid level into the laser guide tube mounted to the wall of the MV volume. This was already illustrated in figure 4.1.

The light sensor of the M10L/100 is right in the middle of the sensors cylindrical mounting connection, but the light emitting laser diode is sitting excentric besides the light sensor. For this reason the laser reflection point is slightly dependent on the distance to the laser sensor. The challenge was to keep the reflection point on the floater within an inner diameter of 5 cm over a guide tube length of up to 7 m.

To allow an accurate adjustment of the laser path, the laser sensor was mounted into a adjustable bush, which is connected to the laser flange with three screws. Between the flange and the bush, rigid expanded rubber enables slight and accurate changes in the direction of the laser path. To see the laser reflection point inside the guide tube, a solid and rigid extension was put between the detector and laser flange. This calibration construction is shown in figure 4.12. The clearance inside the extension allowed to use a small mirror to have a look inside the laser guide tube. For the bush adjustment a dummy PTFE floater was attached to a fishing line to adjust its position in the guide tube. Starting right below the extension, the reflection point was adjusted as seen in figure 4.12. Step by step the floater was lowered and the tilt of the laser sensor was readjusted to keep the reflection point on the surface of the floater. A further check was performed during recovery of the dummy floater. Most likely the laser path will not be exactly parallel to the guide tube, hence the reflection point will move when pulling out the dummy floater with constant velocity. If it moves only towards one direction the adjustment is fine, but if it moves to several directions during recovery, the laser is reflected one or more times on the guide tube wall.
Before installation in Chooz, the laser was tested paying attention on stability and reproducibility of the distance measurements. The M10L/100 showed its accuracy within $\pm 0.5\,\mathrm{mm}$.

4.1.5 Tamago

A special direct liquid level measurement system, called Tamago, was used for the NT volume. There is a direct access to the volume along the central axis of the detector from the top of the detector. But there is no practical solution to install a guide tube or something similar for a laser distance measurement. Moreover a measurement of hydrostatic pressure via a HPS to get a direct liquid level measurement is not possible due to material compatibility issues of the NT liquid scintillator with the stainless steel housing of the sensor. A precise and reliable system was needed because it was the only system measuring the liquid level directly. Besides this system a relative liquid level measurement was also possible (see section 4.1.6).
An adequate device was already used for the far detector level measurement: The Proservo NMS5 from Endress+Hauser [End15] (shown in figure 4.13) is a precision measurement device for liquid levels. The main part of the device is a stepper motor together with a sensitive balance enclosed in an explosion-proof housing. There is no hazard of explosions at the Double Chooz detector, but this specification allows to maintain a clean nitrogen atmosphere in the detector. Since the Proservo NMS5 has direct access to the NT volume this is mandatory. All electronics and control elements are also enclosed in the housing. A stainless steel drum with a thin teflon coated wire is connected to the stepper motor. In normal operation mode, the wire would never get in contact with the liquid scintillator, but in the unlikely event of a broken wire it would rest inside the detector and is therefore coated to ensure material compatibility. At the end of the wire a displacer, made out of PTFE, is

Figure 4.12: Installation and calibration of a laser sensor in Chooz. The laser sensor (blue box) is mounted in a adjustable bush. With screws, the surface perpendicular to the laser path can be adjusted accurately. For calibration, the laser flange with the adjustable bush is mounted to a solid and rigid extension. A dummy PTFE floater connected to a fishing line is lowered step by step into the laser guide tube. After each step, the laser path is readjusted until it is reaching the floater at the very bottom of the guide tube. Afterwards a PTFE floater without line was released into the guide tube and the laser flange was mounted directly onto the detector flange.

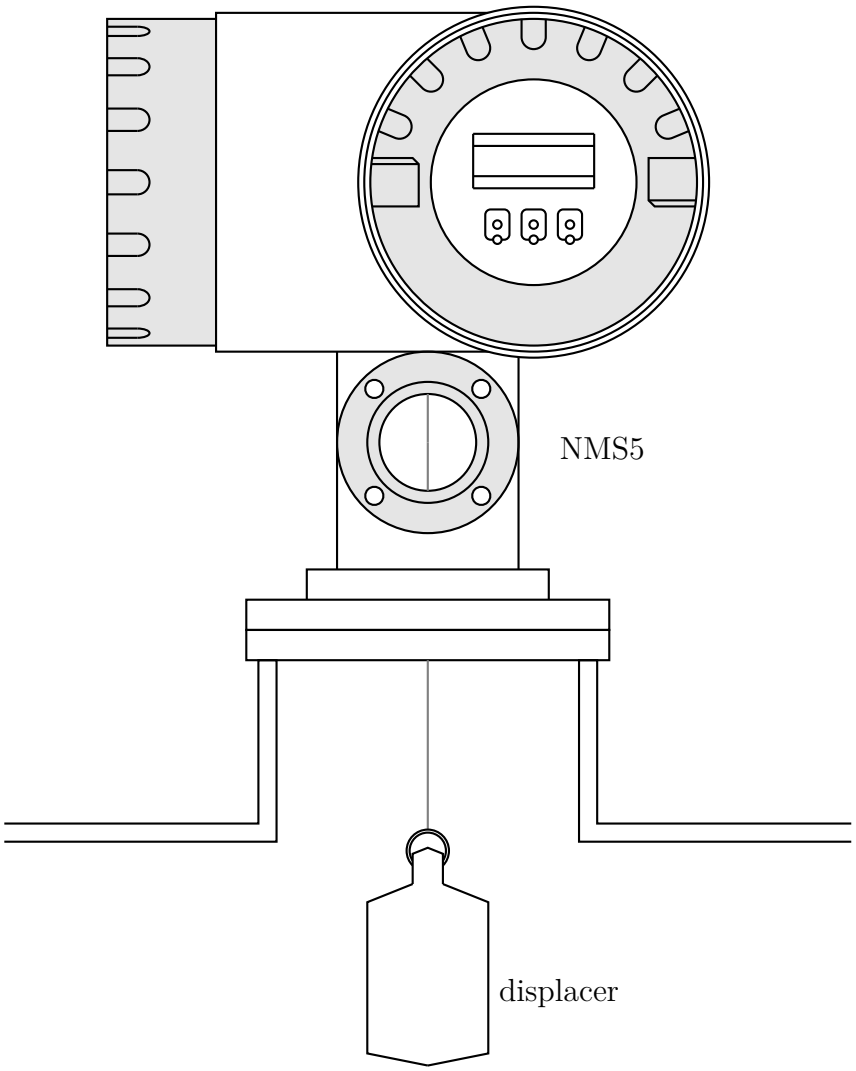

Figure 4.13: Schematic view of the Proservo NMS5. In the housing there is a stepper motor together with a sensitive balance. A stainless steel drum with a thin teflon coated wire is connected to the stepper motor. At the end of the wire a displacer, made out of PTFE, is connected. The liquid level will be measured by lowering the displacer until it touches the liquid. When dipping into the liquid, the balance will measure a reduced weight due to buoyancy. A fixed measured weight is programmed to the device, so the drum will be adjusted to follow this value. This means that the displacer has always the same water line and the liquid level can be measured with help of the stepper motor. According to the manufacturer this method has a precision of $\pm 0.7\,\mathrm{mm}$ [End15].

connected. The displacer mass and geometry as well as the weight per length of the wire and circumference of the drum were measured accurately by the manufacturer and were configured in the measurement device during installation. These parameters are crucial for a precise measurement with the measurement mechanism described in the following.
First prerequisite to get a precise liquid level measurement is the knowledge of the exact displacer position. Since the circumference is known and a stepper motor is used to move the drum, the position of the displacer relative to its resting position can be determined accurately at any time. Second prerequisite is the positioning of the displacer relative to the liquid level. The displacer will be lowered until it touches the liquid. When dipping into the liquid, the sensitive balance of the Proservo NMS5, displayed precision $\pm 0.1\,\mathrm{g}$, will measure a reduced weight due to buoyancy. The density of the NT liquid scintillator and a predefined weight, lower than the displacers actual one, are configured, too. Every time this fixed weight is measured by the balance, the water line on the displacer will be the same. In the scenario of rising liquid level, the measured weight of the displacer will drop. After exceeding the latency limit, the stepper motor will start to hoist the displacer up until the fixed weight is measured by the balance again. The manufacturer claims a precision in liquid level measurement of $\pm 0.7\,\mathrm{mm}$ for the displacer used in the Double Chooz experiment [End15]. This is well below the uncertainty of $\pm 2\,\mathrm{mm}$ on the offset calibration after the installation at the detector site (details on offset calibration will follow below).
The installation in Chooz can be seen in figure 4.14. An extension made out of acrylics and supported by a steel frame was used to mount the Proservo NMS5, to see the displacer at its resting position and to maintain a nitrogen blanket in the NT volume. A ball valve on top of the NT chimney allows access to the NT volume. The extension is mounted directly to the ball valve and is constantly flushed with nitrogen the keep a clean and oxygen free environment during deployment. The Proservo NMS5 was connected to a RS485 interface to read the current liquid level. A few basic commands to set the behavior of the device are also available for this interface.
The space along the path of the displacer is limited by the inner diameter of the NT chimney and the ball valve. A summary of all relevant values is shown in table 4.2. In addition to the displacer there are the two CPSs, a $^3/_4$" filling tube, a $^1/_4$" tube connected to the cross reference system (XRS), a temperature sensor from another group and some acrylics holding structure inside. Another complication is the construction of the drum. To keep the diameter constant, the drum has a helical grooving around the outside, which makes the displacer moving 10 mm perpendicular to the chimney axis. A study to find an optimal position and orientation for the Proservo NMS5 and to ensure a deployment without interference with the other systems was already done for the far detector [Fra11]. Since the near detector is identical to the far one in this context, the same position and orientation was used again.
After installation of the device, the distance between the Proservo NMS5 and the

Figure 4.14: Proservo NMS5 after installation at the detector. In the middle of the picture one can see a ball valve with a blue housing, which is mounted on top of the NT chimney. An extension made out of acrylics and supported by a steel frame is mounted on top of the ball valve. On top of the extension the Proservo NMS5 is mounted. All connections and the Proservo housing are sealed to maintain the nitrogen blanket in the NT volume. Near the black duct tape around the extension, there are two marks which corresponds to the lower tip and the waterline of the displacer at its resting position. The distance between NT volume bottom and upper mark was determined to be $6824 \pm 2\,\mathrm{mm}$.

part	diameter
displacer	50 mm
chimney, acrylics	150 mm
chimney, steel	150 mm
ball valve, clearance	90 mm
extension	100 mm

Table 4.2: Relevant diameters and clearances for the Proservo NMS5 displacer deployment. Compared to the outer diameter of 50 mm for the displacer, the space available on its path trough extension, ball valve and chimney is quite restricted. Beside that, the displacer will move 10 mm perpendicular to the chimney axis and shares the clearance with other systems.

bottom of the NT volume was not known with sufficient precision. Therefore the device was calibrated (offset calibration) using two different methods [Fra11]. In the first calibration, still without any liquids in the volume, the distance between the NT volume bottom and a mark at the displacer resting position was determined to be 6824 ± 5 mm. The water line on the displacer has a height of about 35 mm relative to its lower tip. That means, for liquid levels below 35 mm the Proservo NMS5 is not able to measure the liquid level with the built-in functions. Since the liquid level differences must be below 10 mm, this can not be accepted. By means of the sensitive balance, the liquid level can be calculated from weight measurement (displaced mass) as soon as the displacer touches liquid. This method and calculation was already described in [Fra11]. After the liquid level exceeded 35 mm, the Proservo NMS5 was switched to normal operating mode. At this point, the second calibration method using the amount of filled liquid and detector geometry was used. The absolute value of 6824 mm was unchanged, but the uncertainty was reduced to ± 2 mm.
At the end of the NT volume and the beginning of the chimney, the CPSs allowed a cross-check of the liquid level measurement. At activation of the lower CPS (CPS I) a liquid level of 2504 mm was expected [Buc14]. At this point the Tamago level measurement system showed exactly this value, demonstrating the goodness of the offset calibration and performance of the device.

4.1.6 Cross reference system (XRS) and Loris Tube

Another level measurement system, completely independent from other systems and without any electronics, provides a relative liquid level measurement for all four detector volumes. The name cross reference system (XRS) arises from this property. The measurement principle uses the fact that a common underpressure applied to different tubes submerged below several liquid levels, will lift each liquid level in the tube by the same height. This means, the liquid levels in the four detector volumes can be lifted up to a panel with scale above the detector while the level differences

stay the same and can be monitored on the XRS panel. It is not possible to get absolute liquid levels with this system, but it provides a relative measurement and a cross-check for the other level measurement systems.
A vacuum pump together with a manometer and a buffer volume are used to create underpressure. For deflating, the vacuum pump ventilation is connected to the nitrogen support in the laboratory to maintain a clean and oxygen free environment inside the detector. The buffer volume is needed to decouple the vacuum pump without any regulation from the system. In normal operation mode the buffer volume was evacuated or filled with nitrogen over the ventilation and the relative over- or underpressure was connected to the system with a needle valve. This allows a precise adjustment of the pressure in the system. In section 4.1.4 an inverted syphon, called Loris Tube, was mentioned to transfer the GC liquid level into a laser guide tube. Since this systems needs underpressure for initialization, too, it was included in the XRS panel and is connected to the same vacuum pump. The two systems can be separated and selected easily with valves. A schematic view of the two systems on the XRS panel can be found in figure 4.15. A needle valve is used to steadily inflate or deflate either the Loris Tube or the XRS. Because not all XRS tubes are submerged in liquid during filling of the detector, each tube can be closed separately.
During the construction of the near detector, one part of the Loris Tube and the GC XRS tube were already installed in the GC volume because there is no possibility to access this detector volume after construction. All further XRS tubes were installed afterwards through flanges. 1/4" PFTE tubes weighted down with PTFE pieces were used for this. A panel supporting the vacuum pump, the Loris Tube and the XRS was mounted on top of the detector (see figure 4.16). It was also important to have a steady increase in height between the detector flange and the connection to the panel. If this would be not the case, there is the risk of malfunction because of gas bubbles in the tube. The XRS showed an unstable behavior for detector volumes where the XRS tube was just submerged. This behavior is not understood but disappeared after further filling. After the liquid level reached a height of 10-20 cm above the end of the XRS tube, the system worked as expected.

4.1.7 Weighing cells

Temperature changes and corrsponding slight changes in the liquid density have dramatic effects on the liquid level in the ID volumes. This is caused by the small cross section in the chimney region. Expansion tanks in the XTOS act as buffer volumes for the inner three volumes of the ID after the detector is filled completely. The relation between the XTOS tanks cross section is the same as the relation between the liquid volume of the corresponding detector volumes. In this configuration, homogeneous temperature changes in the detector will lead to equal changes in the XTOS tank liquid levels.
To measure the liquid level for each XTOS tank they are mounted on four weighing cells each. The type of the cells is Z6 and the manufacturer is HBM [Hbm15a].

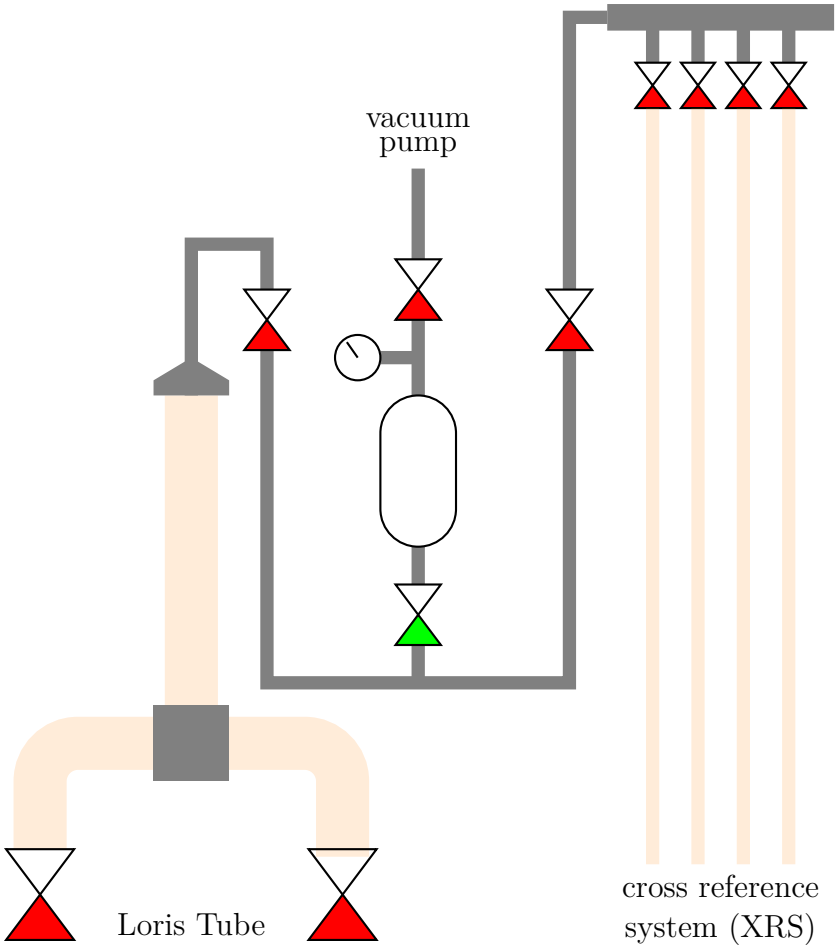

Figure 4.15: Schematic view of the cross reference system (XRS) and the Loris Tube. A vacuum pump with ventilation connected to the nitrogen blanket, a manometer and a buffer volume can be used for both systems. To steadily inflate or deflate the selected system, a needle valve (green) is used. The inverted syphon, called Loris Tube, is connected to GC volume on one side and to a laser guide tube on the other side. Four XRS tubes are bundled together on a scale for relative comparison. For filling steps with some volumes without liquid, each XRS tube can be shut off with a membrane valve (red).

Figure 4.16: Cross reference system (XRS) and Loris Tube panel after installation in the near detector laboratory. In the middle there is a buffer volume connected to a vacuum pump. The buffer volume can be connected either to the inverted syphon, called Loris Tube, (left side) or to the XRS (right side). The XRS consists of four tubes, which are connected to each of the four detector volumes, respectively. If the pressure is decreased in the distributor at the top, the liquid level can be sucked up into the transparent tubing on the panel and the levels can be compared relative to each other.

All weighing cells are connected to a controlling and monitoring device from HBM [Hbm15b]. There is a service interface with RS232 protocol, which was connected to the XTOS level measurement system. Unfortunately, only very few commands are available through the interface. It is possible to do a soft reset and to read the value of the currently selected and displayed weighing cells. But it is not possible to selected a group of weighing cells. The cells for the NT XTOS tank were selected and are integrated into the level measurement readout. The company, which installed the XTOS in the near detector laboratory, did a precision surveillance and determined an uncertainty of around $\pm 30\,\mathrm{g}$ over the whole measurement range. For all three expansion tanks, this precision is more than enough to measure liquid level differences in the XTOS tanks.

4.2 Used electronic modules

In this section only a functional description of each electronic module used in the Double Chooz LM system will be given. A detailed technical explanation of each electronic module and the underlying circuit can be found in appendix A.
Every part of the Double Chooz LM system has its own requirements to the readout electronics. The HPS module for example, needs only three input channels for hydrostatic pressure measurement but with highest possible resolution (16-bit ADC) together with three channels for temperature measurement in which lower resolution is sufficient (12-bit ADC). On the other hand, the gas pressure module needs 8 channels with medium resolution (12-bit ADC) together with 16 digital inputs which need to be decoupled electronically with optocouplers. For every measurement system there is a suitable module which was developed and produced specially for the different purposes. There is a common module for power supply, bus communication and voltage monitoring which can be connected to any of the sensor modules. Besides the sensor module, there are convertors for RS232, RS422 and RS485 serial interfaces used for the connection to Tamago, laser sensors and XTOS weighing cells.
The distance between the measurement computer and the sensors modules can exceed 15 m for some sensors. Therefore a robust and reliable connection was needed. Easily available and relatively cheap are standard Ethernet cables with RJ-45 plugs and different lengths up to 20 m. A standard Ethernet cable has four pairs of twisted wires, perfectly suitable for a bidirectional logic interface together with a field bus system, like controller area network (CAN), which is broadly used in the automotive sector. For the serial interface connections, the twisted wires pairs of the Ethernet cable are ideal, too. The two remaining cable wires are used for $+24\,\mathrm{V}$ power supply. At the master side of the bus, there is a multiplexer module which is able to switch between different measurement systems and to monitor the different power supply voltage levels.
Since the used electronic components and the production of an electronic module is relatively cheap, a sufficient amount of spare parts, and even enough modules to

Figure 4.17: After production and testing, the electronic modules were sealed in antistatic bags together with a tag describing their function and usage in the LM system (left). All spare parts were collected together in a sealed box to protect the electronics from the high humidity in the laboratory. Spare LM computers are also included (right).

replace the old LM system at the far detector in cause of a failure, were produced. The modules were hand-crafted, tested and sealed in antistatic bags together with a tag describing their function and usage in the LM system (see figure 4.17, left). Due to the high humidity in the underground laboratory in Chooz, the electronic modules and LM computers for replacement are stored in a sealed box in the laboratory (see figure 4.17, right).
Because of the high modularity of the LM system, even a person unfamiliar with the system is able to change parts of the system in the case of a failure. Even sensitive electronic components like ADCs are exchangeable because they are mounted on adapters. The different measurement modules are described below, the LM software and computer will be described in the following sections.

4.2.1 USB to I^{2}C adapter with real-time clock

The LM system can be connected using Universal Serial Bus (USB) for a high compatibility. An USB to Inter-Integrated Circuit (I^{2}C) adapter provides the needed connectivity. The main part of the module is an Atmel ATtiny45 microcontroller [Atm15]. On the one side it mimics an USB device using bit-banging, that means it just switches input/output lines in a software driven manner [Har15]. A library to use this device is already included in the most common linux kernels. On the other side, the ATtiny45 provides an I^{2}C interface, which can be accessed directly from the operating system with the included kernel module. I^{2}C was chosen because of

the broad variety of electronics components with I^{2}C interface, for example ADCs or multiplexer.
Besides the measured values of the connected sensors, a correct timestamp is important. To ensure to always have a correct clock, a real-time clock (RTC) with I^{2}C interface [Max15] is build directly onto the USB to I^{2}C adapter. Of course there are network time protocol (NTP) servers available in the internet or even in the computer network in Chooz, but in the case of network failure the LM computer can still use the RTC. In this respect, it is also important to note, that the LM computer does not have an own clock which would be conserved during a power cut. That means the timestamp of the measurement data would be wrong after every power cut in the laboratory. The RTC on the module has a battery included and will have the correct time even after longer power cuts. After restart of the LM computer, its internal clock will be synchronized with the RTC.
Another feature of the USB to I^{2}C adapter is an included temperature and barometric pressure sensor. The BMP085 from Bosch [Bos15] was used for this purpose. It is able to measure the barometric pressure with a precision of $\pm 0.2\,\mathrm{hPa}$ and the temperature with a precision of $\pm 0.1\,^\circ C$. This is more than enough for monitoring the environmental barometric pressure and the temperature near the level measurement electronics in the laboratory.
A picture of an USB to I^{2}C adapter is shown in figure 4.18. It has a standard USB type B connector and needs to be connected to $+5\,\mathrm{V}$ power supply. The 6pin boxed header together with a flat ribbon cable is used to share a common ground amongst the connected modules and for the two data lines of the I^{2}C bus.

see section A.1 for technical details

4.2.2 I^{2}C multiplexer with power supply over Ethernet

As mentioned before, I^{2}C was selected due to the broad variety of available sensors. A drawback of I^{2}C is that it was designed for usage within one circuit board or within one single device. It is not able to deal with longer wire distances because of the rising capacity. It is limited to a few meters with common clock frequency. This is far below the required 15 m for the installation in Chooz. A much better alternative for longer distances is the usage of bidirectional data transfer together with a controller area network (CAN) field bus. Bidirectional means, that instead of pulling a single line to 0 V or $+V_L$, two lines with V_+ and V_- are toggled. This signal is then transferred using CAN, not the specified protocol, but the hardware of the field bus. CAN is broadly used in the automotive sector and allows bus length up to 1 000 m with an appropriate clock frequency.
The multiplexer module is connected to the I^{2}C bus and is able to switch between four different channels. This is not only a matter of convenience because some electrical components with I^{2}C interface have a fixed bus address or a limited address range. If more components than available addresses are used within one system, a bus multiplexer is needed to switch between different bus branches. For each I^{2}C

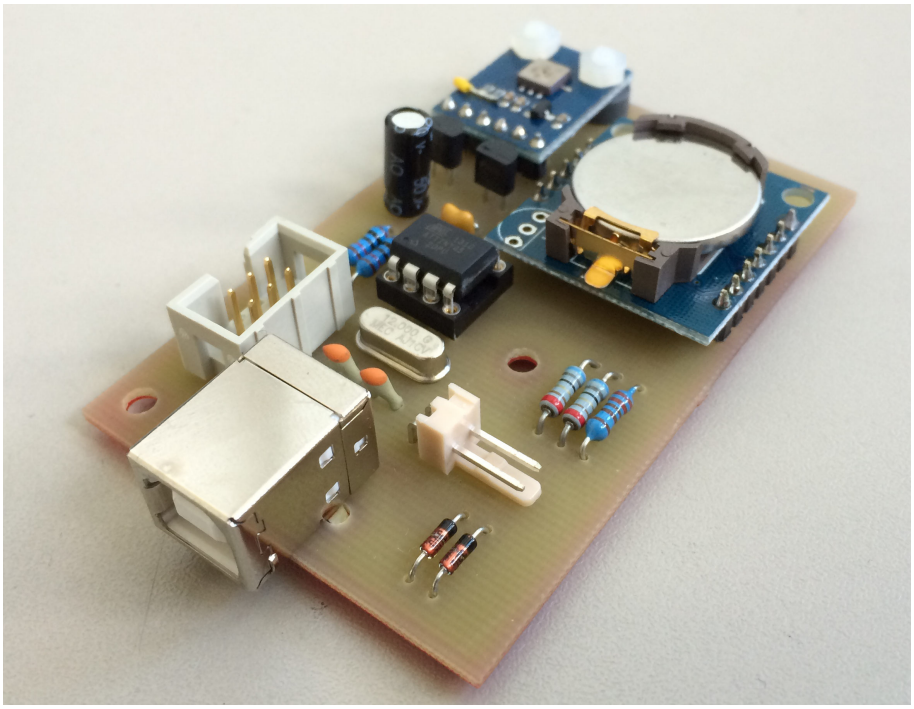

Figure 4.18: Picture of an USB to I^2C adapter. The communication between the two serial buses is managed by a small Atmel microprocessor. The module also contains a RTC to provide the correct timestamp for each dataset of the measurement system. For monitoring the environment, a precise pressure and temperature sensor is connected to the I^2C bus.

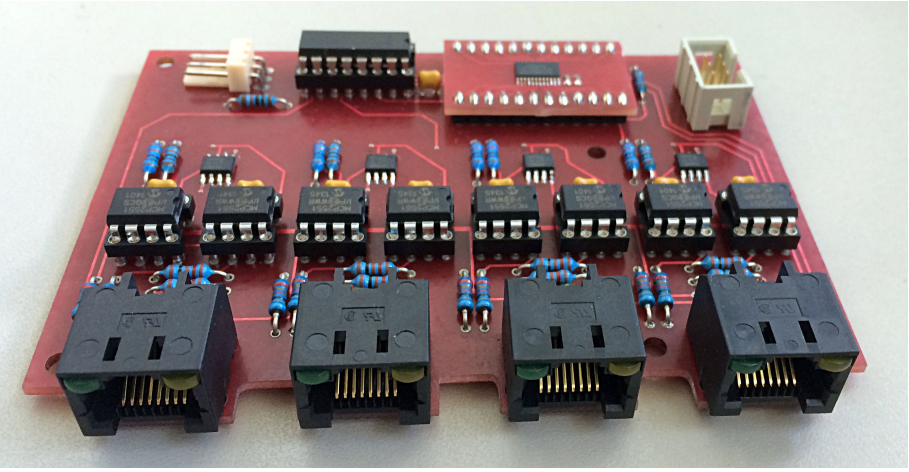

Figure 4.19: Picture of an I^{2}C multiplexer. A single I^{2}C serial bus can be switched between four channels. Each channel uses CAN hardware to extend the range of the bus and provides +24 V power supply over a single Ethernet cable. Light-emitting diodes (LEDs) indicate the selected channel and the status of the power supply.

channel the signal is converted to a bidirectional signal which will be transmitted using CAN hardware.
A picture of an I^{2}C multiplexer can be found in figure 4.19. The module needs to be connected to a power supply with +5 V and +24 V. The +5 V voltage is used for the electronics on the multiplexer module and the +24 V voltage is used as power supply for the connected sensor modules. It is connected to the I^{2}C bus over the 6pin boxed header. At the front there are four RJ-45 connectors which are used to connect several sensor modules. The connectors have two LEDs each, one group indicates if the +24 V power supply is activated for the corresponding connector and the other group of LEDs indicates which of the four channels is selected and can be accessed. The bus data lines (two times two twisted wires) and the +24 V power supply (two wires for GND and +24 V respectively) are connected to the eight wires of a standard Ethernet cable. This allows an easy and robust way to connect the sensor modules to the I^{2}C multiplexer module. This electronic module is normally used together with a USB to I^{2}C adapter (see section 4.2.1).

see section A.2 for technical details

4.2.3 CAN to I^{2}C converter with voltage monitor

After introducing the multiplexer module with conversion from I^{2}C to CAN on the master side of the LM system in the last section, the module used on the sensor side is described here. The same electronics as for the multiplexer are used to get back an I^{2}C interface on the module from the bidirectional interface provided over the

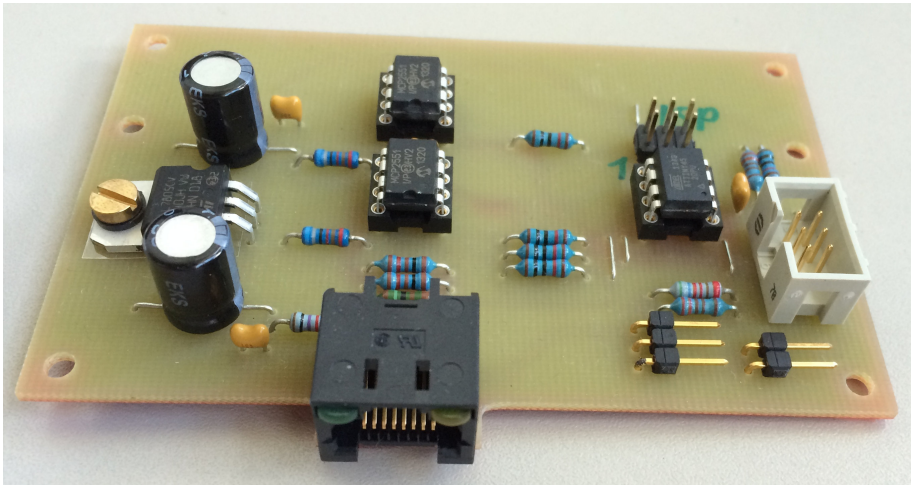

Figure 4.20: Picture of a CAN to I^{2}C converter. The CAN bus and power supply over a single Ethernet cable coming from the multiplexer module can be connected. The module provides +24 V for connected sensors and +5 V for electronics. A small Atmel microprocessor with two 8-bit ADCs works as a voltage monitor and the voltage measurements can be read directly over the serial bus.

Ethernet cable. Besides the +24 V power supply also provided over the Ethernet cable, which is passed to the sensors, a voltage regulator creates a stabilized +5 V power supply for the electronic parts on the sensor side. A LED at the RJ-45 connector indicates the status of the power supply over Ethernet.

An ATtiny45 microcontroller [Atm15] with two built-in 8-bit ADCs is used to monitor both voltage levels on the module. The microcontroller acts as a slave with I^{2}C interface and is able to send the monitored voltage levels over the serial bus. The I^{2}C interface and the device address is completely driven by software. An in-system programming (ISP) interface is used to connect the module to a computer. With the help of a Makefile, the firmware is compiled and transferred to the ATtiny45 microcontroller on the module. In case of address conflicts, the firmware could be changed without removing it from the LM system. Another feature is the possibility to detect if the module is connected to a serial interface which is currently selected by the multiplexer module (see section 4.2.2 for details). If this is the case and the CAN to I^{2}C converter is connected to the I^{2}C bus on the master side, the ATtiny45 indicates the selection with driving another LED at the RJ-45 connector.

A picture of a CAN to I^{2}C converter can be found in figure 4.20. The LEDs included in the RJ-45 connector, indicating power supply and serial bus connection, were used during the integration of the LM system and could be used for debugging. Both +24 V and +5 V voltage levels and the I^{2}C bus are passed to the sensor modules over the pin headers and the 6pin boxed header. The ISP pin header is only used to load the firmware onto the ATtiny45 microcontroller.

see section A.3 for technical details

4.2.4 ADC module for hydrostatic pressure sensors

For the HPSs (see section 4.1.1) a module with high ADC resolution was needed. Every HPS has a special measurement range fitted for each detector volume. Since the manufacturer only allows rough steps in the measurement range for ordering, every sensor has a different region in the ADC range which it will cover during filling from empty volume to full filling height. To have an ADC resolution which corresponds to less than 1 mm of liquid level for every sensor, which is well below the noise of the HPS amplifier, a 16-bit ADC was used to get the desired resolution. Although only three sensors are used for the Double Chooz LM system, MV, BF and GC volume, the module has four channels to have a spare connection. For every channel there is a separate 1 channel 16-bit ADC which is connected to the I^2C bus. Besides the measurement of hydrostatic pressure, the HPSs are able to measure the liquid temperature. Since this parameter is not important for the LM system and the resolution of the temperature amplifier is much worse than for hydrostatic pressure, it is only used for reference. A multichannel 12-bit ADC is enough for this purpose and is included on the module for temperature measurement. It is also accessible over the I^2C interface.
This electronic module is normally used together with a CAN to I^2C converter (see section 4.2.3). The converter provides connection to the master of the serial interface and the power supply for the electronics on the module and the connected sensors. A picture of an ADC module for HPSs can be found in figure 4.21. The terminal block in front has four groups for every channel, two connectors for power supply, one for 16-bit resolution hydrostatic pressure measurement and one for 12-bit resolution temperature measurement. The pin header is used for power supply and the 6pin boxed header for the serial interface of the connected CAN to I^2C converter.

see section A.4 for technical details

4.2.5 ADC module for gas pressure sensors

The noise of the gas pressure sensor amplifiers and the uncertainty of the calibration is relatively high compared to the measurement range of the gas pressure sensors. Therefore, there are no hard requirements for the resolution of the ADC module for gas pressure sensors. To maintain highest compatibility, the multichannel 12-bit ADC from the electronic module for HPSs was used again, providing sufficient resolution. The ADC values for all channels can be read over the I^2C interface.
Another feature of the gas pressure sensor amplifiers are so called hardware triggers. It is possible to define two gas pressure values and the behavior of two digital outputs. They can be used to trigger either a rising or falling edge on the digital output if the predefined value is reached. For the Double Chooz LM system, the amplifiers for absolute pressure measurement were configured to pull one output high, if the

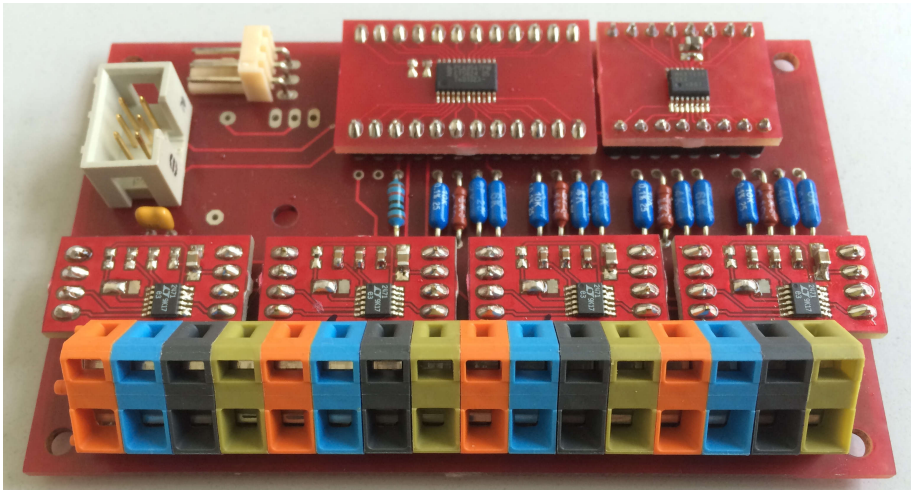

Figure 4.21: Picture of an ADC module for hydrostatic pressure sensors. The ADC module is connected to the power supply and I^2C bus of a CAN to I^2C converter. The module is able to provide +24 V for connected hydrostatic pressure sensors. It reads the hydrostatic pressure with 16-bit ADCs and the liquid temperature with a multichannel 12-bit ADC for each sensor.

measured value exceeds 3 mbar. For differential pressure measurement, two outputs were used indicating if the gas pressure difference dropped below -1 mbar or if it exceeded +1 mbar. This means, in normal state all hardware triggers are pulled low. All hardware triggers are monitored by a separate part of the ADC module for gas pressure sensors. Since there can be fast changes in the detector gas pressure due to changes in the nitrogen support or due to weather changes, this could be used to trigger a signal or horn independently from any value readout or measurement software. During the filling of the Double Chooz detector this option was not used, only the measured gas pressure values shown in the monitoring software were used. The hardware triggers were monitored using two I^2C port expanders with eight digital inputs each.

A picture of an ADC module for gas pressure sensors can be found in figure 4.22. The module consists of two parts which are stacked together using straight connectors. The smaller upper part is used for the gas pressure sensor power supply. Due to limited space, two sensors are sharing one power supply group on the terminal block. The green connectors of the upper terminal block are connected to the ADC for gas pressure measurement. The bigger lower part including a terminal block with black and gray connectors is used to read the hardware triggers. Although only twelve hardware triggers are used (4 absolute pressure triggers, 8 differential pressure triggers), all sixteen hardware triggers can be connected to the ADC module. The 6-pin boxed header of both module parts are connected to a CAN to I^2C converter (see section 4.2.3) over a ribbon cable. The pin headers are connected to the power

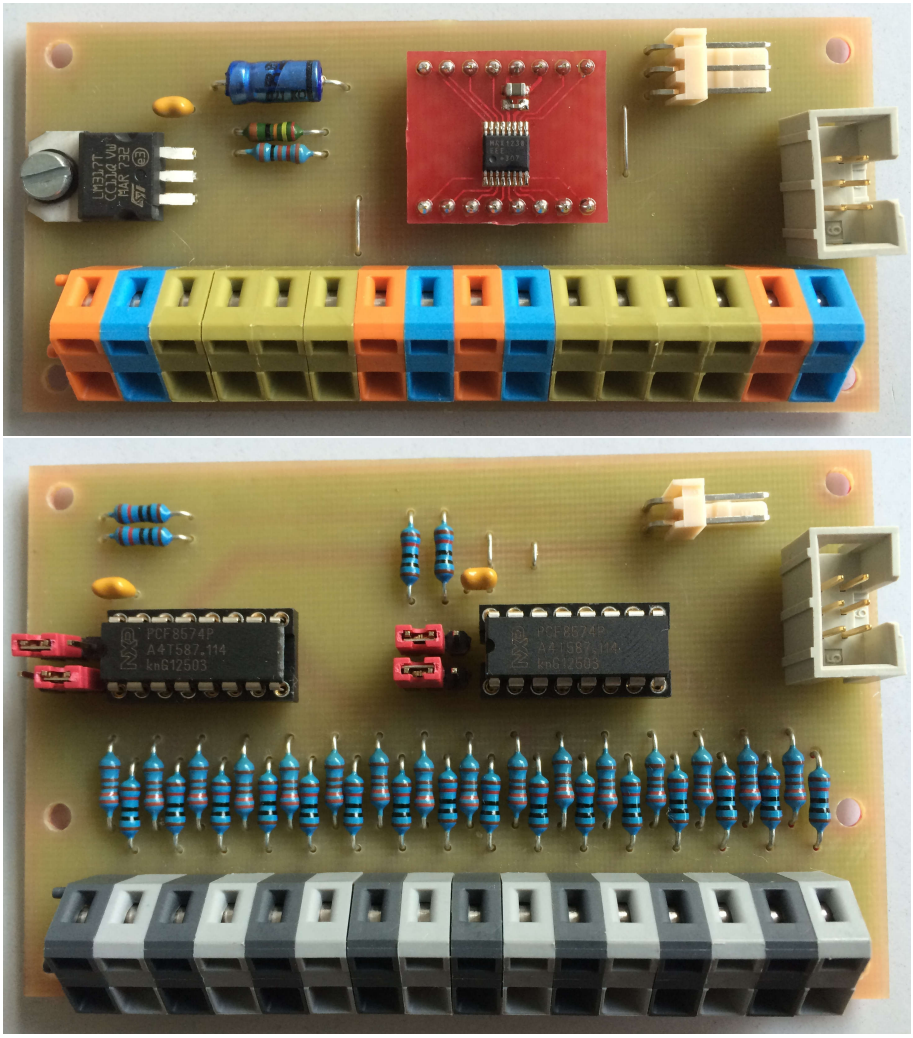

Figure 4.22: Picture of the two parts of an ADC module for gas pressure sensors. The two printed circuit boards (PCBs) are stacked together to a single component, which is connected to the power supply and I^2C bus of a CAN to I^2C converter. The module is able to provide +24 V for the connected gas pressure sensors. It reads the gas pressure with 12-bit ADCs (upper part) and the hardware triggers (lower part) for each channel.

supply of such a converter.
As an example, the setup for the gas pressure measurement is shown in picture 4.23. A housing includes all electronics, the gas pressure sensors and their corresponding amplifiers. All other measurement modules are constructed in a similar way.

see section A.5 for technical details

4.2.6 ADC module for critical point sensors

To monitor the transition of a CPS (see section 4.1.3), very little resolution is required for the corresponding ADC module. As before, to maintain highest compatibility, the multichannel 12-bit ADC from the electronic module for HPSs was used with sufficient resolution. Only one channel for each of the four sensors, GC CPS I, II and NT CPS I, II, is used on this module. The ADC values for all channels can be read over the I^2C interface.
The CPS module has the same feature of hardware triggers as described above for the gas pressure ADC module. But this time there is only one digital output available for every amplifier. The trigger was configured to stay low until the measured intensity drops below 90 %. This means that during filling of the Double Chooz detector the digital output is pulled high as soon as roughly 10 % of the height of the sensors tip has contact to liquid. This can be compared to a liquid level around 1 mm above the tip of the sensor. Besides the change in intensity shown in the LM monitoring software, this was used as second trigger in the region of the transition to the chimney. The hardware triggers were monitored using the same I^2C port expander as mentioned before.
Under certain circumstances, a problem could arise with the CPSs emitting light with high intensity into the detector. Normally this would be no problem during the filling process, but detector filling could have overlapped with PMT and electronics commissioning. Another possible scenario were interferences between the sensors due to reflections on the acrylics or the liquid surface. None of this problems were observed during the usage of the CPSs, but as a precaution, the ADC module was designed to have the ability to switch on and off every CPS independently. Since the I^2C port expander has four additional input/output ports, those were used as digital output to control the power supply for every channel. The port expander is reachable over the I^2C bus, so the power supply can be controlled even remotely without being on site.
A picture of an ADC module for CPSs can be found in figure 4.24. The terminal block in front has four groups for every channel, two connectors for power supply, one for 12-bit intensity measurement and one for a hardware trigger. The pin header is used for power supply and the 6pin boxed header for the serial interface of the connected CAN to I^2C converter.

see section A.6 for technical details

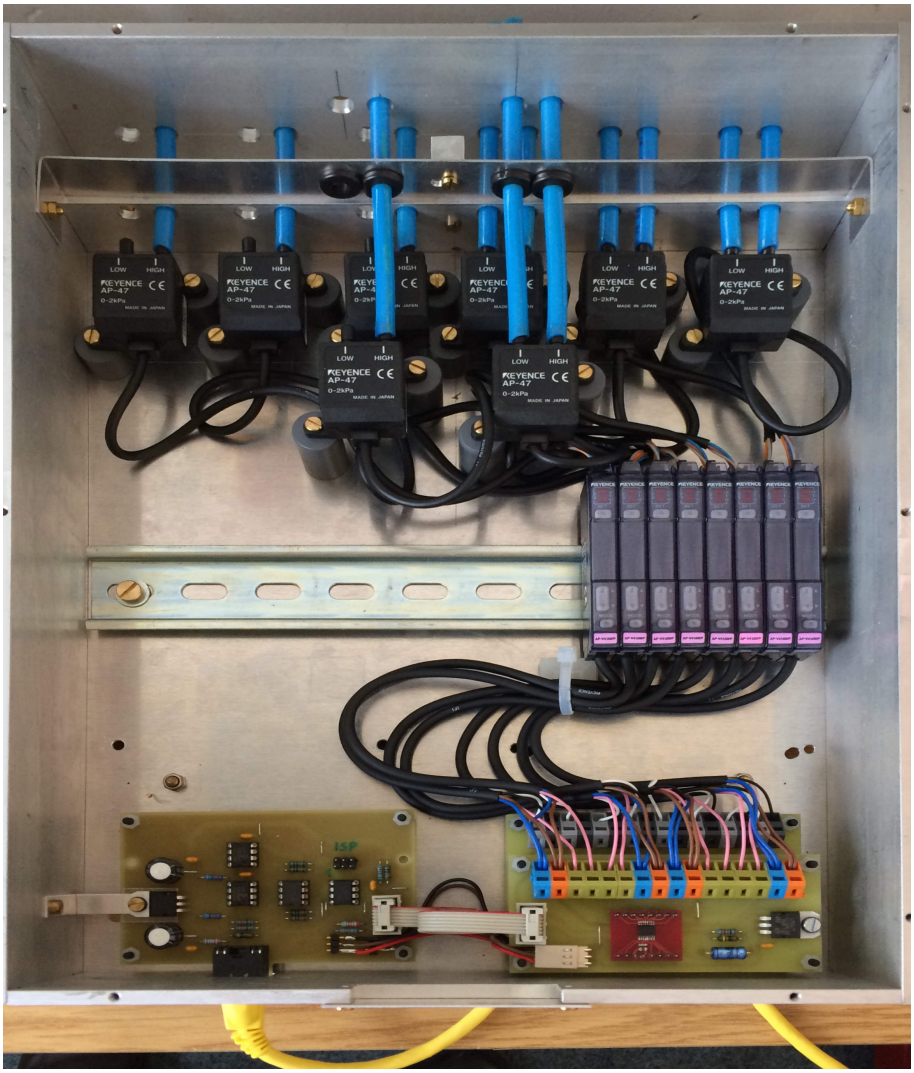

Figure 4.23: Picture of an assembled sensor module for gas pressure measurement as an example representative for other sensor modules. The sensor module is connected to a single yellow Ethernet cable providing power supply and serial interface connection. The PCB on the left side is the CAN to I^2C converter with voltage monitor (see section 4.2.3) with the voltage regulator thermally connected the the housing of the sensor module. The PCB on the right side is the ADC module for gas pressure sensors described in section 4.2.5. All three PCBs are connected over a ribbon cable for the I^2C bus and connectors for power supply. The eight AP-47 sensor heads (see section 4.1.2) and their amplifiers are also mounted inside the sensor module housing and are connected to the terminal blocks of the ADC module.

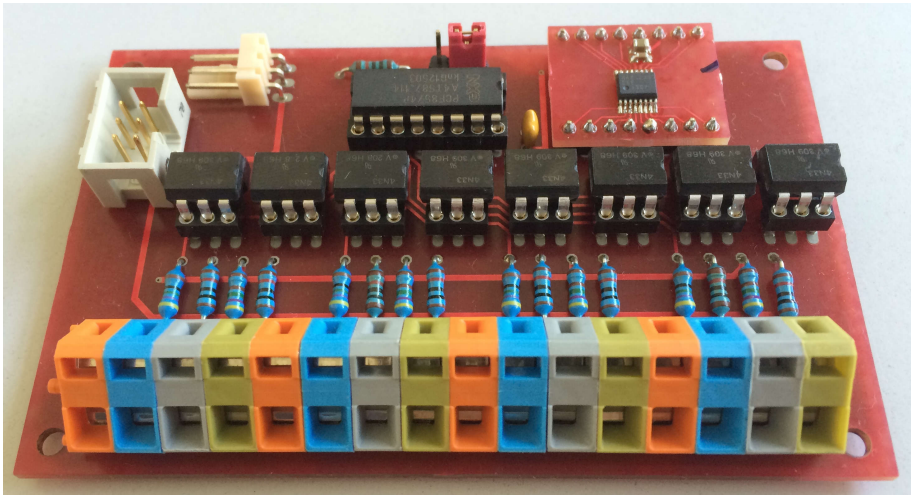

Figure 4.24: Picture of an ADC module for critical point sensors. The ADC module is connected to the power supply and I^2C bus of a CAN to I^2C converter. The module is able to provide +24 V for connected critical point sensors. It reads the reflection intensity value with a multichannel 12-bit ADC and the hardware triggers for each channel.

4.2.7 Further support modules

For the connection of laser sensors, Tamago and weighing cells, commercial USB to serial interface adapters were used. To use the same scheme with data lines and power supply over a standard Ethernet cable as described above, some small modules were used to ensure compatibility.
For example, figure 4.25 shows an USB adapter with four RS422 serial interfaces. A support module, including a +24 V power supply for the laser sensors, was mounted directly onto the interface adapter. On the other side of the connected Ethernet cable there is a box, connected to the laser sensor to provide power supply and the connection to the data interface of the sensor.

4.3 Measurement and monitoring software

4.3.1 Monitoring software

The design of the Double Chooz LM system required that the measurement values are stored in a MySQL database. Furthermore, all sensor calibration data and a timeline of applied offset corrections are stored in the database. It also includes correlations between the calibration and offset data and the plain measurement data. That means, the ADC values from the sensor modules are stored in the database and the measured value is calculated with the calibration data during the readout of the database. The calculation process needs only a small amount of resources, but

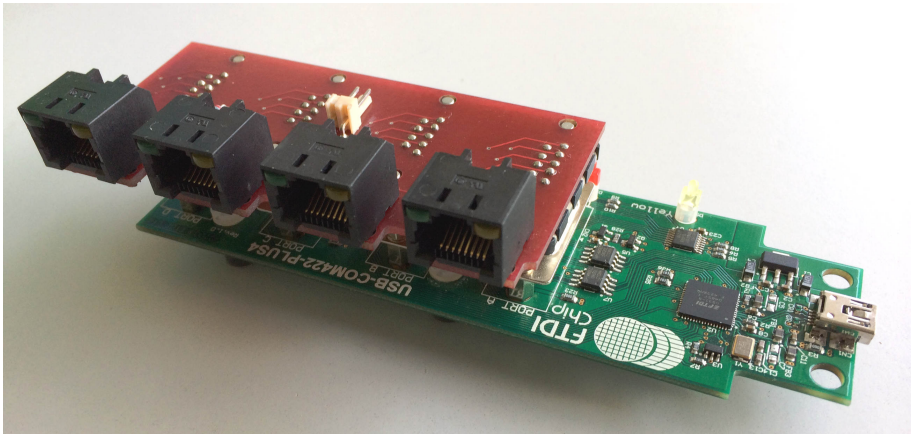

Figure 4.25: Picture of a support module for the connection of the laser sensors. A commercial USB adapter with four RS422 serial interfaces was used for connection to the laser sensors. To use power supply and data transfer over a standard Ethernet cable as for the other modules, a support module was mounted on top. The status of the +24 V power supply is indicated with the LEDs included in the RJ-45 connectors. LEDs for monitoring the data transfer for every interface are already included on the USB adapter and are not visible in this view.

provides full transparency for the measured ADC values and the offset corrections, which were applied during the filling process. Furthermore, the disk usage of the database decreases dramatically if only one or two bytes, instead of a floating point number, are stored for every measurement value. Besides that, groups of sensor channels and measurement systems were defined as well as descriptions of the sensors and groups, which can be read from the database together with the measurement data.

To link the physical level measurement system to the database, a framework called monitoring software was developed during this thesis. It was written in C++ and runs on the measurement computer. At first, the framework contains a class to communicate with the I^2C multiplexer, connected over the USB to I^2C adapter. With this class, the measurement computer is able to act as a master on the data bus, switch between the several subgroups of the network and to read and write data over the bus. Next, there are classes managing the connection to the serial interfaces also connected over USB. At last, there is a dedicated class for every sensor or I^2C device used in the LM system. Each class manages the initialization and configuration of the corresponding component and is able to send commands, e.g. switching the power supply of a CPS, or read the status, e.g. active hardware triggers, or get the measurement values from the sensors.

The main part of the monitoring software is a loop with a measurement timer. For each sensor or sensor group, an event is defined which can be attached to the

measurement timer together with a selected periodicity. The measurement timer will trigger a measurement for the corresponding sensor or sensor group when an associated event occurs in the loop. This improves the performance of the system and reduces the amount of stored data. For example, the detector gas pressure which can change quickly, was measured every 2 s, while the barometric pressure in the laboratory is measured every 15 min. Finally the measurement values are stored in the database by the monitoring software.

During the installation of the LM system, control over the laser sensors and the Tamago was needed. Of course, there is the possibility to control the devices by instruction over the command line of the measurement computer. But since the measurement computer is used as embedded system without a terminal, an inconvenient connection from another computer would be necessary. As a solution, a Python based control interface has been developed, which can be accessed by any smartphone being in the same network as the measurement computer. The interface accepts commands to turn the laser on or off, to move the displacer of the Tamago or gives back the current measurement value. It acts like a web server and can be opened simply with a web browser. As an example, this is shown in figure 4.26 for the Tamago control and monitoring interface. With this tool, a convenient working environment was possible during the installation of the laser sensors and the Tamago.

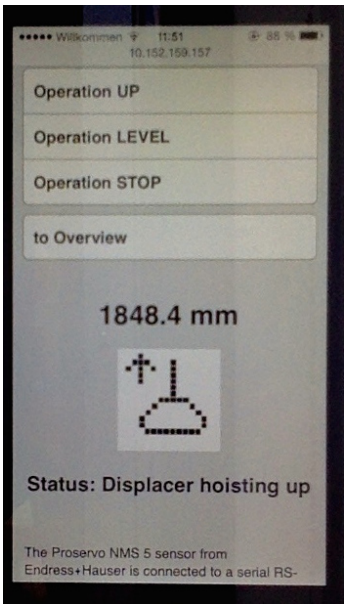

Figure 4.26: Control tool for the Tamago running on a smartphone.

All informations about the database structure, the latest version of the monitoring software and some needed software sources are stored in a subversion repository on a web server. That means, the setup of the database structure, the compilation of software dependencies and the installation of the latest monitoring software can be done automatically by running a dedicated script on the measurement computer.

4.3.2 Software for filling process

During the filling process of the detector, the shifters need direct access to the measurement data of the LM system. A computer called shifters PC was placed in the near laboratory which was used during the filling process. It was placed close to the DFOS for the case that the measurement values would indicate an intervention or stopping of the filling process.

An application based on C++ and Qt was developed during this thesis. It was installed on the shifters PC and had a connection to the database of the measurement computer over the network. The measurement data was requested from the

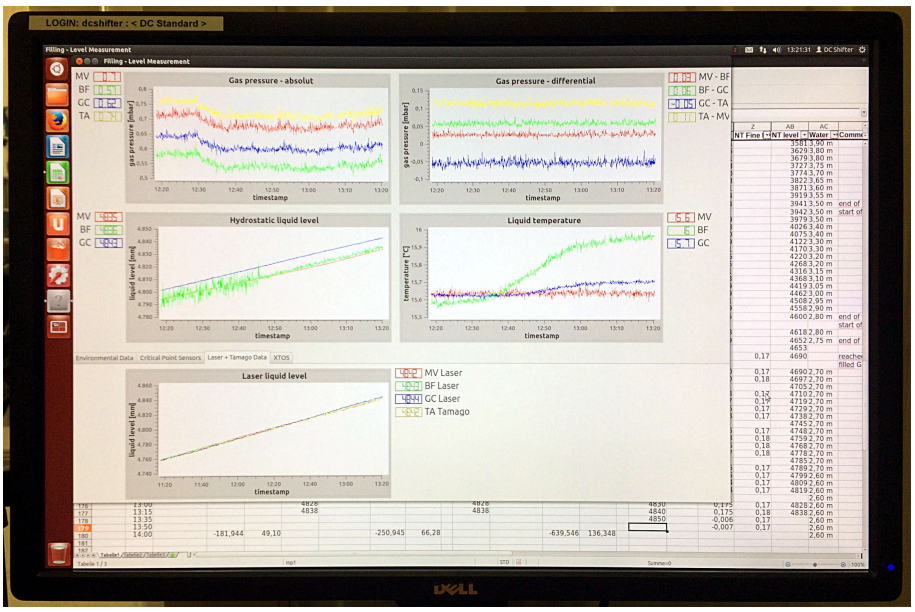

Figure 4.27: Picture of the monitoring for the filling process running on the shifters PC. The upper four plots show the time evolution of gas pressure, hydrostatic pressure and liquid temperature measurement values. In the lower part there are tabs to switch between other measurement values, in this example values from the laser sensors.

database, calibrated with the provided calibration data and was shown in real time[3] in the application. Not only the last measured value, but also plots to show the time evolution of a certain value were displayed (see figure 4.27). A toolbox was available for the shifters to evaluate or modify the displayed plots. The coordinates of every point inside the plot were displayed when the mouse cursor was placed over it and a zooming tool was available, for example. This application was used only during the filling process. For monitoring of the near detector measurement values, a different approach was used which will be explained in the next section.

4.3.3 Remote access and data backup

The LM computers[4], the shifters PC and a controllable power switch are connected to a network router. This allows communication amongst the components of the LM system without relying on the network infrastructure in the near laboratory. Since

[3] Some sensor data was recorded every 2 s and the database readout was performed every 2 s, too. In the worst case it could take up to 4 s until the current value is displayed.

[4] Actually there are two measurement computers. One is placed inside the laboratory close to the detector and the second one is placed inside the XTOS pit. One measures all detector related values and one XTOS related values only, but both systems work seamlessly together. In the filling or monitoring software they appear as one coherent measurement device. Even more measurement computers could be included in the measurement system.

the router is connected to the internet, all computers and interfaces are accessible remotely. The router manages all connections coming from the outside, providing access to the MySQL databases and to the computers themselves using SSH connections. The LM computers have a web server providing access to the measurement data over a common interface (see figure 4.28). However, this web server is not directly accessible from the outside and is only used for debugging or by the shifters PC inside the local network.
Every week, the database structure and the contained data is dumped into a backup file which will be sent to a server in Garching. The files are collected by the server and are stored in an incremental subversion archive as backup solution. This has the advantage of low disk usage due to the incremental storage because only changes to the previous version of the file are stored. Furthermore, it is possible to reconstruct every database state on a weekly basis.
Another flow of data is the mirroring of the database data to an external database, which is used for several other Double Chooz systems and which is easily accessible for Double Chooz collaborators over the internet. Due to some restriction from the host of the database, an adequate feature of the MySQL system could not be used for the mirroring. Therefore, a custom solution was developed to achieve this goal. Every two minutes, the difference to the previous state of the database is transferred to the external database. Compared to the 2 min measurement periodicity for the LM system in monitoring mode, this provides a de facto real time copy of the measurement value database. The server in Garching provides the identical web server as described above, but it reads data from the external database. Thus, the values from the Double Chooz near detector LM system can be accessed remotely by simply opening a dedicated website. This is a major improvement compared to the access over VNC as for the far detector LM system.

4.4 Level measurement computer

A picture of the assembled LM computer can be found in figure 4.29. It consists of several components which are mounted together in an aluminium housing. The main component is a credit card sized computer [Ras13] and an USB hub to increase the number of USB ports. To access the sensor modules, an USB to I^2C adapter together with an I^2C multiplexer is included. It provides four selectable channels, but only three were used: HPS module, gas pressure module and CPS module (only used during filling). The Tamago was connected using an USB to RS422 serial interface adapter, but since the Tamago was dismounted after the end of the filling process, this was also used only during filling. The three laser sensors were connected to an USB to RS485 serial interface adapter, but the GC laser sensor was removed after the filling process was completed, because the Loris Tube was dismounted, too. Only the MV and BF laser sensor stayed in place, but are turned off by default. They are only used for single measurements to cross check the liquid levels in MV and BF.

Gas pressure detector

	MV abs	BF abs	GC abs	TA abs	MV-BF diff	BF-GC diff	GC-TA diff	TA-MV diff
	mbar	mbar	mbar	mbar	mbar	mbar	mbar	mbar
2016-01-15 11:12:57	2.28	2.16	2.22	2.31	0.01	-0.04	-0.03	0.09
2016-01-15 11:10:58	2.27	2.13	2.21	2.28	0.01	-0.04	-0.01	0.07
2016-01-15 11:08:57	2.30	2.19	2.24	2.33	0.01	-0.03	-0.04	0.06
2016-01-15 11:06:57	2.26	2.15	2.20	2.27	0.00	-0.04	-0.03	0.08
2016-01-15 11:04:57	2.27	2.14	2.19	2.30	0.01	-0.04	-0.03	0.07
2016-01-15 11:02:57	2.20	2.08	2.13	2.22	0.01	-0.04	-0.03	0.07
2016-01-15 11:00:57	2.34	2.20	2.25	2.33	0.01	-0.04	-0.03	0.07
2016-01-15 10:58:57	2.31	2.16	2.22	2.31	0.01	-0.04	-0.03	0.08
2016-01-15 10:56:57	2.32	2.18	2.25	2.33	0.01	-0.04	-0.03	0.07
2016-01-15 10:54:57	2.29	2.16	2.22	2.30	0.01	-0.03	-0.02	0.08
2016-01-15 10:52:58	2.30	2.18	2.23	2.33	0.01	-0.04	-0.03	0.07
2016-01-15 10:50:57	2.28	2.16	2.19	2.29	0.01	-0.04	-0.03	0.07
2016-01-15 10:48:57	2.31	2.17	2.25	2.35	0.00	-0.03	-0.04	0.08
2016-01-15 10:46:57	2.31	2.16	2.23	2.31	0.02	-0.03	-0.04	0.09

Figure 4.28: Monitoring of the near detector measurement data using a web server. The data is requested from the database, calibrated with the provided calibration data and displayed on the website. A tabular view of the latest measurement values is provided as well as a plot to show the time evolution. Three different time spans can be selected (2 days, 1 month and 1 year) as basis for the showed diagrams.

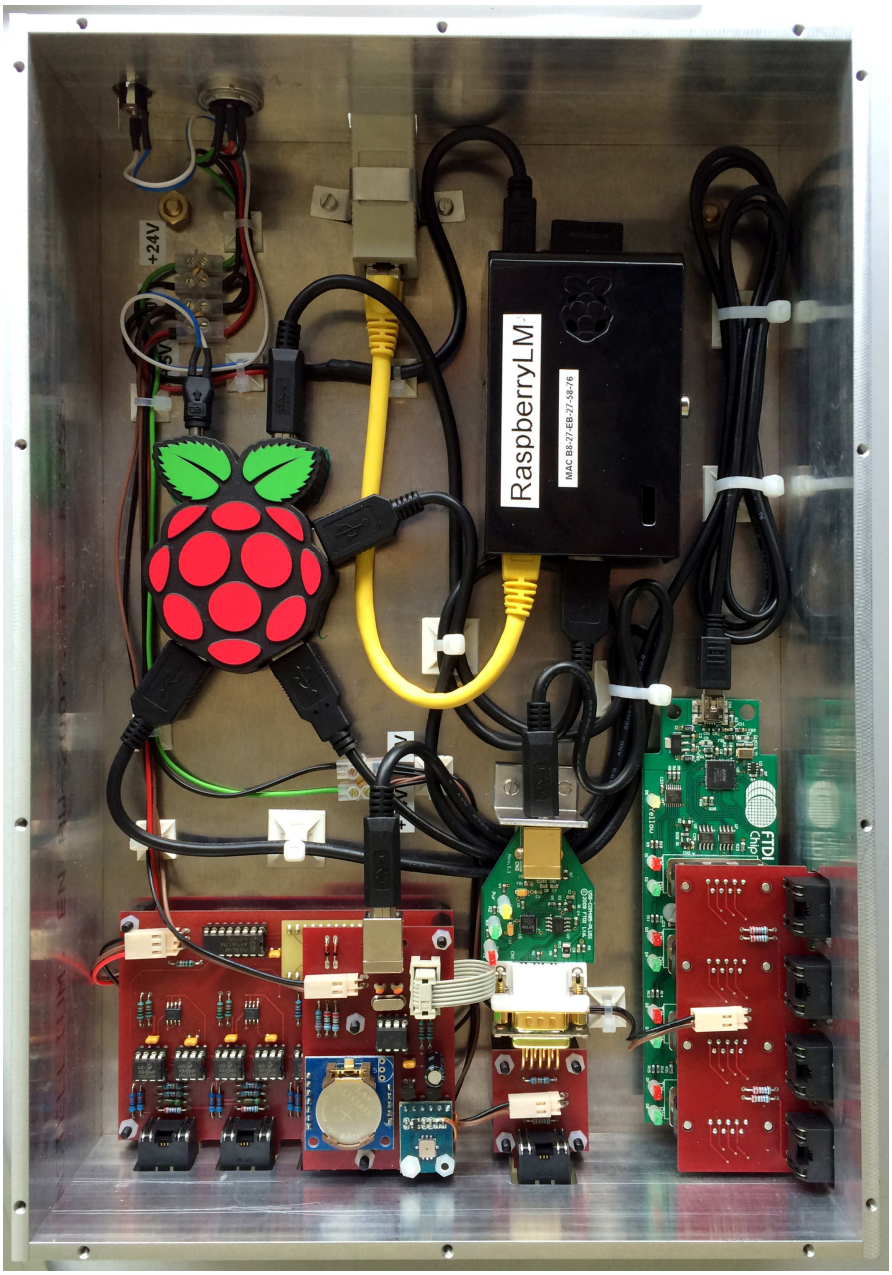

Figure 4.29: Picture of the LM computer. It consists of various components which are mounted in a housing. The credit card sized computer is contained in the black box labeled "RaspberryLM", which stands for the hostname of the computer. The part looking like a raspberry, is an USB hub to increase the number of USB ports. The PCB in the lower left corner is an I^2C multiplexer (see section 4.2.2) with an USB to I^2C adapter (see section 4.2.1) attached. The remaining two PCBs are USB to serial interface adapters, from left to right, one RS422 interface for the Tamago and four RS485 interfaces for the laser sensors.

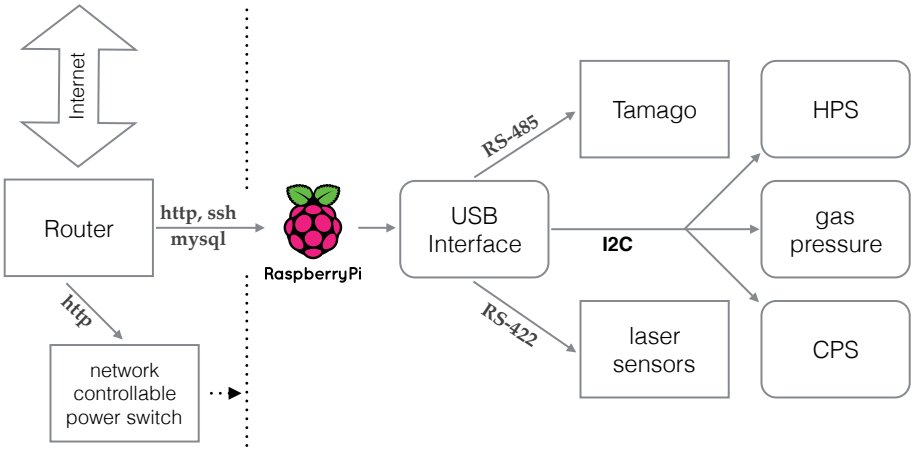

Figure 4.30: Schematic overview over the near detector level measurement system. On the left side, a network router manages the connections between the internet, a controllable power switch and the measurement computer. Over USB to I^2C, RS422 and RS485 adapters, all connected level measurement sensors are accessible. The layout can be extended with additional measurement computers by design.

The operating system for the measurement computer is a linux distribution with a customized kernel and runs completely from a SD memory card. This allows fast upgrading of the operating system and the measurement software as well as easy replacement in case of a failure. A memory card ready for use in the LM system can be created on a host system even by a person unfamiliar with the measurement system. On the host system, a script which was created specially for this purpose during the thesis, downloads the recent version of the linux distribution, recompiles the linux kernel to include the module for the USB to I^2C interface, compiles and installs all measurement software from a software repository and configures the measurement system. Therefore, a memory card with the operating system for the measurement computer including the newest version of the measurement software can be built from scratch automatically.

To achieve a high modularity and expandability of the LM system, the design was based on common interfaces and technologies. A schematic view of the underlying design concept can be found in figure 4.30. The whole system can be maintained completely remotely and can be repaired easily in case of a failure due to the high modularity.

The possibility of expansion was already used successfully. During the design and the building of the LM system, the XTOS was not part of the task. It was attached later on to include the weighing cells to the LM system and to add the measurement of gas pressure inside the XTOS tanks. A second LM computer with an USB to I^2C adapter, a gas pressure module and an USB to RS232 serial interface was built and connected to the router of the measurement system. The measurement data

Figure 4.31: Picture of the controllable power supply which can be switched over a network connection remotely. A stabilized power supply (hidden under the black coverage) provides +5 V and +24 V, used for the LM system, and +12 V which is used to drive a temperature-dependent cooling system. The LEDs in the front plate indicate the status of the power switch (red and green) and of the different supply voltage levels (yellow).

coming from the computer was seamlessly integrated in the existing system. The existence of more than one measurement computers will not even be noticed in the filling software or over the web server.

For the unlikely event of an unattainability of the LM computer due to problems in the operating system or in the already observed event of a blocked laser sensor interface, a hard reset of the LM system is required. That means, cutting the power supply of the system and restarting the whole system afterwards. A controllable network power switch is used for this purpose (see figure 4.31). It takes less than one minute from the power cut to the moment when all systems of the measurement system are recovered and the system is able to do measurements again. This was achieved because of the custom made electronics and the adapted operating system, which are prepared for an event like this. Besides this hard reset, an unexpected power glitch in the laboratory has the same effect on the system. This has already happened several times and proved the robustness of the designed measurement hardware.

4.5 Performance of the level measurement system

The completely new designed level measurement system presented here, proved its utilizability during the successful filling of the Double Chooz near detector. Because of the measurement system, it was possible to fill the detector in a secure manner and to comply with the hard restrictions on liquid level and gas pressure differences during the entire filling process. And even after filling, in monitoring mode, the system showed its reliability and its easy handling in terms of maintenance and remote access.
During the filling process, the system was extended to include parameters from the XTOS in the measurement system. And it was already necessary to switch the operating system for the measurement computer because of a corrupted memory card. The operating system and the monitoring software was built from scratch on a new memory card and it was installed successfully by a person unfamiliar with the measurement system. Several power cuts and network failures did not harm the LM system and did not result in any loss of data. All of these irregular occasions acknowledged the success of the design concept.

Chapter 5
5 Data Analysis

After data taking started with the Double Chooz far detector in April 2011, the near detector was finished in October 2014 and data taking started within this year. The analysis of data from both detectors enables a significant reduction of both reactor and detector related systematic uncertainties. But still, several sources of background have to be taken into account to allow a measurement of the neutrino mixing angle θ_{13} with the desired precision.
During the writing of this thesis, the first calibration campaign for the Double Chooz near detector was still ongoing. But it was possible to use a set of data which was taken during the first year of both detectors running, a period with around five months of data. In total 110.4 days of live time were used for the Bismuth-Polonium 214 and 212 coincidence analysis presented in section 5.1. It will be shown that the near Double Chooz detector is comparable to the far detector in terms of radiopurity. In section 5.2, a study regarding (α,n) reactions on ^{13}C as correlated background contribution in the Double Chooz far detector will be presented. It was not possible to do the same for the near detector with five month of data and without calibration. The energy scale and the trigger efficiency are very important for this type of analysis, both were not available for this thesis. Therefore only the analysis principle will be demonstrated using far detector data.

5.1 Bismuth-Polonium 214 and 212 coincidences

The analysis presented in this section will focus on the background induced by radioactivity in the near detector. The most important radioimpurities are isotopes included in the uranium and thorium decay chains as well as ^{40}K. Events originating from the β^--decay of ^{214}Bi and ^{212}Bi followed by the α-decay of ^{214}Po and ^{212}Po are referred to as BiPo coincidences. They provide a fast coincidence signal between β^- and α signal, which is also spatially correlated (see figure 5.1). It can be easily distinguished from other background contributions.

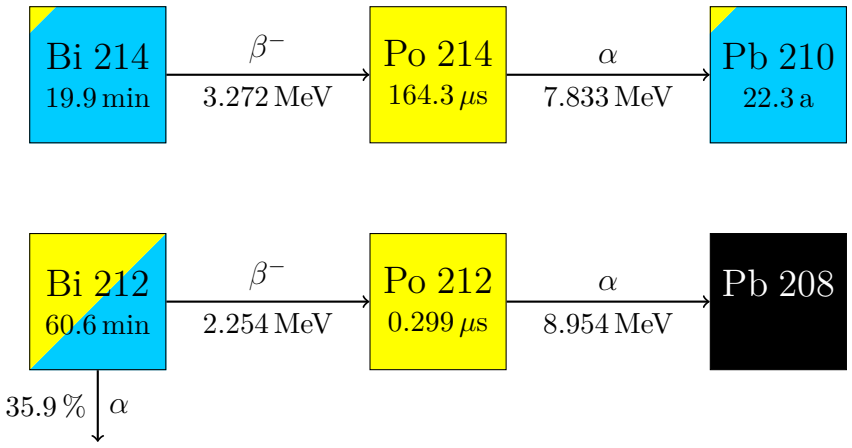

Figure 5.1: Excerpt from the ^{214}Bi and ^{212}Bi decay scheme which is important for the BiPo coincidences. The β^- decay of bismuth and the following α decay of polonium provide a fast coincidence signal for detection. ^{214}Bi also undergoes α decay, but only with a probability of 0.021 %, which can be neglected for this analysis. The same applies for ^{212}Bi, but this time the branching ratio of 35.9 % has to be included. Data taken from [Fir96].

Most of the decays of heavy isotopes coming from natural radioactivity are isotopes present in the ^{238}U and ^{232}Th decay chains (see appendix B). ^{238}U and ^{232}Th are both primordial isotopes. ^{238}U has a natural abundance of 99.3 % and ^{232}Th a natural abundance of 100 %. The short decay time of ^{214}Po can be used as coincidence measurement to tag the number of decays within the uranium decay chain. However, the radioactive equilibrium in this chain can be broken because of some isotopes with long life time such as ^{226}Ra with a half-life of 1 600 years. So, at least, ^{222}Rn and its daughters can be tagged with this method. The same applies for ^{212}Po and the thorium decay chain accordingly. Here no isotopes with long life time can break the radioactive equilibrium. Hence, the BiPo coincidence analysis provides a tool to prove the radiopurity of the Double Chooz detector.

5.1.1 Single event energy spectrum

During the first five month of data taking with the Double Chooz near detector, in total 110.4 days of live time were recorded. For the following analysis a prepared dataset with only single events was used. That means that events following a muon and events which have no physical origin, like instrumental light emission, were already removed [Nov15b]. Roughly $1.47 \cdot 10^8$ single events are available in this prepared dataset leading to a single event rate of 15.4 Hz in the near detector.
Figure 5.2 shows the energy spectrum for those single events in the region from 0 to 4 MeV. There are some features in the spectrum, the most dominant one around $\sim$2.6 MeV is most likely coming from the 2.615 MeV gammas of the ^{208}Tl decay.

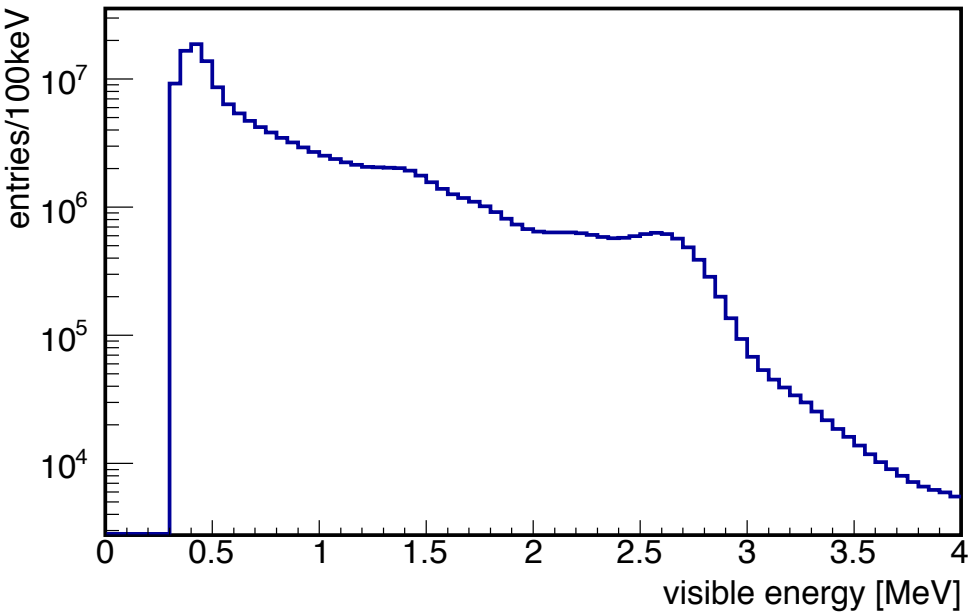

Figure 5.2: Single event energy spectrum of the used near detector data sample. The plot has a logarithmically scaled y-axis and shows the region with energies lower than 4 MeV. Below 0.5 MeV the events start to disappear because of the fading trigger efficiency. The excess at 2.6 MeV is most likely coming from the 2.615 MeV gamma emission of the ^{208}Tl decay.

Another gamma emission from the ^{40}K decay is expected at 1.460 MeV. Beside that the spectrum rises constantly towards lower energies, until the detector trigger efficiency drops at around 0.5 MeV. The dominant part of the single events is expected to come from radioimpurities inside the detector, mainly uranium and thorium and their daughter isotopes in the decay chain. Here, the BiPo coincidences are a suitable tool to determine the low mass concentration of radioimpurities coming from uranium and thorium.

5.1.2 Coincidence selection cuts

After cosmic muon events and their following events as well as light noise events, like instrumental light from the PMTs, were already removed from the used data sample, only selection cuts to extract the BiPo coincidences were necessary. The used selection cuts are summarized in table 5.1 and are explained in the following:

1. The prompt energy cut is searching for the β^--decay of bismuth. The Q-value for ^{214}Bi is 3.272 MeV and for ^{212}Bi it is 2.254 MeV (see figure 5.1). Since there is no notable quenching effect for electrons and gammas from the β^--decay, the upper energy limit is set slightly above the Q-value. This leads to an upper selection limit of 3.5 MeV for ^{214}Bi events and an upper limit of 3.0 MeV for ^{212}Bi events respectively.

	BiPo 214	BiPo 212
prompt energy (Q_β of bismuth)	1.0 to 3.5 MeV	0.5 to 3.0 MeV
delayed energy (Q_α of polonium)	0.2 to 0.9 MeV	0.35 to 1.2 MeV
time difference	6 to 2000 μs	0.5 to 5 μs
spatial difference	< 50 cm	

Table 5.1: Selection cuts for BiPo coincidences to extract BiPo 214 and BiPo 212 events from the used single events dataset. The choice of the values is explained in the text.

With some non-negligible probability, the β^--decay can reach the ground state of the polonium daughter nuclei. So, the visible prompt energy can go down to zero. Therefore, the lower energy limit should be set to the lowest possible energy without any influence of the detector trigger efficiency (see figure 5.24). In that case, 0.5 MeV as lower limit ensures a trigger efficiency of 100 % with negligible uncertainty. However, this limit was used only for ^{212}Bi. For ^{214}Bi the lower limit was set to 1.0 MeV to reduce accidental background events in this analysis. The large time window of almost 2 ms and the large number of single events below 1 MeV (see figure 5.2) would increase the accidental rate for BiPo 214 coincidences dramatically. For the same reason the upper energy limit was set very close to the β^--decay Q-value of ^{214}Bi.

For the evaluation of the cut efficiencies, the Monte Carlo simulation of the identical far detector was used. Under the assumption that the near detector is similar to the far detector in that point and with using the same cut values, the cut efficiencies from a former study regarding the radiopurity of the far detector was used [Hof12]. In this study the efficiency of the prompt energy cut was determined to be 84.3 ± 1.3 % for ^{214}Bi and 74.1 ± 1.5 % for ^{212}Bi. The cut efficiencies are also summarized in table 5.5.

2. The delayed energy cut is searching for the α-decay of polonium. The Q-value for ^{214}Po is 7.833 MeV and for ^{212}Po it is 8.954 MeV (see figure 5.1). But this time, a quenching factor in the order of 10 [Abe11] has to be taken into account for α events in the detector. In contrast to the continuous β spectrum of the prompt event, the visible energy of α events is only affected by the energy resolution of the Double Chooz detector. Therefore, narrow energy windows were chosen for the α events from both coincidences, 0.2 MeV to 0.9 MeV for ^{214}Po and 0.35 MeV to 1.2 MeV for ^{212}Po. The quenching factor is also different for GC and NT liquid scintillator, but for both volumes the visible α energy is included in the chosen energy windows.

Again, the cut efficiencies are taken from [Hof12]. Different values for GC and NT were found because of the different quenching factors. For the GC region the efficiency of the delayed energy cut was determined to be 100 % for ^{214}Po and > 98.0 % for ^{212}Po. In the NT region the efficiencies are > 96.2 % for ^{214}Po and > 99.8 % for ^{212}Po respectively. All limits are noted for 68 % C.L., see table 5.5 for a summary of the cut efficiencies.

3. The time difference cut is used to find the signature of BiPo coincidences in the single events dataset. The lowest time difference used for neutrino candidate selection is 0.5 μs [Abe14c]. Hence, this value can be assumed as safe value to reject unphysical pulses following an event, generated in the electronics or PMTs. To avoid notable losses of coincidences due the the upper time difference limit, it has to be selected several times higher than the half-life of the corresponding isotope. For ^{212}Po with a half-life of 0.299 μs an upper limit of 5 μs was chosen, which corresponds to more than 16 half-lives or a negligible loss of $9 \cdot 10^{-4}$ %. The cut efficiency due to the lower limit of 0.5 μs can be calculated as 31.4 %, that means 68.6 % of all ^{212}Po nuclei have decayed during the first 0.5 μs.

   For ^{214}Po with a half-life of 164.3 μsm the time difference window was defined from 6 μs to 2 000 μs to avoid any contamination of BiPo 212 coincidences. The time difference cut efficiency due to the lower limit can be calculated as 97.5 %. The upper limit of 2 000 μs corresponds to more than 12 half-lives of ^{214}Po and a negligible loss of 0.02 %.

   As mentioned above, the upper limits of several half-lives of each polonium isotope ensures negligible losses for long time differences. But it gives also the possibility to evaluate accidental events, which will appear as constant background in the time difference spectrum, because accidental events are not correlated in time. This will be further addressed in section 5.1.4.

4. The spatial difference cut is used to further suppress accidental background in the BiPo coincidence sample. Since the life-time of the polonium nuclei is rather short, both β^- and α events are expected to occur almost at the same position. But since the vertex reconstruction algorithm has a finite resolution, the distance between the two reconstructed vertices will be greater than zero. An upper limit in spatial difference of 50 cm was required in this analysis, which is well above the estimated vertex reconstruction resolution in the order of 20 cm [Sha14].

   To determine the spatial difference cut efficiency, a BiPo coincidence sample allowing all difference values was created. After subtracting accidental events (see section 5.1.4) the number of found BiPo coincidences was compared to the number of coincidences in the sample with < 50 cm spatial difference. The spatial difference cut efficiency for BiPo 214 coincidences was determined to be 98.6 ± 0.5 % and for BiPo 212 coincidences > 98.6 % at 68 % C.L. respectively.

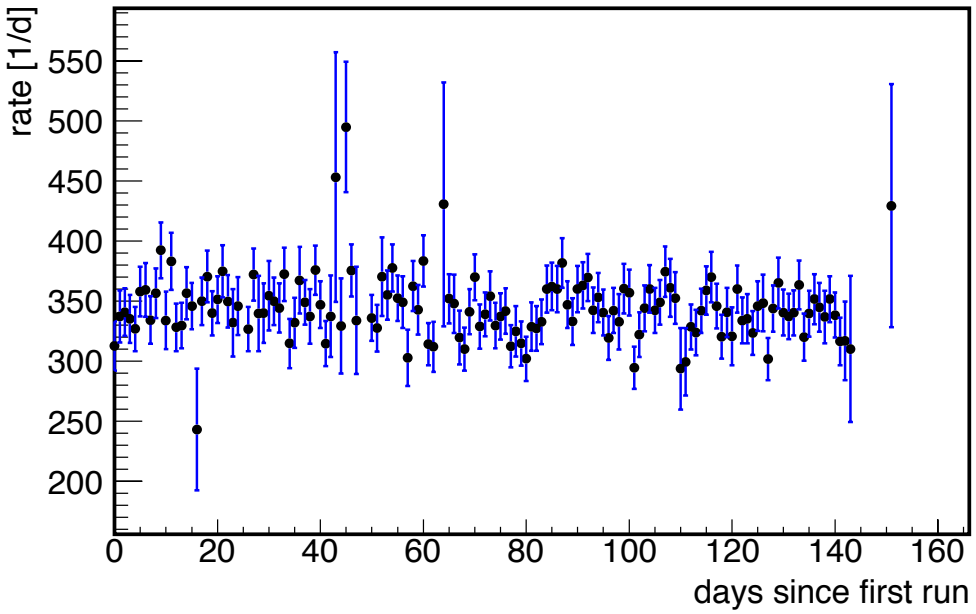

Figure 5.3: Daily rate of coincidences passing the used BiPo 214 selection cuts. First run was taken on January 26th, 2015. This rate is not the actual BiPo coincidence rate because no accidentals or efficiencies have been taken into account. This is meant to confirm a constant rate for the used dataset. The error bars depict the statistical error.

Another cut, which is normally applied to coincidence search, is a multiplicity cut. That means, no other valid trigger besides the delayed event is allowed in the whole time difference window. This cut might have had an effect during production of the single events dataset, but did not change the BiPo coincidence selection in this analysis.

5.1.3 Coincidence rate evolution

To use BiPo coincidences as a tag for radioimpurities in the Double Chooz detector, one has to assume radioactive equilibrium in the decay chains of uranium and thorium. If this assumption is true, a constant rate of BiPo coincidences is expected on time scales of the Double Chooz detector operation. If the radioactive equilibrium is broken, the BiPo coincidence rate will change in time. The change in time would have the same time structure as the decay of the isotope which has a higher concentration within the decay chain. In the case of BiPo 214 coincidences, which are following the decay of ^{222}Rn, this is interesting in terms of detector tightness and possible radon emanations.
Figure 5.3 shows the rate of BiPo 214 coincidences on a daily basis since the first run used in this analysis, taken on January 26th, 2015. It is important to note that this shows only the rate of coincidences which pass the selection cuts and not the number of decays within the uranium chain. To get this number, accidental

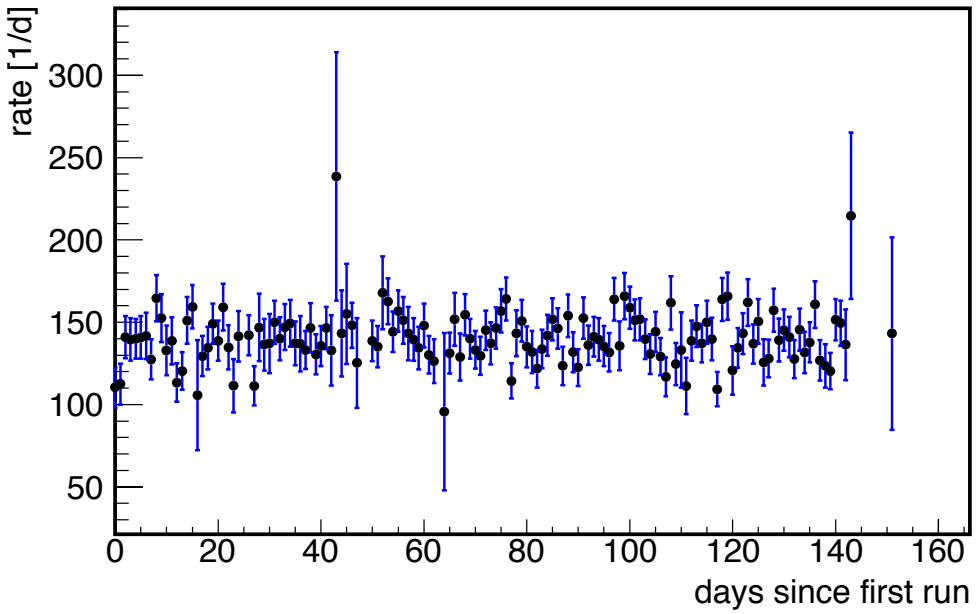

Figure 5.4: Daily rate of coincidences passing the used BiPo 212 selection cuts. First run was taken on January 26th, 2015. This rate is not the actual BiPo coincidence rate because no accidentals or efficiencies have been taken into account. This is meant to confirm a constant rate for the used dataset. The error bars depict the statistical error.

coincidences and the efficiencies of the selection cuts have to be included first. This will be shown in section 5.1.9 where the mass concentration of uranium and thorium in the Double Chooz detector will be calculated. The daily rate of found BiPo 214 coincidences is constant over time. This indicates that the liquid scintillator was not contaminated during filling and that radioactive equilibrium in the uranium decay chain, at least below ^{226}Ra, is reached.
The same is shown for BiPo 212 coincidences passing the selection cuts in figure 5.4. The daily rate stays constant over the data taking period, indicating radioactive equilibrium in the thorium decay chain.

5.1.4 Accidental BiPo coincidences

As seen in figure 5.2, the energy spectrum of single events spreads all along the prompt and delayed energy cut windows with considerable rate. Therefore, it is just a matter of probability that uncorrelated events pass the selection cuts by accident. This is called accidental background and has to be accounted for during rate calculations for example. All background in this analysis is assumed to be accidental, except BiPo 214 coincidences which can be tagged as BiPo 212 coincidences because of overlapping energy windows and a half-life fitting into the time difference window of BiPo 212.
It is not possible to discriminate accidental BiPo coincidences on an event by event

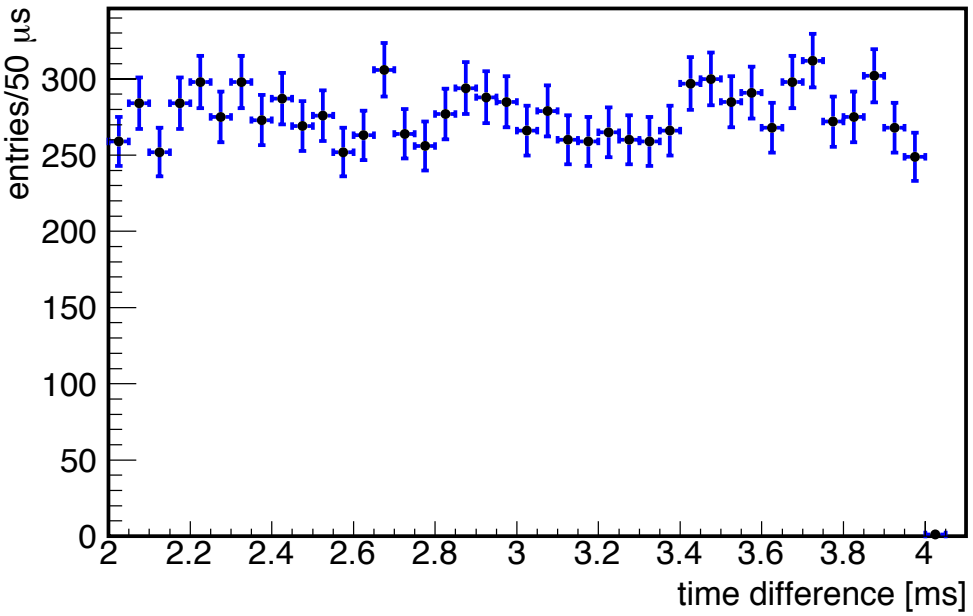

Figure 5.5: Time difference between prompt and delayed event of BiPo 214 accidental coincidences. A flat distribution is found, indicating a completely uncorrelated set of coincidences as expected for a clean accidental coincidence sample. The error bars depict the statistical error and bin width.

basis. But, the accidental background rate can be calculated analytically or it can be determined in a separate analysis. This gives not only the rate of accidental coincidences, but also allows to determine the energy spectrum of accidentals, which can be statistically subtracted from the energy spectrum of selected BiPo coincidences. One possibility is to shift the time difference window by an arbitrary amount. If the shift is big enough, all correlated coincidences will be cut out. This also applies for BiPo 214 coincidences spoiling into the BiPo 212 dataset. So, only true accidental coincidences survive the selection cuts and a clear sample of BiPo 214 and BiPo 212 like accidental coincidences can be determined.
This dedicated analysis was done by shifting the time difference window for BiPo coincidences by 2 ms leaving all other cuts untouched. This results in a time difference cut of 2 006 μs to 4 000 μs for BiPo 214 and 2 000.5 μs to 2 005 μs for BiPo 212 respectively. The energy spectrum of prompt and delayed events are not shown here, but are subtracted statistically from the visible energy spectra of bismuth and polonium to get a clean BiPo coincidence energy spectrum.
The time difference distribution of BiPo 214 accidental coincidences is shown in figure 5.5. For a completely uncorrelated sample of coincidences, any time difference between prompt and delayed event occurs with the same probability. This expected flat spectrum is found for BiPo 214 accidental coincidences, as well as for BiPo 212 accidental coincidences whose distribution is not shown here.
The surface of a sphere with radius r around a certain point is proportional to r^2.

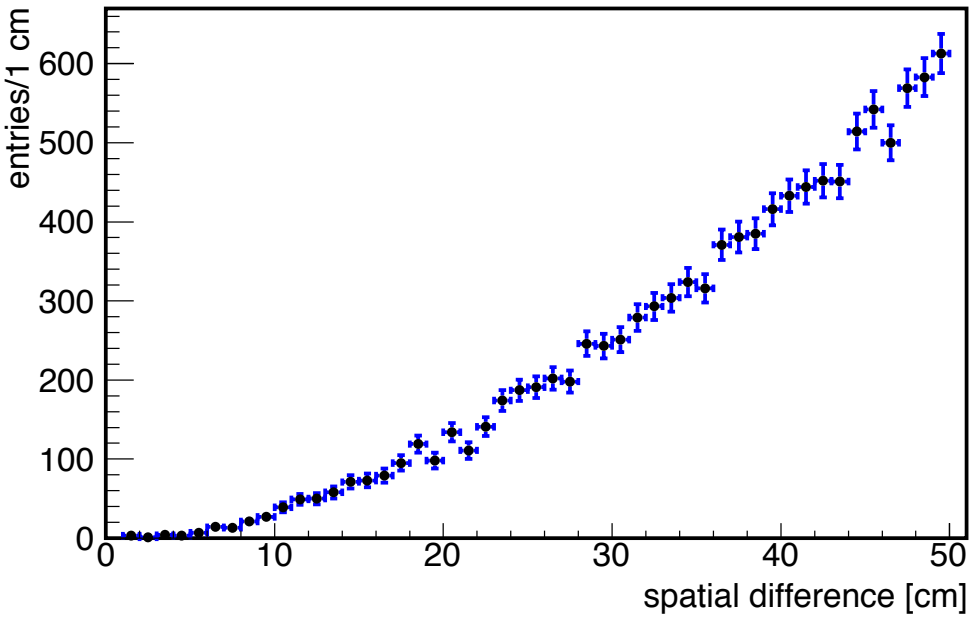

Figure 5.6: Spatial difference between prompt and delayed event of BiPo 214 accidental coincidences. A quadratically rising distribution is found, which is expected for an uncorrelated set of coincidences. The error bars depict the statistical error and bin width.

Hence, the spatial distance distribution of a completely uncorrelated sample has to rise quadratically. The distribution for BiPo 214 accidental coincidence can be found in figure 5.6, which shows this expected behavior. For the distribution of BiPo 212 accidental coincidences, which is not shown here, the statistics are to low to draw any conclusions.

A projection of the reconstructed vertices of prompt and delayed events of BiPo 214 accidental coincidences is shown in figure 5.7. In a projection like this, correcting for geometrical effects, a homogeneous distribution of radioimpurities would cause an even vertex map within the detector. This is true for large parts of the detector but also two accumulations of accidental events are found along the central axis of the detector. The more dominant excess can be seen right below the chimney of the detector. Because of this feedthrough, the shielding on top of the detector has a small hole around the chimney region. External radiation can enter the detector there, causing an accumulation of accidental events. As already explained in section 4.1.1, a HPS was glued to the bottom of the GC vessel. This sensor introduces a small amount of radioactivity, causing a higher fraction of accidental events at its position.

Another access to the BiPo accidental coincidence rate is a fit to the time difference distribution of the coincidences passing the selection cuts. The accidental rate determined by this method is explained in section 5.1.6. A summary of the number of accidental coincidences determined by this method and by the dedicated accidentals analysis, compared to the number of found BiPo coincidences, is shown in table 5.2.

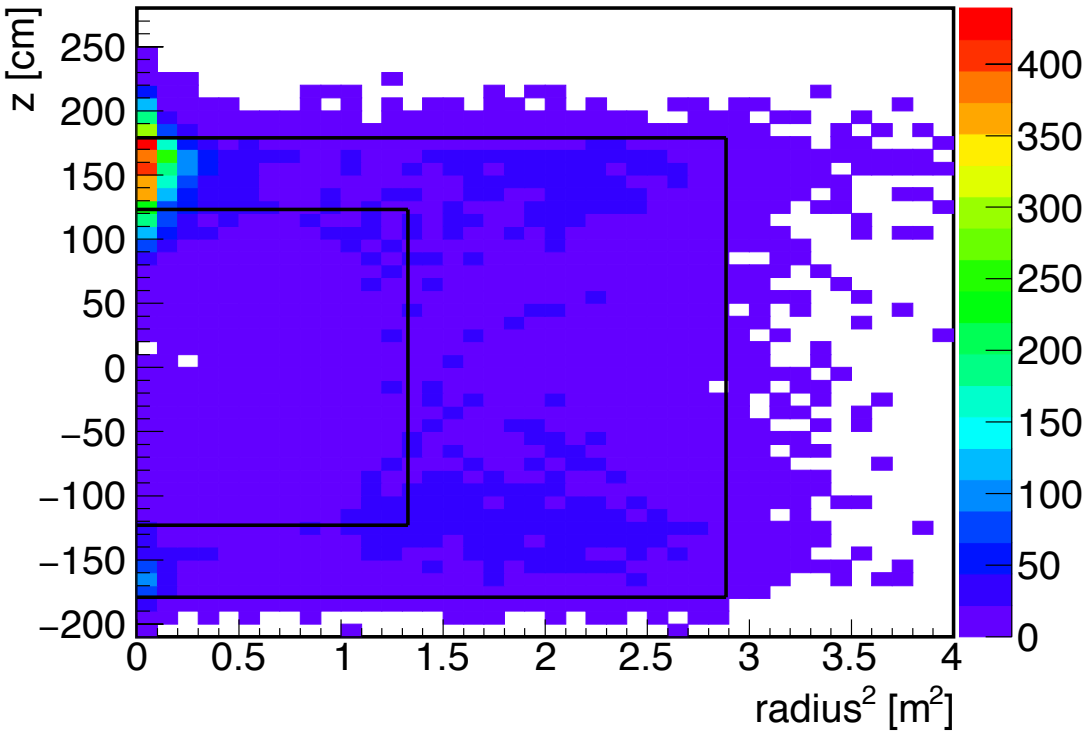

Figure 5.7: Reconstructed vertices of prompt and delayed events of the BiPo 214 accidental coincidence sample. The x-axis shows the squared radius of the events, that means in terms of the coordinates $x^2 + y^2$, to correct for any geometrical effects in the plot. The y-axis represents the z coordinate and the color depicts the number of events in a bin of the projection. The black lines show the dimensions of NT and GC vessels respectively. A clear excess of events is found around $(0, 160)$ which is right below the chimney of the detector. Because of the feedthrough there is a hole in the shielding which allows external radiation to enter the detector and causing a higher rate of accidentals in this region. Another much smaller excess is visible around $(0, -165)$ which could arise from the GC HPS which is glued to the bottom of the GC vessel.

	BiPo 214	BiPo 212
selected coincidences	$37\,914 \pm 195$	$15\,483 \pm 124$
accidentals analysis	$11\,072 \pm 105$	54 ± 7
fit to time difference spectrum	$10\,838 \pm 159$	< 571

Table 5.2: Number of accidental BiPo coincidences compared to the number of coincidences passing the selection cuts. The number from the accidental analysis comes from a clean sample of accidental coincidences selected by shifting the time difference window. In section 5.1.6 the calculation from a fit to the time difference distribution will be explained.

5.1.5 Prompt and delayed event energy spectrum

After gathering all events which pass the selection cuts and after determination of the accidental event energy spectrum, these two datasets can be combined. By subtracting analytically the accidental energy spectrum from the selected coincidence energy spectrum, a clean energy spectrum of BiPo coincidences can be obtained. This was done for both prompt and delayed energy event spectrum.
The corrected prompt event energy spectrum of BiPo 214 coincidences can be found in figure 5.8, the corresponding one for BiPo 212 coincidences is shown in figure 5.9. For the β^--decay of ^{214}Bi and ^{212}Bi, several excited states of the polonium daughter nuclei can be reached. The continuous energy spectrum is therefore a combination of the emitted electron from the β-decay and of one or more gammas coming from disexcitation of the polonium daughter nuclei.
Due to the different α quenching factors for GC and NT liquid scintillator it is necessary to plot the delayed energy spectrum separately for each volume. Since a fit to this data can be used to measure the quenching factors for GC and NT, this will be further addressed in section 5.1.8. The delayed energy spectra for BiPo 214 events are shown in figure 5.18 and figure 5.19. For BiPo 212 events the delayed energy spectra are shown in figure 5.20 and figure 5.21 accordingly.

5.1.6 Half-life of polonium

A key value to extract BiPo coincidences from the single events dataset, is the time difference between prompt and delayed event. The time difference distribution for BiPo 214 coincidences is shown in figure 5.10 and for BiPo 212 coincidences in figure 5.11 respectively. To measure the half-life of the polonium nuclei, which is responsible for the delayed coincidence signal, a constant background function summated with an exponential decay function was fitted to the data:

$$y(t) = e^{c - t\frac{\ln 2}{T_{1/2}}} + b \tag{5.1}$$

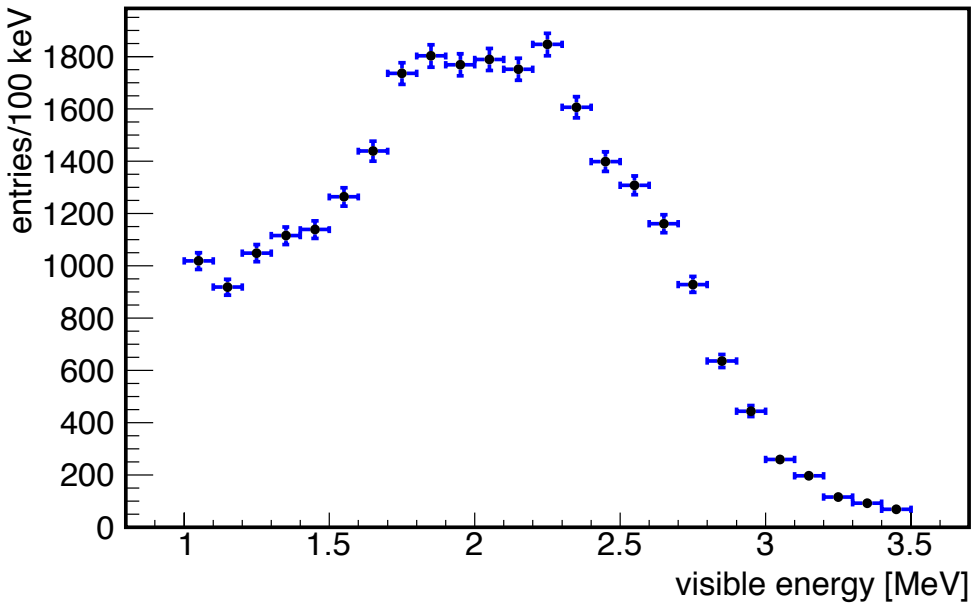

Figure 5.8: BiPo 214 prompt event energy spectrum. The energy spectrum of accidental events was subtracted analytically. The continuous energy distribution is caused by the β^- spectrum of ^{214}Bi with a Q-value of 3.272 MeV [Fir96]. Error bars depict the statistical error and bin width.

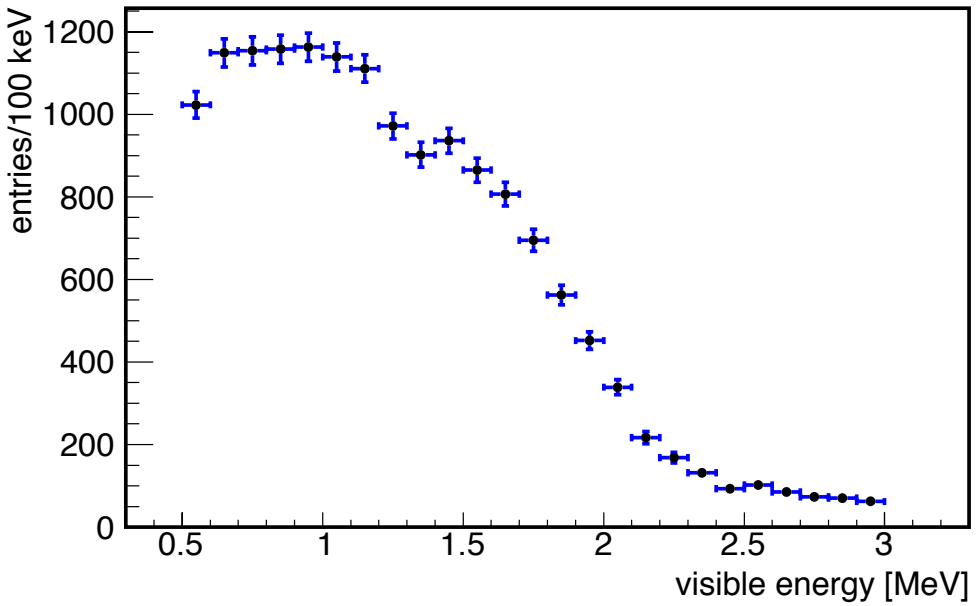

Figure 5.9: BiPo 212 prompt event energy spectrum. The energy spectrum of accidental events was subtracted analytically. The continuous energy distribution is caused by the β^- spectrum of ^{212}Bi with a Q-value of 2.254 MeV [Fir96]. Error bars depict the statistical error and bin width.

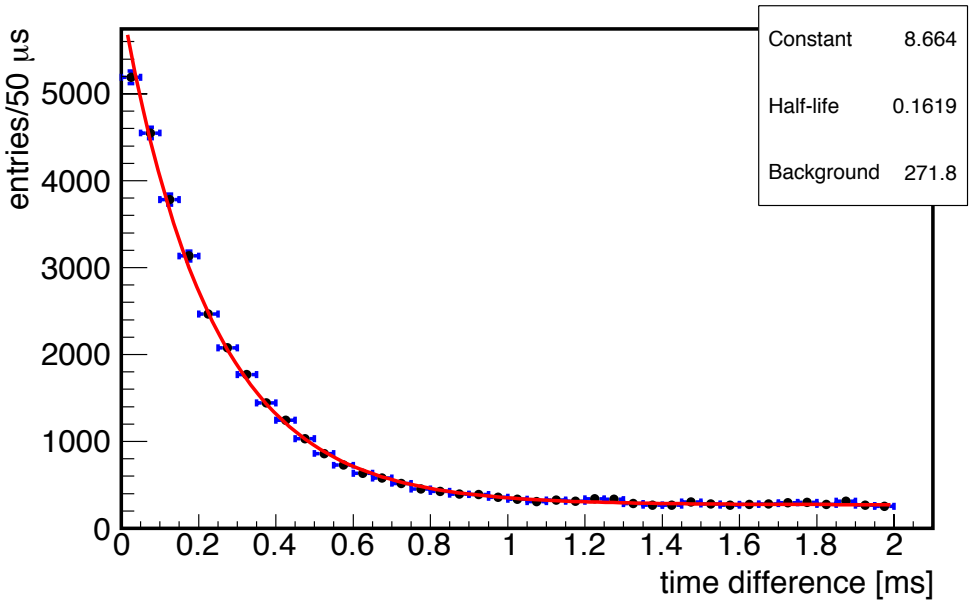

Figure 5.10: Time difference between prompt and delayed event of BiPo 214 coincidences. A constant background function plus an exponential decay has been fitted to the data. The fitted half-life of ^{214}Po is $161.9 \pm 1.6\,\mu$s and the error bars depict the statistical error and bin width.

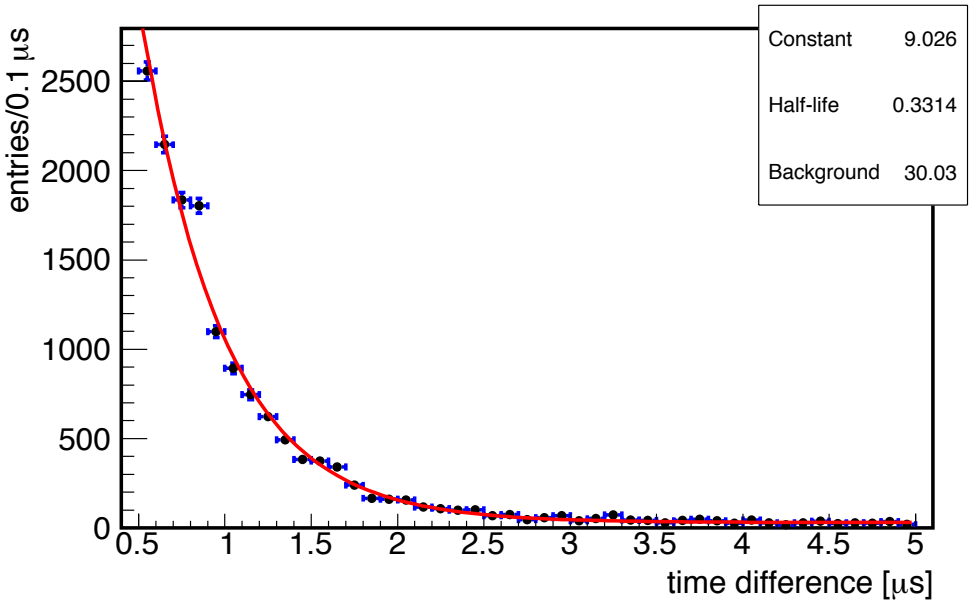

Figure 5.11: Time difference between prompt and delayed event of BiPo 212 coincidences. A constant background function plus an exponential decay has been fitted to the data. The fitted half-life of ^{212}Po is $0.331 \pm 0.004\,\mu$s but this value could be affected by an inefficiency for short time differences. Error bars depict the statistical error and bin width.

Here y is the number of coincidences as a function of the time difference t. e^c corresponds to the number of coincidences at $t = 0$ and b is to account for a constant background contribution. Choosing the fit function in this form, provides the half-life directly in the form of the parameter $T_{1/2}$.
The fitted half-life of ^{214}Po is $161.9 \pm 1.6\,\mu$s, which agrees well with the literature value of $164.3 \pm 2.0\,\mu$s [Fir96]. A deviation in the order of 10 % is found between the fitted half-life of ^{212}Po with $0.331 \pm 0.004\,\mu$s and the literature value of $0.299 \pm 0.002\,\mu$s [Fir96]. There seems to be an inefficiency for short time differences and the data point around $0.85\,\mu$s is much higher than expected. Both effects are not understood yet, but lead to a higher fitted half-life.
As mentioned before, the constant part of the fit function provides the number of accidental background events per bin. From this number the total amount of accidental coincidences in the dataset can be calculated. In the case of BiPo 214 coincidences this method gives a reliable determination of the number of accidental coincidences. The number of BiPo 214 accidental coincidences was determined to be $10\,838 \pm 159$ in good agreement to the value from the dedicated accidental analysis of $11\,072 \pm 105$.
In the case of BiPo 212 coincidences the fit delivers a total number of 1351 ± 58 accidental coincidences. But this time BiPo 214 coincidences leaking into the BiPo 212 data sample due to the overlapping energy window have to be considered. Because of the large time scale compared to BiPo 212 coincidences, they will contribute to the constant background of the BiPo 212 fit function. If all cut efficiencies are ignored, the number of spoiled BiPo 214 events can be estimated from the number of selected BiPo 214 coincidences by just using the time difference distribution of both BiPo coincidences. This gives a rough estimation of > 838 BiPo 214 events in the BiPo 212 coincidence dataset. The rough estimation on BiPo 212 only accidental coincidences can be estimated as < 571 in the used dataset. This is by a factor of 10 times higher than the determined value of 54 ± 7 using the dedicated accidental analysis. This method has a much higher uncertainty due to all cut efficiencies, which would have to be accounted for. In contrast to the dedicated accidental analysis, which provides a clean set of accidental coincidences. Hence, these results from the time difference fit are not used for any calculations, only as a comparison.

5.1.7 Coincidence position reconstruction

Because of the rather short life-time of the polonium nuclei, both β^- and α event vertices are expected to occur almost in the same position. Nevertheless, the vertex reconstruction algorithm has a finite resolution in the order of 20 cm [Sha14]. This affects the measured distribution of spatial difference between the reconstructed prompt and delayed event vertices. The spatial difference distribution for BiPo 214 and BiPo 212 coincidences is shown in figure 5.12 and figure 5.13 respectively. The data points with round markers and blue error bars show the measured distribution. To correct for the quadratically rising surface of the sphere around the prompt event, the data points have been divided by d^2, where d is the spatial difference

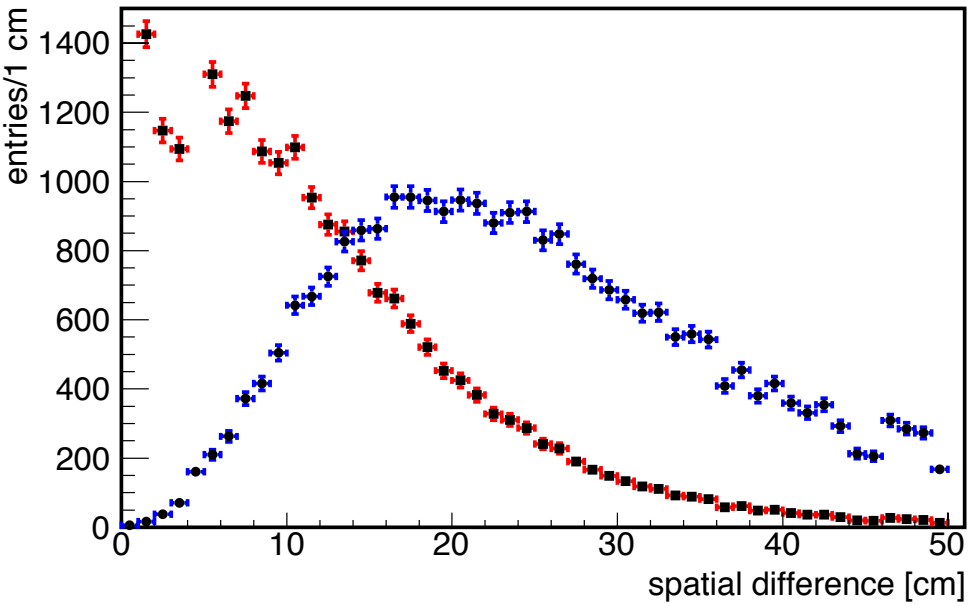

Figure 5.12: Spatial difference between prompt and delayed reconstructed vertex of BiPo 214 coincidence. Circles and blue error bars show the measured distribution, squares with red error bars show a geometrically corrected distribution proving spatial correlation of the coincidences. The error bars depict the statistical error and bin width.

corresponding to each bin center. Data points with squared markers and red error bars show this corrected and renormalized distribution. Thus, in both distributions the same number of entries is shown. For a completely uncorrelated sample the corrected distribution would show a flat spectrum. A clear spatial correlation between prompt and delayed event is found in figure 5.12 for BiPo 214 coincidences and in figure 5.13 for BiPo 212 coincidences accordingly.

The reconstructed vertices of the prompt and delayed events of the BiPo 214 coincidences are shown in figure 5.14, using a side view projection. Since the surface of a cylinder around the central axis of the detector scales with radius r, a side view projection would accumulate events for larger r, masking a homogenous distribution in the detector. Therefore the plot shows the squared radius $r^2 = x^2 + y^2$ on the x-axis to correct for this geometrical effect. Figure 5.14 shows an almost homogenous vertex distribution besides a higher fraction of events at the bottom of the GC vessel. This could arise from the NT acrylic vessel support structure, which may introduce some intrinsic radioimpurities. A more clear excess of events appears around $(0, -140)$. As already explained in section 4.1.1, a HPS was glued to the bottom of the GC vessel. This sensor introduces a small amount of radioactive impurities causing a higher fraction of events in this region. The more dominant excess can be seen right below the chimney of the detector around $(0, 160)$. Because of the chimney feedthrough, the shielding on top of the detector has a small hole around this region. External radiation can enter the detector causing an accumulation of

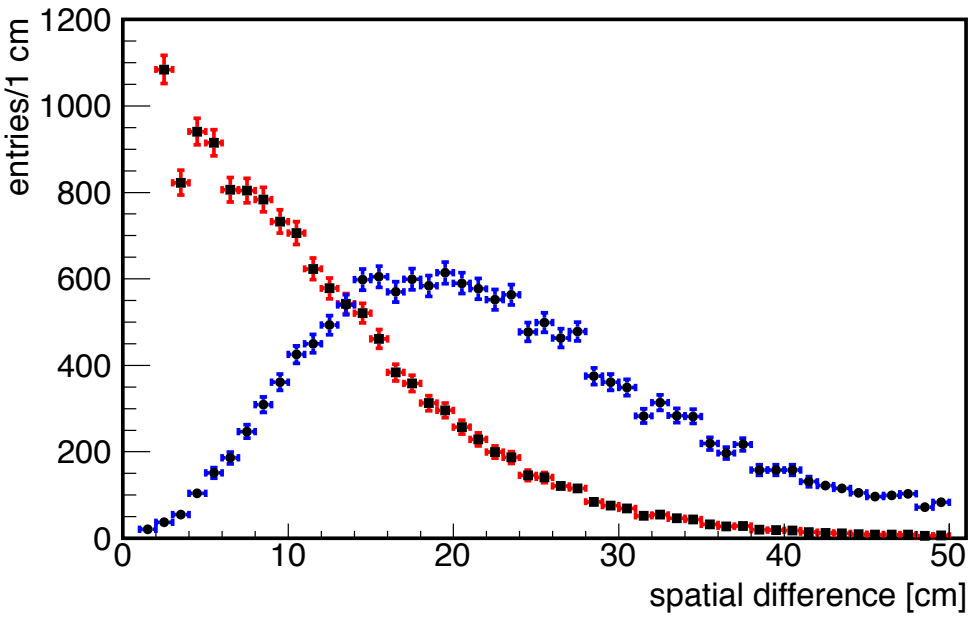

Figure 5.13: Spatial difference between prompt and delayed reconstructed vertex of BiPo 212 coincidence. Circles and blue error bars show the measured distribution, squares with red error bars show a geometrically corrected distribution proving spatial correlation of the coincidences. The error bars depict the statistical error and bin width.

events below this hole.
A top view projection of BiPo 214 coincidences is shown in figure 5.15. Besides the excess in the middle, coming from the area below the chimney, there is also the event structure from the GC vessel bottom. The acrylics support structure for the NT vessel has six feet. These are aligned symmetrically with two feet orientated along the y-axis of figure 5.15. This 6-fold structure can be adumbrated in the top view projection and could explain the structure of events at the GC bottom. This also indicates that the number of BiPo 214 coincidences is enhanced through uranium contamination in the acrylics or the glue used for construction.
The side view projection for BiPo 212 coincidences is shown in figure 5.16. Again, the squared radius on the x-axis is used to correct for the geometrical bias. It becomes apparent that the NT liquid scintillator has a much higher fraction of radioimpurities coming from the thorium decay chain than the GC liquid scintillator. The majority of all BiPo 212 coincidences appear inside the NT vessel. Again, there is an excess of events in the region below the chimney as already seen for BiPo 214 coincidences. Besides this feature, a homogenous distribution within the NT vessel is found. Therefore it can be concluded, that the thorium contamination is dominated by the NT liquid scintillator and not by the acrylics or glue as for the BiPo 214 coincidences.
Figure 5.17 shows the top view projection for the BiPo 212 coincidence events vertex reconstruction. The accumulation in the middle is caused by the chimney, as

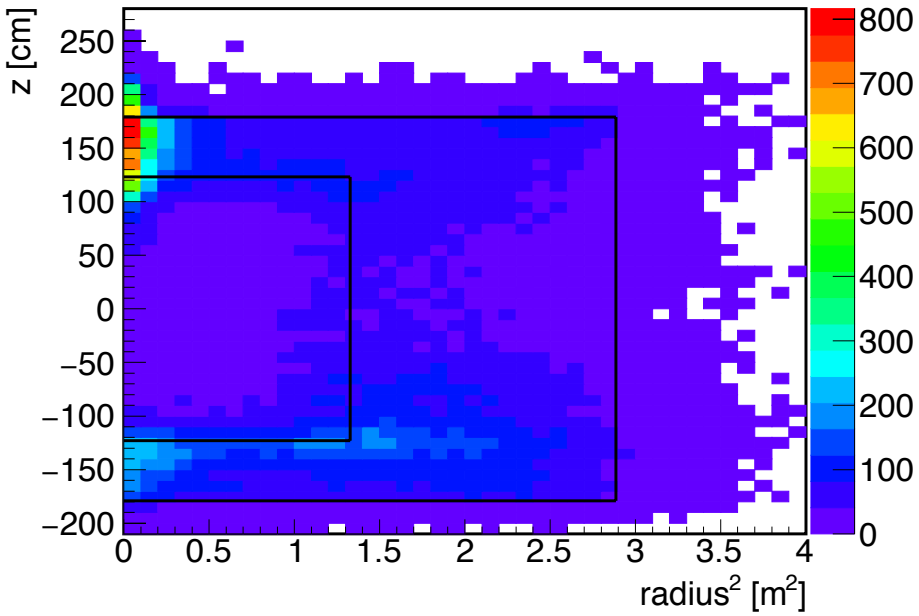

Figure 5.14: Vertex reconstruction of BiPo 214 coincidences in side view projection. The x-axis shows the squared radius $x^2 + y^2$ to correct for geometrical effects. The y-axis shows the z coordinate and the color depicts the number of events in a projection bin. The black lines show the dimensions of NT and GC vessels respectively. A detailed discussion of the features can be found in the text.

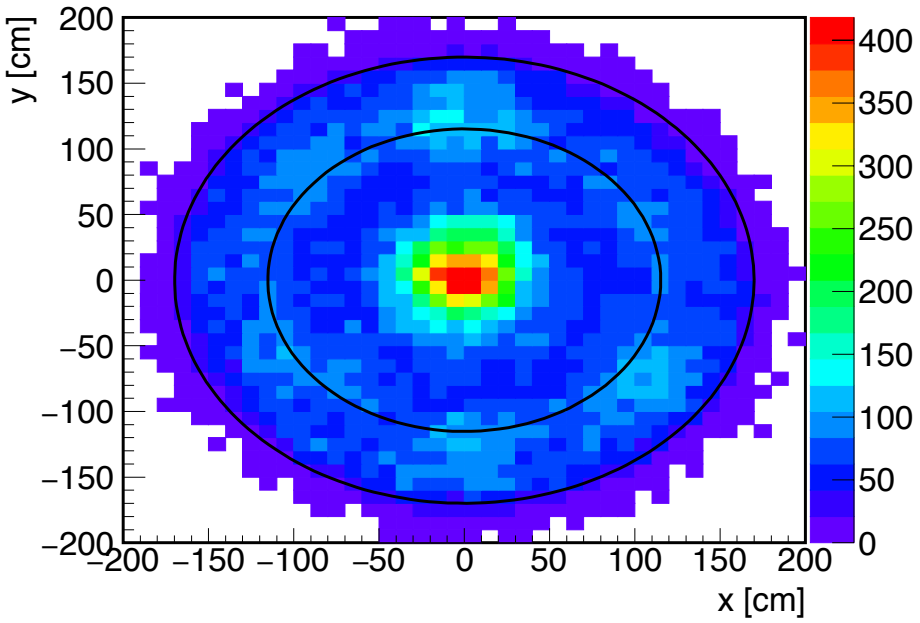

Figure 5.15: Vertex reconstruction of BiPo 214 coincidences in top view projection. The x and y coordinates are plotted, while the z coordinate is projected to the x-y-plane. The color depicts the number of events in a projection bin. The black lines show the dimensions of NT and GC vessels respectively. A discussion of the features can be found in the text.

mentioned before. Furthermore, the homogenous distribution within the NT vessel and the absence of notable events in the GC liquid scintillator, as already seen in the side view projection, are confirmed.

5.1.8 α quenching factors

After showing the visible prompt energy spectra for BiPo coincidences in section 5.1.5, the delayed event energy spectra are shown here. In contrast to the continuous β^- energy spectrum of bismuth, a monoenergetic line originating from the α decay of polonium is expected. However, due to the finite detector energy resolution a gaussian shaped peak will be present in the delayed energy spectrum.
Due to the different α quenching factors for GC and NT liquid scintillator, it is necessary to plot the delayed energy spectrum separately for each volume. To clearly separate the two volumes, all coincidences with a reconstructed vertex closer than 25 cm to the NT vessel wall were discarded. Compared to the vertex reconstruction resolution in the order of 20 cm [Sha14], this should provide a clear separation of GC and NT events. The delayed event energy spectra for BiPo 214 coincidence events are shown in figure 5.18 and figure 5.19. For BiPo 212 coincidence events the delayed energy spectra are shown in figure 5.20 and figure 5.21 accordingly.
A gaussian function was fitted to the data of all four delayed energy spectra:

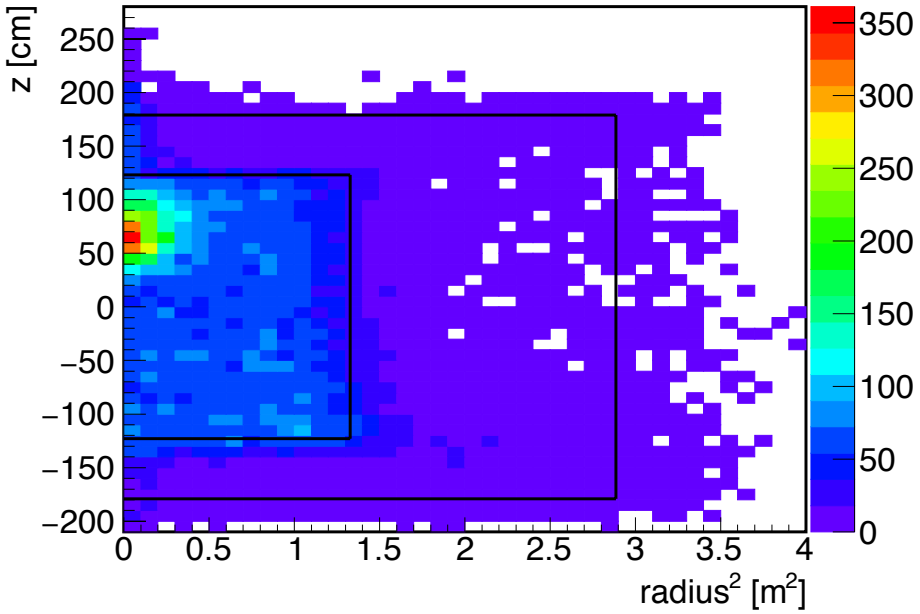

Figure 5.16: Vertex reconstruction of BiPo 212 coincidences in side view projection. The x-axis shows the squared radius $x^2 + y^2$ to correct for geometrical effects. The y-axis shows the z coordinate and the color depicts the number of events in a projection bin. The black lines show the dimensions of NT and GC vessels respectively. A detailed discussion of the features can be found in the text.

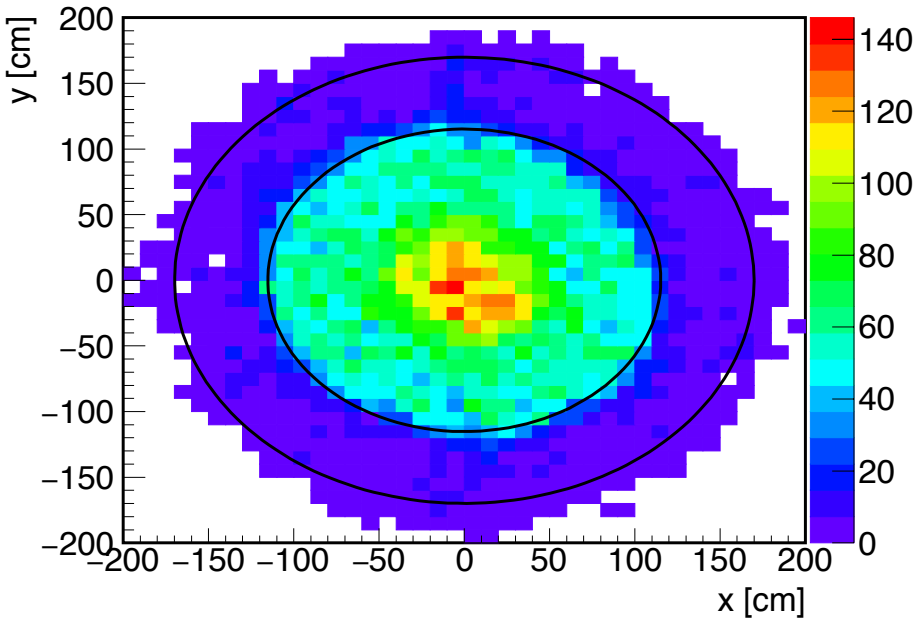

Figure 5.17: Vertex reconstruction of BiPo 212 coincidences in top view projection. The x and y coordinates are plotted, while the z coordinate is projected to the x-y-plane. The color depicts the number of events in a projection bin. The black lines show the dimensions of NT and GC vessels respectively. A discussion of the features can be found in the text.

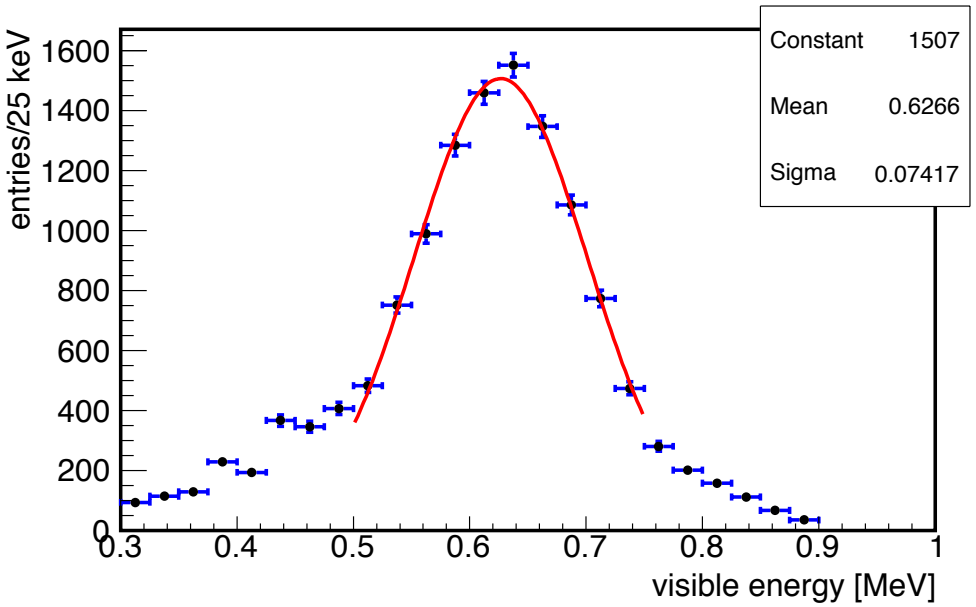

Figure 5.18: BiPo 214 delayed event energy spectrum for GC. A gaussian function was fitted to the α peak. The mean value of the fit is $626.6 \pm 0.9\,\mathrm{keV}$ with an energy resolution estimation of $11.8 \pm 0.2\,\%$ for this energy. The error bars depict the statistical error and bin width.

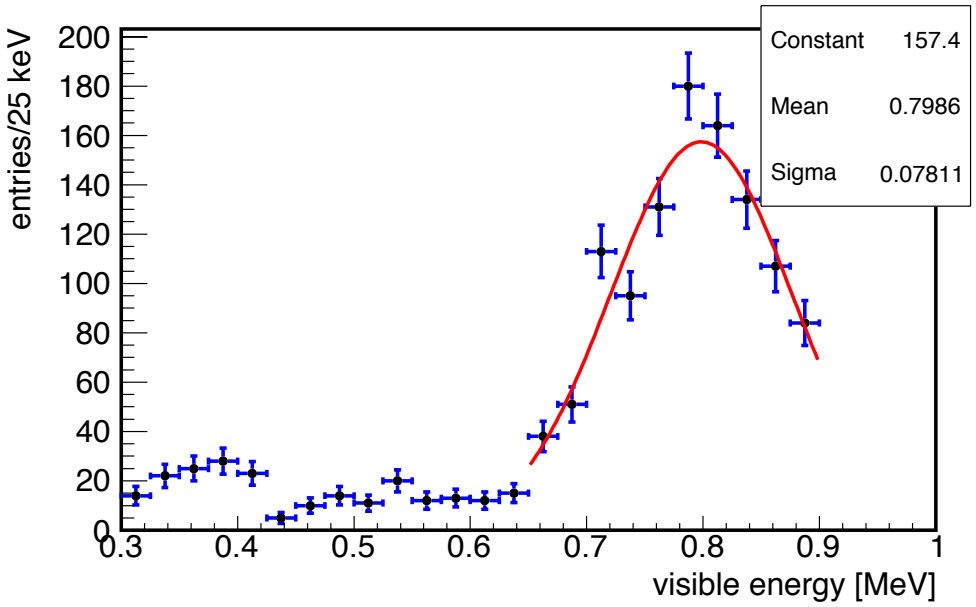

Figure 5.19: BiPo 214 delayed event energy spectrum for NT. A gaussian function was fitted to the α peak. The mean value of the fit is $798.6 \pm 3.4\,\mathrm{keV}$ with an energy resolution estimation of $9.8 \pm 0.5\,\%$ for this energy. The error bars depict the statistical error and bin width.

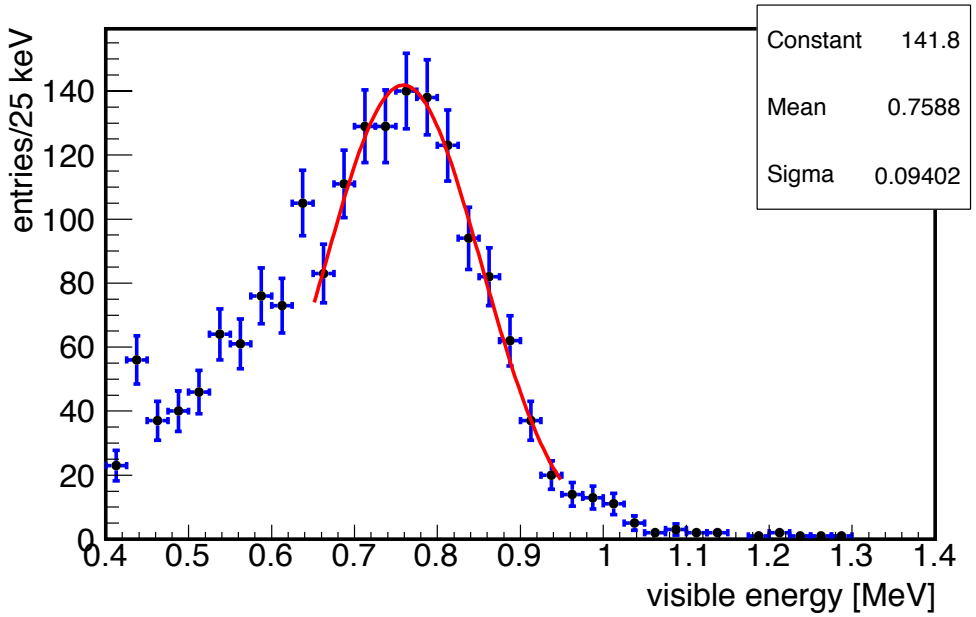

Figure 5.20: BiPo 212 delayed event energy spectrum for GC. A gaussian function was fitted to the α peak. The mean value of the fit is $758.8 \pm 4.5\,\mathrm{keV}$ with an energy resolution estimation of $12.4 \pm 0.6\,\%$ for this energy. The error bars depict the statistical error and bin width.

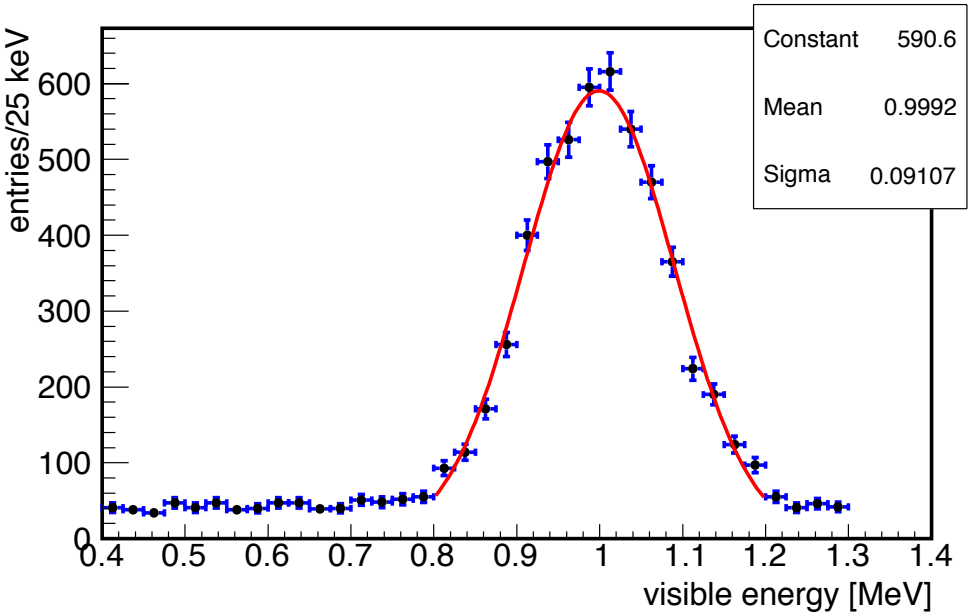

Figure 5.21: BiPo 212 delayed event energy spectrum for NT. A gaussian function was fitted to the α peak. The mean value of the fit is 999.2 ± 1.4 keV with an energy resolution estimation of 9.1 ± 0.1 % for this energy. The error bars depict the statistical error and bin width.

	GC scintillator	NT scintillator
BiPo 214	11.8 ± 0.2 %	9.8 ± 0.5 %
BiPo 212	12.4 ± 0.6 %	9.1 ± 0.1 %

Table 5.3: Values for an estimated detector energy resolution determined by fitting gaussian functions to the delayed energy spectrum of BiPo coincidences.

$$y(E) = c \cdot e^{-0.5\left(\frac{E-\mu}{\sigma}\right)^2} \tag{5.2}$$

Here y is the number of coincidences as a function of the visible energy E. c corresponds to maximum of the gaussian peak at $E = \mu$, σ can be used as resolution of the peak and μ is the mean value of the peak. Values for an estimated detector energy resolution determined with the fits to the delayed energy spectrum are summarized in table 5.3. The values for GC and NT liquid scintillator are in good agreement for both determination cases. In general it was found that the detector features a better energy resolution for NT events compared to GC events. This reflects the effort which was taken to get a high energy resolution in the NT fiducial volume.
Another key value which is accessible through this fit is the α quenching factor for

	GC scintillator	NT scintillator
BiPo 214 (7.687 MeV)	12.27 ± 0.02	9.63 ± 0.04
laboratory measurement	12.6 ± 0.6	9.8 ± 0.4
BiPo 212 (8.784 MeV)	11.57 ± 0.07	8.79 ± 0.01

Table 5.4: α quenching factors determined by fitting gaussian functions to the delayed energy spectrum of BiPo coincidences. The quenching factor for BiPo 214 at an energy of 7.687 MeV was compared to a laboratory measurement [Abe11] and shows good agreement.

the Double Chooz liquid scintillators. The literature value for the energy of the polonium α decay is divided by the mean value of the gaussian fit. The results are summarized in table 5.4. There is a laboratory measurement of the α quenching factors performed at an energy of 7.687 MeV [Abe11]. The values for BiPo 214 coincidences at the same energy found in this analysis are in good agreement with the values from the laboratory measurement. For an energy of 8.784 MeV from the BiPo 212 coincidences no values for comparison are available.

5.1.9 Concentration of radioimpurities

The goal of the BiPo coincidence analysis which was presented here, is to measure the mass concentration of uranium and thorium in the Double Chooz detector. Under the assumption of radioactive equilibrium, the number of decays coming from the uranium and thorium decay chain can be calculated from the number of BiPo coincidences. To calculate the number of BiPo coincidences the number of accidental coincidences N_{acc} determined in section 5.1.4 was subtracted from the number of all coincidences N which passed the selection cuts. To calculate the mass concentration c of uranium and thorium the following formula was used:

$$c = \frac{1}{\prod_{\epsilon}}(N - N_{\mathrm{acc}})\frac{m}{M}\frac{\tau}{t} \tag{5.3}$$

Here m is the atomic mass of ^{238}U or ^{232}Th, M the total mass of the fiducial volume, τ the life time of ^{238}U or ^{232}Th and t the live time of the used dataset. To account for all efficiencies summarized in table 5.5, the parameter

$$\prod_{\epsilon} = \epsilon_{\beta} \cdot \epsilon_{E_{\mathrm{p}}} \cdot \epsilon_{E_{\mathrm{d}}} \cdot \epsilon_{\mathrm{t}} \cdot \epsilon_{\mathrm{x}} \tag{5.4}$$

was used. ϵ_{β} is the β^{-} decay branching ratio of bismuth, $\epsilon_{E_{\mathrm{p}}}$ and $\epsilon_{E_{\mathrm{d}}}$ are the cut efficiencies for prompt and delayed energy respectively, ϵ_{t} the efficiency of the time difference cut and ϵ_{x} the efficiency of the spatial difference cut.

	BiPo 214	BiPo 212
bismuth β^- branching ratio	100 %	64.1 ± 0.1 %
prompt energy (Q_β of bismuth)	84.3 ± 1.3 %	74.1 ± 1.5 %
delayed energy (Q_α of polonium)	100 % (GC) > 96.2 % (NT)	> 98.0 % (GC) > 99.8 % (NT)
time difference	97.5 %	31.4 %
spatial difference	98.6 ± 0.5 %	> 98.6 %

Table 5.5: Efficiencies of selection cuts for BiPo coincidences to extract BiPo 214 and BiPo 212 events from the used single events dataset. The branching ratio data was taken from [Fir96]. The efficiencies for prompt end delayed energy cuts were taken from [Hof12]. The time difference cut efficiency is analytically calculated and the spatial difference cut efficiency is determined in a dedicated study.

The mass concentration of uranium in the inner part of the Double Chooz near detector, calculated using the whole dataset, is $(1.09 \pm 0.03) \cdot 10^{-14}$ g/g. The mass concentration of thorium is $(9.76 \pm 0.27) \cdot 10^{-14}$ g/g accordingly. Compared to the design goal of 10^{-13} g/g [Ard06] for uranium and thorium separately in the liquid scintillator this already shows the high level of radiopurity in the Double Chooz near detector. However, the vertex reconstruction for BiPo 214 and BiPo 212 coincidences showed unequal uranium and thorium distribution in the GC and NT volumes. A possible explanation could be the different composition of the two liquids. Therefore the mass concentration was calculated for each volume separately, too. The results are shown in table 5.6. The mass concentrations are well below the design goal of 10^{-13} g/g, except for the mass concentration of thorium in the NT. The design goal was defined for the liquid scintillator itself, while the dataset used for calculation is polluted with events coming from external radiation because of the chimney (see figure 5.16). Since the total mass concentration of radioimpurities is well below the design goal of $2 \cdot 10^{-13}$ g/g for the liquid scintillators of the detector combined, the Double Chooz near detector is proven to have a high level of radiopurity.

5.2 Polonium 210 background

Another contribution to the background rate in the Double Chooz detector are (α,n) reactions. This type of this background contributes to the so called correlated background and is induced by radioactivity in the detector. Most dominant is the reaction ^{13}C(α,n)^{16}O which cannot be distinguished from an IBD event. The α decay will mimic the prompt event of the coincidence and the produced neutron will

	uranium	thorium
whole dataset	1.09 ± 0.03	9.76 ± 0.27
GC sample	1.19 ± 0.02	2.77 ± 0.04
NT sample	0.36 ± 0.01	27.3 ± 0.7

Table 5.6: Mass concentration of uranium and thorium in units of 10^{-14} g/g, calculated from the whole BiPo coincidence data sample and separately for the GC and NT sample.

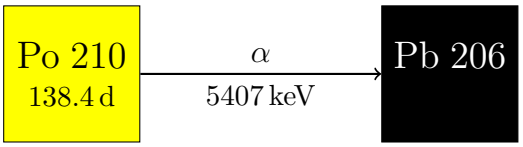

Figure 5.22: Decay scheme of ^{210}Po. No coincidence can be used to tag ^{210}Po decays in the dataset. The α energy of 5.4 MeV will be quenched to the region of fading trigger efficiency (see figure 5.24). Data taken from [Fir96].

be captured as delayed event exactly like for an IBD coincidence. According to the reactor neutrino experiment KamLAND, the (α,n) background events are coming mainly from ^{210}Po [Abe08]. This α emitter with a life time of 138.4 d is a daughter isotope of ^{210}Bi and is the last unstable isotope in the uranium decay chain. The Q-value for the α-decay is 5.407 MeV and the daughter isotope is the stable nucleus ^{206}Pb. The decay of ^{210}Po is illustrated in figure 5.22.
Since ^{210}Po is a part of the uranium decay chain, the values determined in the BiPo coincidence analysis can be used to estimate the ^{13}C(α,n)^{16}O background contribution. Under the assumption that the Double Chooz scintillator is similar to the one used in KamLAND, the ^{13}C(α,n)^{16}O rate R can be calculated from the mass concentration of uranium in the detector:

$$R = c \cdot \frac{M}{m} \frac{1}{\tau} \frac{N}{N_\alpha} \tag{5.5}$$

Here c is the mass concentration of ^{238}U in the fiducial volume with a total mass M. Moreover, m is the atomic mass and τ the life time of ^{238}U. $N = 182.0 \pm 21.7$ the number of (α,n) reactions and $N_\alpha = (5.56 \pm 0.22) \cdot 10^9$ the number of ^{210}Po decays in the KamLAND dataset [Abe08] were used as an estimate for the relation between ^{210}Po decays and ^{13}C(α,n)^{16}O events. The results for the near detector GC and NT volume are summarized in table 5.7.
All other contributions to the correlated background are much higher ($> 10^{-2}\,\mathrm{d}^{-1}$ [Abe14c]). Hence, the (α,n) background can be neglected in the case of Double Chooz. However, the mass concentrations used for the calculation of the estimation

	(α,n) reaction rate
GC	$(7.47 \pm 0.95) \cdot 10^{-6}$ d^{-1}
NT	$(1.05 \pm 0.13) \cdot 10^{-6}$ d^{-1}

Table 5.7: Calculated rate of ^{13}C(α,n)^{16}O reactions induced by ^{210}Po decays under the assumption of radioactive equilibrium in the uranium decay chain. For calculation, the mass concentrations from table 5.6 and the ratio between (α,n) reactions and ^{210}Po decays from KamLAND [Abe08] were used.

are only valid under the assumption of radioactive equilibrium in the uranium decay chain. ^{210}Pb, a member of the uranium decay chain, has a relatively high life time of 22.3 years, which could break the radioactive equilibrium at this point. A dedicated study searching directly for the ^{210}Po decays could investigate if the decay chain is broken or not. For this thesis it was not possible to do this analysis with Double Chooz near detector data. Therefore, a far detector dataset from a study, which was already done in 2014, will be used to demonstrate the ^{210}Po analysis principle. A single events dataset containing 465.5 days of live time from the far detector was used. As an example the events in the NT are used for demonstration.
The single event spectrum for this far detector dataset is shown in figure 5.23. The trigger efficiency for single events in the far detector is practically 100 % down to energies of 0.4 MeV. For lower energies the trigger efficiency starts to drop quickly (see figure 5.24). The α quenching factor for an energy equal to the Q-value of the ^{210}Po decay was measured to be 17.4 ± 0.5 in the GC liquid scintillator and 13.1 ± 0.2 in the NT liquid scintillator [Abe11]. Accordingly, the α events coming from ^{210}Po are expected at an energy of 311 keV in the case of the GC and at an energy of 413 keV in the case of the NT. Hence, the α events will be suppressed because of an inefficiency caused by the trigger efficiency at these energies. The measured energy spectrum is a convolution of the true energy spectrum and the trigger efficiency. To correct for this suppression effect, the single event spectrum was divided by the corresponding trigger efficiency for each bin center. The result after this correction is shown in figure 5.25 for the case of NT events.
The corrected single event energy spectrum shows a clear peak, which is most likely coming from α events. To evaluate the excess, a gaussian fit function summated with an exponential background function was fitted to the spectrum:

$$y(E) = e^{a+bE} + c \cdot e^{-0.5\left(\frac{E-\mu}{\sigma}\right)^2} \tag{5.6}$$

Here y is the number of events as a function of the visible energy E. The important parameter is μ, the mean value of the gaussian peak. For the NT energy spectrum shown in figure 5.25, the mean value μ was found to be 453.9 ± 1.2 keV which was translated into an α quenching factor of 11.9 ± 1.6. The mean value is

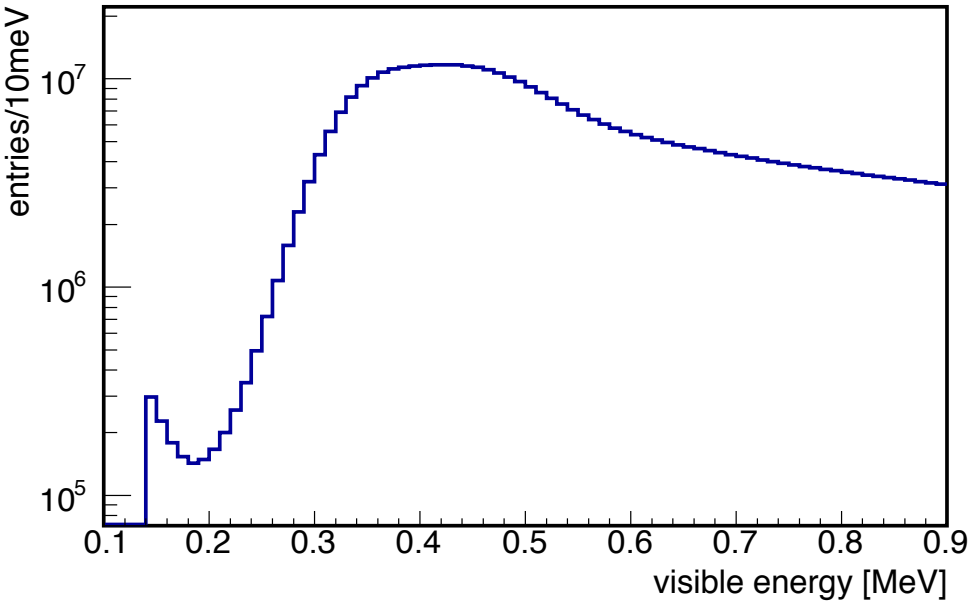

Figure 5.23: Far detector single event energy spectrum from a dataset with 466 days of live time. The plot has a logarithmically scaled y-axis and shows the region with energies lower than 0.9 MeV. Below 0.4 MeV the events start to disappear because of the fading tigger efficiency.

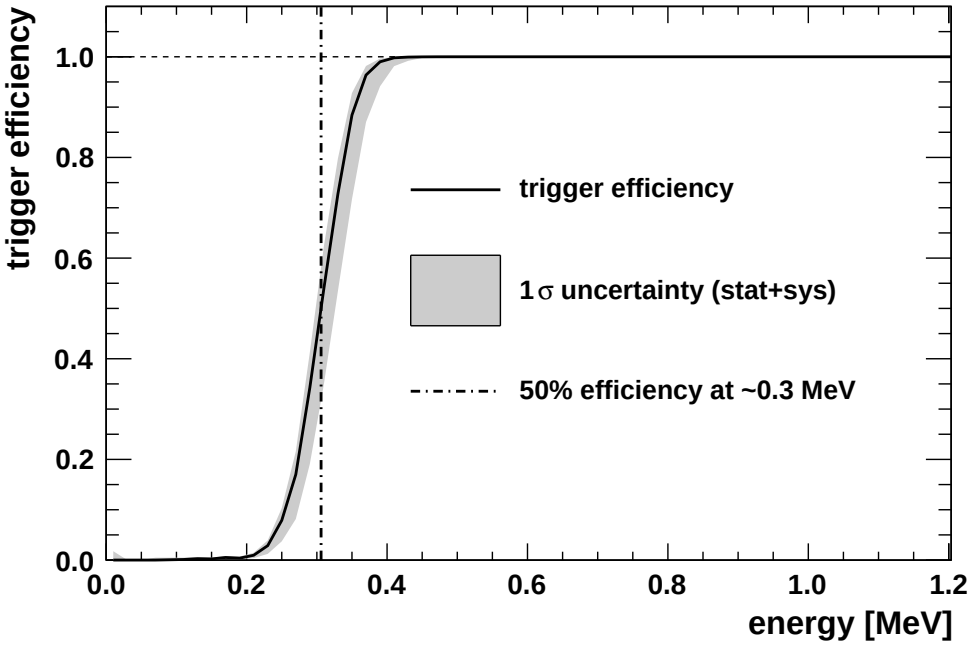

Figure 5.24: Trigger efficiency for single events in the Double Chooz far detector. For energies above 0.5 MeV, the trigger efficiency is practically 100 %. Below this energy it starts to drop quickly, the uncertainty is depicted by the gray area. This transition gets important for studies with low-energy events. Data und plot taken from [Stu13].

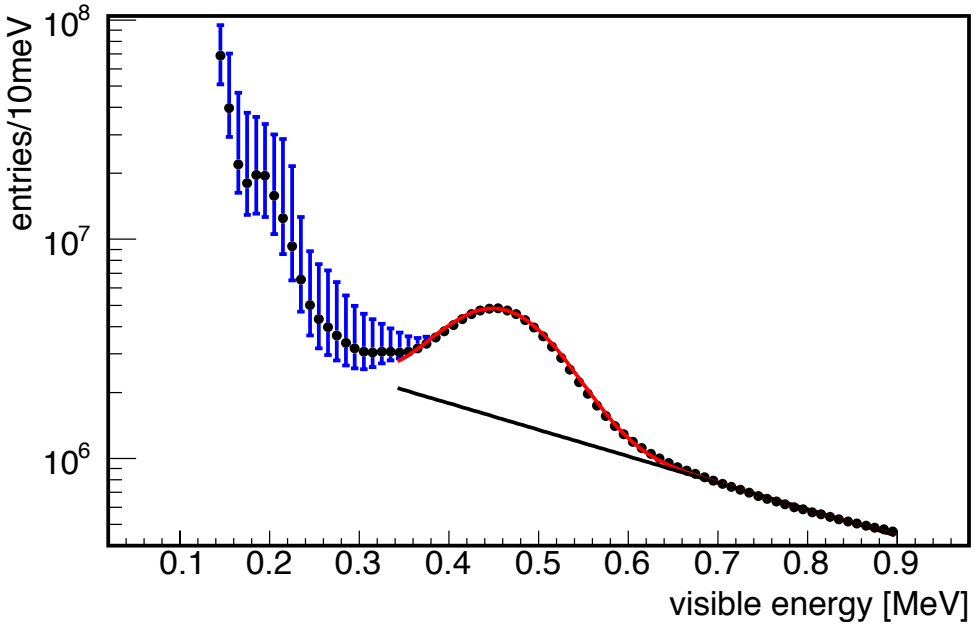

Figure 5.25: Far detector single event spectrum for the NT from a dataset with 466 days of live time. The energy spectrum was corrected for the trigger efficiency (see figure 5.24), details on the correction can be found in the text. The plot has a logarithmically scaled axis of ordinate and the error bars depict the uncertainty coming from the trigger efficiency. The fit function consists of an exponential background function (black) and a gaussian peak (red) for an evaluation of the excess (see equation 5.6). The mean value of the gaussian function was found to be at $453.9 \pm 1.2\,\mathrm{keV}$ and a total number of $5.15 \cdot 10^7$ possible ^{210}Po events is contained in the area between the two fit functions.

defined precisely by the fit, but due to the big uncertainty introduced by the trigger efficiency, σ from the gaussian fit was used as an error estimation, resulting in the big uncertainty quoted for the quenching factor. The calculated quenching factor is compatible with the value from the laboratory measurement of 13.1 ± 0.2 and is an indicator for the presence of events coming from the ^{210}Po decay in this peak.
In the worst case scenario, all events in the excess are coming from ^{210}Po decays. Under this assumption, the following numbers are a conservative upper limit on the (α,n) background contribution. For the spectrum in figure 5.25, the area between the exponential background function and the total fit function contains $5.15 \cdot 10^7$ events. Using the KamLAND estimation described above, this number of events leads to a ^{210}Po (α,n) background rate of $(3.7 \pm 0.5) \cdot 10^{-3}$ d^{-1} in the NT. This value is well below any other contributions to the correlated background in the Double Chooz far detector. In addition, this value was calculated from a conservative approach and is just an upper limit on the (α,n) rate.
Although the presented BiPo analysis used near detector data and the ^{210}Po analysis used far detector data, a great difference between both methods is obvious. The rate for the NT volume determined with the BiPo 214 analysis is $(1.05 \pm 0.13) \cdot 10^{-6}$ d^{-1} and the value calculated above is $(3.7 \pm 0.5) \cdot 10^{-3}$ d^{-1}. A possible explanation is that the radioactive equilibrium is broken and the detector contains much more ^{210}Po nuclei than expected. This additional radioactive impurity could have been introduced during the construction of the detector. Another possibility is that the origin of the events in the peak is not exclusively ^{210}Po. Even a remnant from the trigger efficiency correction could be an explanation. In either case, the conservative approach to the background contribution in the example of NT single events indicates that the (α,n) background can be neglected.

6 Chapter 6
Conclusions

There has been a huge progress in the field of neutrino physics during the last years. Since the first neutrino experiments in the sixties, many experiments have seen effects from neutrino oscillations and have determined important parameters. One example is the reduced flux of electron neutrinos coming from the sun. R. Davis firstly reported this deficit measured in a radiochemical experiment in an underground laboratory. A few years earlier, in 1962, the theoretical model of neutrino oscillations was born and it should take until the turn of the millennium until the change of neutrino flavor was confirmed by the Super-Kamiokande and SNO experiments. This achievement was rewarded with the Nobel Prize in 2015.
The current model of neutrino oscillations has six free parameters, the mixing angles θ_{13}, θ_{12} and θ_{23}, two squared mass differences Δm^2_{21} and Δm^2_{32} as well as a CP-violating phase δ. Besides a possible CP-violation due to δ, whose value is still unknown, all other values have been determined by several experiments to a high precision. Only a few years ago, Double Chooz was the first reactor neutrino experiment measuring a nonzero value for θ_{13}. With further contributions from Daya Bay and RENO, θ_{13} is now the best known mixing angle in terms of precision. The current combined best fit value is $\sin^2 2\theta_{13} = 0.085 \pm 0.005$ [Oli14]. The precise knowledge of all mixing angles and squared mass differences is a key to the determination of the CP-violating phase δ.
Other important properties of the neutrinos are still unknown: There are two possibilities for the mass hierarchy of neutrinos and their absolute masses are not determined yet. Furthermore, the question for the Majorana or Dirac nature of the neutrino is still unanswered. Several current and future experiments will address this issues.
One experiment providing a precise measurement of θ_{13}, is the Double Chooz reactor antineutrino experiment. Located at the Chooz nuclear power plant in France, it relies on a measurement with two identical detectors, canceling most of systematic uncertainties related to neutrino flux emission and detection. Each of the two pressurized water reactors in Chooz has a thermal power of 4.25 GW, which can

be translated into an electron antineutrino flux of $2 \cdot 10^{21}\,\mathrm{s}^{-1}$. The near detector, located at an average distance of 400 m from the two reactor cores, aims to monitor the $\bar{\nu}_e$ flux from the cores. The far detector, located near the expected first maximum of the oscillation at an average distance of 1 050 m from the reactor cores, measures an energy dependent deficit in the electron antineutrino spectrum. The reactor antineutrinos are detected using the inverse beta decay (IBD) inside the two liquid scintillator based detectors. This detection reaction has a relatively high cross-section of $10 \cdot 10^{-43}\,\mathrm{cm}^2$ for electron antineutrinos and has a threshold of 1.8 MeV. The expected sensitivity for the measurement of $\sin^2 2\theta_{13}$ is 0.015 for three years of data taking with both detectors (see figure 2.5). Improvements in the analysis techniques could presumably lower the precision to 0.01.
The Double Chooz far detector takes data since April 2011 and a total live time of 468 days has been analyzed. Furthermore, a remarkable period of 7.53 days with both reactors off was collected. This is unique amongst all reactor neutrino experiments and allows to put a constraint on the total background rate and provides a test for the background model. Data taking with both detectors has started at the beginning of the year 2015. A time period of about 5 months with data from far and near detector is available for analysis.
As part of this thesis, several tasks for the construction of the Double Chooz near detector were performed. For the filling of the near detector, $90\,\mathrm{m}^3$ of muon veto (MV) liquid scintillator and $100\,\mathrm{m}^3$ of buffer (BF) liquids were prepared. $175\,\mathrm{m}^3$ of liquids were delivered to Chooz, the different liquid components were mixed thoroughly and adjusted to the target density of $0.804\,\mathrm{g/cm}^3$. The liquid storage and handling facility close the far detector was reused for this purpose. Therefore, several transports with swap body tanks were carried out between the liquid storage area (LSA) area and the near detector laboratory.
At the Double Chooz near detector site, an unloading area with retention pits for the swapbody tanks was set up and an infrastructure for a trunk line connection to the near laboratory with a total length of 250 m was installed. The filling of the near detector was done successfully using a liquid and gas handling system called detector filling and operating system (DFOS). The processes for filling and the duty roster were optimized compared to the Double Chooz far detector filling. Including interruptions due to the liquids transport, the filling time was reduced to 22 days until the Double Chooz near detector filling was successfully completed on October 6th 2014. Compared to the far detector filling time of 2 months this is a great improvement.
The level measurement (LM) system is a crucial part for the safety of the Double Chooz detector. Strict margins were defined to keep the detector in a safe state. The allowed difference in differential gas pressure was set to 1 mbar. While the allowed difference in liquid level was set to 1 cm. The LM system needs to handle two different modes of operation. During the filling process a high periodicity of 2 s between measurements and a real time view of the measurement data was needed. Afterwards, during several years of monitoring, the measurements are done with a low periodicity of 2 min but have to be easily accessible remotely.

Another part of this thesis was the design of a completely new measurement system. A high modularity and expandability of the LM system were the keystones of the design concept. Therefore the design was based on common interfaces and technologies. The LM system was designed and built for the Double Chooz near detector, but there are enough spare parts to replace the existing system of the far detector. A cheap credit card sized computer was used as embedded system in the LM computer. Due to the restricted resources, a good performance of the used software and a low memory usage is required, which was implemented very efficiently.
Several sensors with different measurement principles are used in the LM system to get independent measurement values. Hydrostatic pressure sensors and sensors for absolute and differential gas pressure were calibrated accurately and were integrated to the LM system. Other sensors used for the system are laser distance measurement sensors, optical critical point sensors, weighing cells and a specialized level measurement system for the neutrino target (NT), called Tamago. Another system provided a relative liquid level measurement without relying on any electronics. All sensors worked as expected and formed a basis for a successful detector filling process.
The measurement electronics are specially designed for each purpose and are custom-made. A matching resolution for every sensor and a high exchangeability are the benefits of this efforts. The primarily used serial interface in the measurement system is the Inter-Integrated Circuit (I^2C) interface, which makes a broad variety of electronic components, like temperature sensors and analog-to-digital converters (ADCs), available. A downside of the I^2C bus is the small distance which is possible between the components. For the installation of the LM system a bus length up to 15 m was required, which is not possible with a I^2C bus. This drawback was successfully cancelled by using controller area network (CAN) hardware for the transmission of the logical interface. CAN is a field bus system which is broadly used in the automotive sector and could support a bus length up to 1 000 m. Besides the usage of a robust field bus hardware, the electronics for the LM system include voltage monitors and indicators of critical states to keep track of the health of the measurement system. An Universal Serial Bus (USB) to I^2C converter included in the system, ensures a high compatibility and can be used directly with all common linux kernels. For the other LM sensors like laser sensors, Tamago and weighing cells, which have a serial interface already included by the manufacturer, USB to serial interface converters were used for the connection to the measurement system.
A MySQL based monitoring software and a Qt based filling software were developed during this thesis. The monitoring software configures and controls the connected LM hardware, schedules the measurement events and stores all data in the database. The filling software provided real time access to the measurement data for the shifter in the near detector laboratory. The data was displayed graphically to show the time evolution of the measurement parameters and a basic toolbox allowed the shifter to manipulate the representation of the data and to get further information. All data gathered by the monitoring software, including the structure of the database, calibration data and descriptions are regularly transferred to a backup server. The database of the LM computer is mirrored to an external database which is easily

accessible over the internet. A web server provides all relevant information in a convenient way using the measurement values from the external database.
During the successful filling process of the Double Chooz near detector, the newly designed level measurement system proved its utilizability and made a secure filling of the detector possible. The hard restrictions on liquid level and gas pressure differences were met during the entire filling process. Since one year, the system is in monitoring mode and showed its reliability and easy handling in terms of maintenance and remote access. The possibility to extend the LM system was already used. Parameters from the expansion tank operating system (XTOS) were integrated seamlessly into the existing measurement system. A memory card with the operating system for the measurement computer including the newest version of the measurement software can be built from scratch automatically. This was already necessary once because of a corrupted memory card. A person unfamiliar with the system was able to prepare and replace the memory card on-site by running a dedicated script on a host computer. Furthermore, several power glitches and network failures did not harm the LM system and did not result in any loss of data. These irregularities and the simple maintenance and repair possibilities certify the success of the design concept for the new level measurement system.
Data taking with the Double Chooz far detector started in April 2011, the near detector was finished in October 2014 and data taking started within this year. Analysis of the data from both detectors enables a significant reduction of both reactor and detector related systematics uncertainties in the $\sin^2 2\theta_{13}$ measurement. For this thesis, data from the Double Chooz near detector with a total live time of 110.4 days was used. A key value are radioimpurities inside the Double Chooz detector. The mass concentration of uranium and thorium in the near detector was determined using BiPo coincidences. These events originate from the β-decay of ^{214}Bi and ^{212}Bi followed by the α-decay of ^{214}Po and ^{212}Po respectively. This technique provides a fast coincidence between β^- and α signals, which is also spatially correlated and can easily be distinguished from other background events. In the case of radioactive equilibrium, this can be used as a tag for events in the uranium and thorium decay chain.
The BiPo coincidences were extracted from a single events dataset using selection cuts. A prompt and delayed energy cut around the β Q-value of bismuth and the α Q-value of polonium respectively as well as a time difference cut corresponding to the life time of polonium were defined. Because of the spatial correlation between prompt and delayed event, an additional cut on the spatial difference further reduces the accidental events in the BiPo coincidence dataset. A total of $37\,914 \pm 195$ BiPo 214 coincidences and $11\,072 \pm 105$ BiPo 212 coincidences were found. A dedicated off-time window accidentals analysis provided a clean sample of $15\,483 \pm 124$ BiPo 214 like accidental coincidences and 54 ± 7 BiPo 212 like accidental coincidences respectively. The energy spectrum obtained from the respective analysis was used to remove accidental coincidences from the corresponding BiPo coincidence dataset. A constant rate of BiPo 214 coincidences indicates radioactive equilibrium in the uranium decay chain between ^{210}Pb and ^{238}U, or at least radon and its daughters.

The same behavior is found for the BiPo 212 coincidences, indicating radioactive equilibrium in the thorium decay chain. The measured half-life for ^{214}Po, obtained from the time difference distribution of BiPo 214 coincidences, is $161.9 \pm 1.6\,\mu$s, which agrees well with the literature value of $164.3 \pm 2.0\,\mu$s [Fir96]. The fitted half-life of ^{212}Po with $0.331 \pm 0.004\,\mu$s is slightly higher than expected, compared to the literature value of $0.299 \pm 0.002\,\mu$s [Fir96]. The delayed energy spectra of the coincidences showed a clear peak which was identified to stem from the α-decay of polonium. A cross-check was carried out in the case of BiPo 214 coincidences, calculating the α quenching factor for the gamma catcher (GC) and NT liquid scintillator. The determined values for an α energy of 7 687 keV are 12.27 ± 0.02 in the GC and 9.63 ± 0.04 in the NT. This agrees well with the values of 12.6 ± 0.6 (GC) and 9.8 ± 0.4 (NT) respectively from a laboratory measurement [Abe11].
Under the assumption of radioactive equilibrium, the mass concentration of uranium and thorium in the Double Chooz near detector was determined as part of this thesis. The total mass concentration of uranium in the ID was determined to be $(1.09 \pm 0.03) \cdot 10^{-14}$ g/g. For thorium, the mass concentration is found to be $(9.76 \pm 0.27) \cdot 10^{-14}$ g/g. Both values are a prove for the radioactive purity of the Double Chooz near detector and the total mass concentration of radioimpurities from uranium and thorium is well below the design goal of $< 2 \cdot 10^{-13}$ g/g. The mass concentration can also be translated into an (α,n) background rate which is found to be far below any other background contribution.
Another (α,n) background rate analysis is searching for ^{210}Po events in the detector data. The analysis principle was demonstrated using a dataset from the Double Chooz far detector, which confirmed the negligible (α,n) background contribution for the far detector.

A

Appendix A

Electronics

In this chapter the technical details of each electronic module used for the Double Chooz LM system will be described. A basic functional description of the circuits and the layout of the PCBs will be discussed. The general specifications and functions were already described in section 4.2.

A.1 USB to I^{2}C adapter with real-time clock and environmental data measurement

This module is used to get an interface between USB and I^{2}C bus. I can be used with a kernel module which is already included in most of the common linux kernels. The I^{2}C bus can be accessed directly from the operating system. The module also includes a RTC and a temperature and pressure sensor to monitor environmental conditions.
The circuit of the USB to I^{2}C adapter is shown in figure A.1. The main part is IC1 an ATtiny45 microcontroller [Atm15]. It is driven by quartz Q1 with a clock frequency of 12 MHz. PB0 and PB2 of IC1 are used for the completely software driven USB interface. Since a supply voltage of +5 V is used for all logic components the voltage level has to be adjusted to the specifications of the USB interface. In this case it is enough to break the voltage above +3.6V towards ground. Zener diodes D1 and D2 in each USB data line achieve this level conversation. The +5 V power supply (pin 1 of X1) is not used, an external power supply has to be connected to SL1. Only pin 4 of X1 is connected to get a common ground. PB5 of IC1 is used for the serial clock (SCL) line and PB1 of IC1 is used for the serial data (SDA) line of the I^{2}C bus. The ATtiny45 microcontroller acts as master on the I^{2}C bus and is again completely software driven. The I^{2}C bus is shared amongst the electronic modules via a boxed header SV1, flat ribbon cables are used for electrical connection. Pins 3 and 4 are always used to get a common ground amongst the electronic modules,

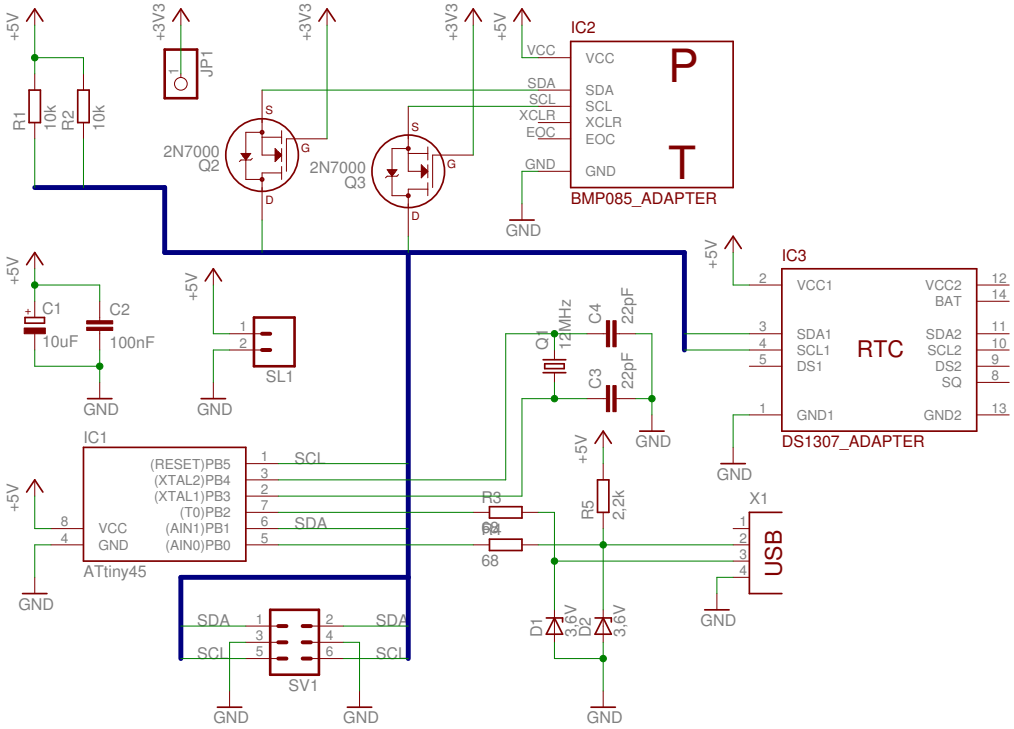

Figure A.1: Circuit diagram of the USB to I^{2}C adapter. A detailed description of the components can be found in the text.

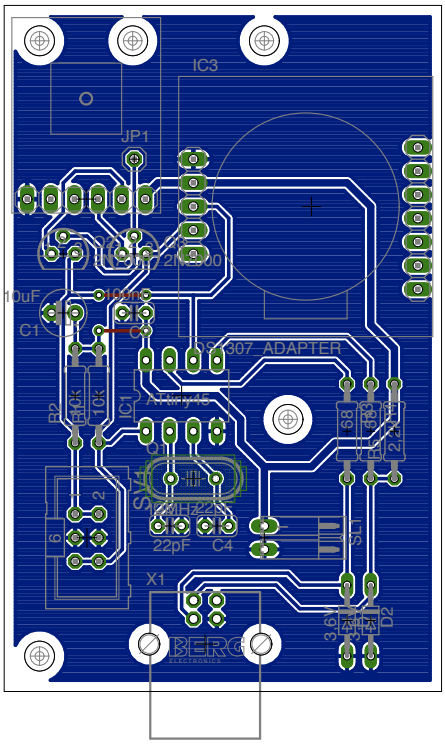

Figure A.2: PCB layout of the USB to I²C adapter. The one-sided layout has a size of 47 mm × 74 mm and has drill holes matching the layout of other modules to allow stacking with 20 mm straight connectors.

pins 1 and 2 are connected to SDA and pins 5 and 6 are connected to SCL. The I²C bus requires a pull-up resistor on SDA and SCL which is done by R1 and R2.

For several reasons, already described in section 4.2.1, a RTC with I²C interface [Max15] was needed. The DS1307 can be bought as a module with support electronics and battery already included, so it can be connected directly to the I²C bus and the power supply (IC3).

IC2 is a BMP085 from Bosch [Bos15], a temperature and barometric pressure sensor on a module. The module comes with support electronics and can be connected to a wide range of supply voltages, +5 V like all other logic components in that case. But it works with +3.3 V internal voltage and needs therefore +3.3 V levels on the I²C bus, too. This voltage conversation is achieved by field effect transistors Q2 and Q3. Drain is connected to the common I²C bus with +5 V voltage level, source is connected to the DS1307 module. To get the voltage level conversation working, the transistors gate has to be connected to +3.3 V. Since the DS1307 module has its own voltage regulator to adjust the supply voltage, a wire was welded directly onto it and was connected to JP1 on the module the get this voltage level. This is important to note, because this connection is not drawn in the circuit.

Figure A.2 shows the PCB layout of the USB to I²C adapter. For this rather simple

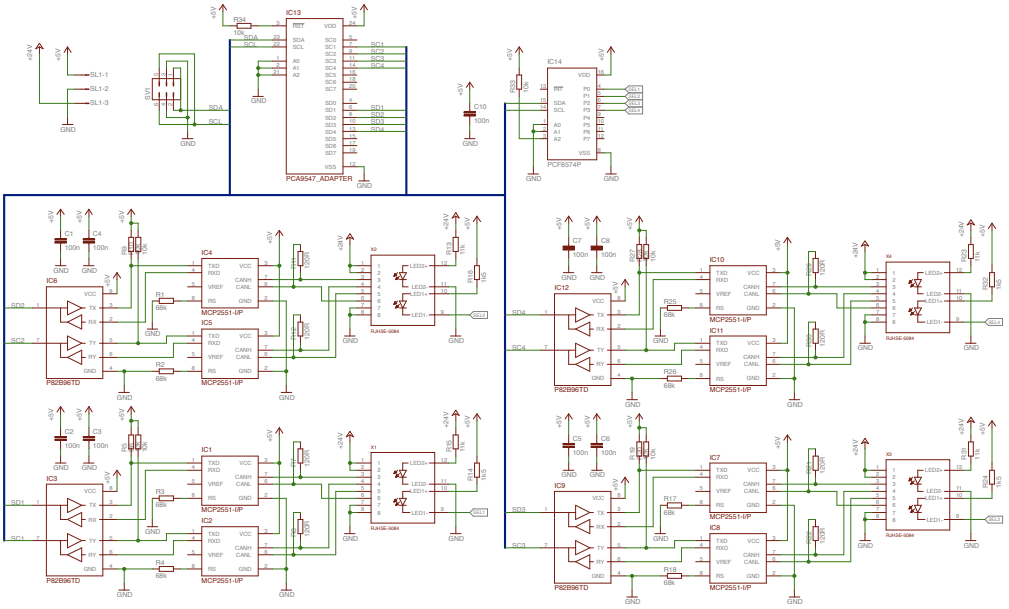

Figure A.3: Circuit diagram of the I^{2}C multiplexer. A detailed description of the components can be found in the text.

circuit a one-sided PCB was enough. A standard USB type B connector sits in front of the PCB with a dimension of 47 mm × 74 mm. The four outermost drill holes and the position of the boxed header match the layout of other electronic modules to allow stacking with straight connectors. The fifth drill hole is only for supporting the RTC module.

A.2 I^{2}C multiplexer with power supply over Ethernet

This module with I^{2}C interface is able to switch between four different channels to connect several sensor modules. The data is transferred using CAN hardware to extend the range of the I^{2}C bus. The data lines are distributed together with +24 V power supply over standard Ethernet cables.

The circuit of the I^{2}C multiplexer is shown in figure A.3. The power supply is connected to SL1, +5 V are used for the electronics on the module and +24 V are provided over the Ethernet cable connection to the sensor modules. Normally this module is connected to a USB to I^{2}C adapter via boxed header SV1. IC13 is responsible for switching between the four different subgroups of the I^{2}C network. The PCA9547 is able to switch between eight I^{2}C channels but only four are used for this module.

To transmit the I^{2}C data over CAN hardware, four groups of electronics, one for each channel, are included on the module. The principle is described in the example of the lower left group, connected to the SC1 and SD1 channel of IC13. A bidirectional

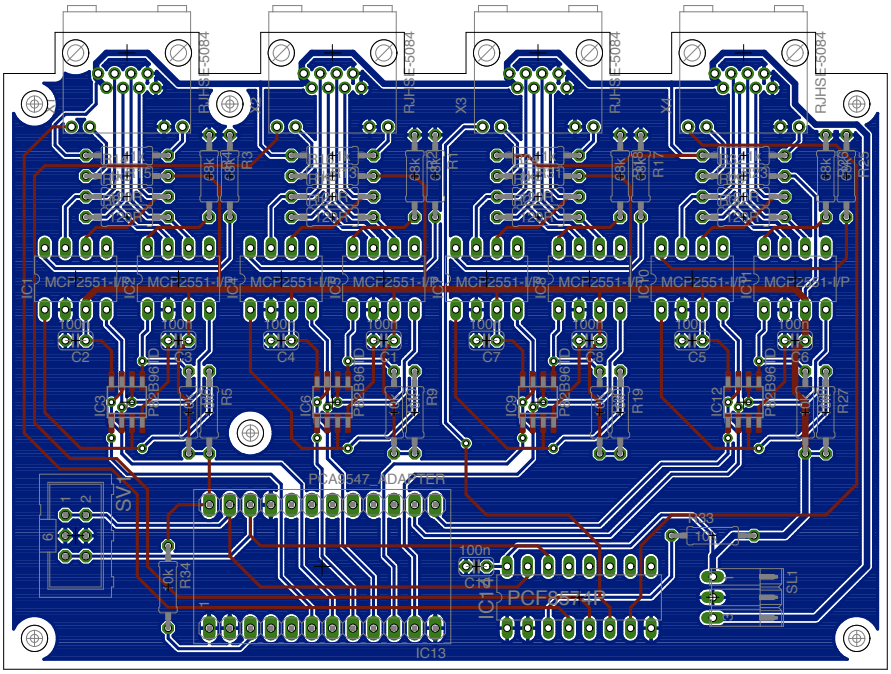

Figure A.4: PCB layout of the I²C multiplexer. The two-sided layout has a size of 109 mm × 81 mm and has drill holes matching the layout of the USB to I²C adapter module to allow stacking with 20 mm straight connectors.

bus buffer of the type B82P96 is used as IC3 to create a non-latching logical interface for both lines SDA and SCL and to exceed the restrictions of the I²C bus. For each pair of data lines there is a MCP2551 CAN transceiver, here IC1 and IC2, to use the benefits of a robust field bus for the data connection to the sensor modules. The data lines for SDA are connected to pins 3 and 6 of X1 and the data lines for SCL are connected to pins 4 and 5 of X1, an RJ-45 connector. This configuration uses a twisted pair of wires for each set of the data lines inside the connected Ethernet cable. As mentioned before, the remaining wire pairs are used for power supply, pins 1 and 2 for +24 V and pins 7 and 8 for ground. The RJ-45 connector X1 has two LEDs, the green one is connected to the +24 V power supply of the connector to monitor the sensor module power supply and the yellow one is connected to an input/output line of IC14.

IC14 is a PCF8574 a 8-bit inout/output port expander for the I²C bus which allows to control eight independent logical input or output lines. Only four of them are used to switch the second LED on the RJ-45 connectors. This software driven solution shows the connector, which is currently selected from IC13 and is connected to the I²C interface SV1.

Figure A.4 shows the PCB layout of the I²C multiplexer. This is a two-sided PCB layout not only because of some surface-mounted device (SMD) components but also because of the rather complex circuit. It has a dimension of 109 mm × 81 mm

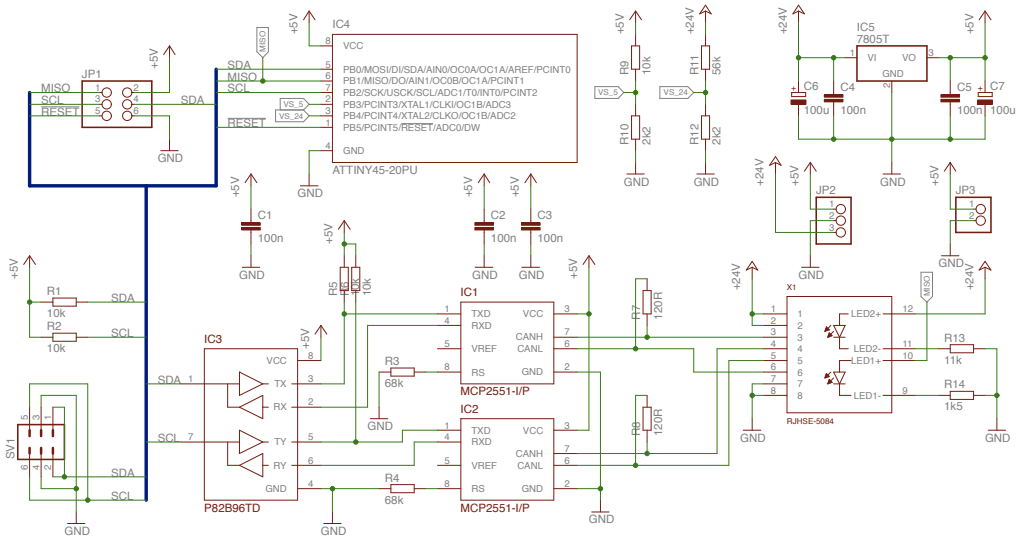

Figure A.5: Circuit diagram of the CAN to I^{2}C converter. A detailed description of the components can be found in the text.

and has drill holes for four RJ-45 connectors which are directly mounted on the PCB. The four drill holes on the left side in figure A.4 are designed to match the drill holes of the USB to I^{2}C adapter the other two drill holes are for mounting the module itself.

A.3 CAN to I^{2}C converter with voltage monitor

This module is directly connected to a multiplexer module over a single Ethernet cable with power supply and serial interface. It provides power supply for the sensors modules and electronic components on all sensor modules. It uses an I^{2}C interface for connection to the sensor modules.
The circuit of the CAN to I^{2}C converter is shown in figure A.5. The electronics for the conversion of the bidirectional logic interface using CAN hardware to I^{2}C interface is the same as for the multiplexer module (see section A.2 for details). The Ethernet cable with power supply and serial interface is connected to the RJ-45 connector X1. The I^{2}C bus is used for the module itself and is connected to the 6pin boxed header SV1 for connection to the sensor modules. The I^{2}C bus requires a pull-up resistor on SDA and SCL which is done with R1 and R2.
The +24 V power supply connected to X1 is directly passed to pin header JP2 for connection to the sensor modules and is connected to the green LED in X1 to show the status of the power supply. A voltage regulator (IC5) and four capacitors C4 to C7 create a stabilized +5 V voltage level which is used for the electronics on the module and for the sensor module electronics connected over pin header JP3.
IC4 is an ATtiny45 microcontroller [Atm15] driven by its internal quartz with a

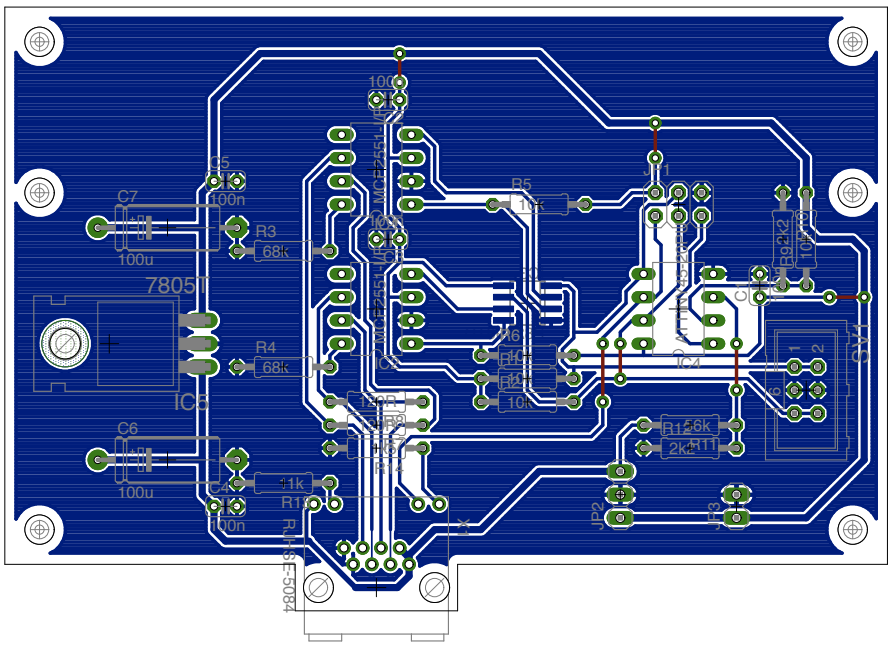

Figure A.6: PCB layout of the CAN to I²C converter. The one-sided layout has a size of 97 mm × 66 mm and has drill holes matching the layout of the sensor modules to allow stacking with 20 mm straight connectors.

clock frequency of 1 MHz. An ISP interface is available over pin header JP1 for programming the microcontroller without removing it from the LM system. The ATtiny45 has two built-in 8-bit ADCs which are used as a voltage monitor for the +24 V and +5 V voltage levels. They are connected over two voltage dividers R11/R12 and R9/R10 to pin 3 and pin 4 of IC4 respectively to match the internal 1.1 V voltage reference. The ADC values will be sent over the I²C bus once requested by the master. To use IC4 as slave on the I²C interface and to set the device address, a completely software driven solution was included in the ATtiny45 firmware. If the CAN to I²C converter is connected to a serial interface which is selected or deselected by the multiplexer module, it is able to detect this change in connection status with broadcast commands sent by the master. IC4 will display this status with a yellow LED included in X1 and connected to pin 6 of IC4 which is configured as logical output.

Figure A.6 shows the PCB layout of the CAN to I²C converter. For this module a one-sided PCB layout was enough, the only SMD part IC3 was mirrored to the bottom layer of the layout. It has a dimension of 97 mm × 66 mm and includes a directly mounted RJ-45 connector. The voltage regulator IC5 has a thermal connection to the housing of the sensor module over a small metal sheet to regulate the temperature of IC5. The drill holes match the layout of all sensor modules to allow stacking with straight connectors.

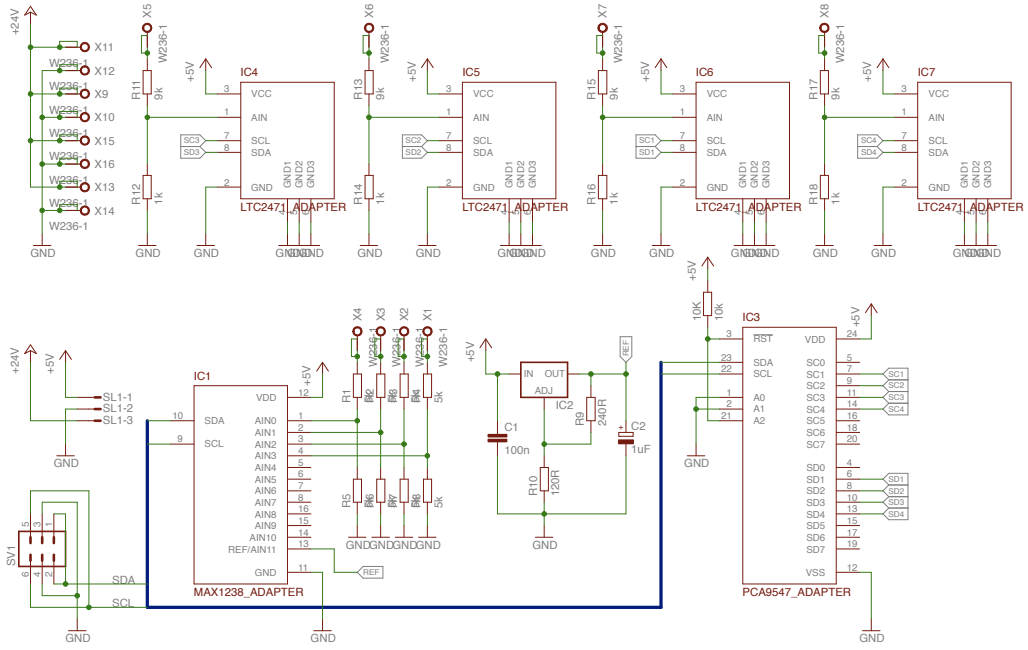

Figure A.7: Circuit diagram of the ADC module for hydrostatic pressure sensors. A detailed description of the components can be found in the text.

A.4 ADC module for hydrostatic pressure sensors

This module is normally used together with a CAN to I^2C converter and provides +24 V power supply for the connected HPSs. Is is able to measure hydrostatic pressure using 16-bit ADCs and liquid temperature using a 12-bit ADC. All ADCs are connected to the I^2C interface and the ADC values can be read directly over the serial interface.

The circuit of the ADC module for hydrostatic pressure sensors is shown in figure A.7. 6pin boxed header SV1 is the same as for all other modules and is used for connection to the I^2C bus. +24 V and +5 V power supply provided by the connected CAN to I^2C converter is attached to pin header SL1 and is distributed to the terminal block (X9 to X12) for sensor power supply. The +5 V power supply is used only for the electronic parts on the module itself.

For the hydrostatic pressure measurement (sensor output connected to X5 to X8), LTC2571 16-bit ADCs (IC4 to IC 7) are used for every channel. The input voltage is reduced using voltage dividers (R11 to R18) and is connected to the analog input of the ADCs (pin 1). Since there is no programmable bus address for a LTC2571 ADC, a I^2C bus multiplexer (IC3) is needed to switch between the ADCs . For the liquid temperature measurement, a MAX1238 multichannel 12-bit ADC (IC1) is used for conversion. The MAX1238 also has a fixed bus address, but since there is only one on this sensor module, it is directly connected to the serial interface. The LTC2571 16-bit ADCs have their own fixed internal voltage reference which is used

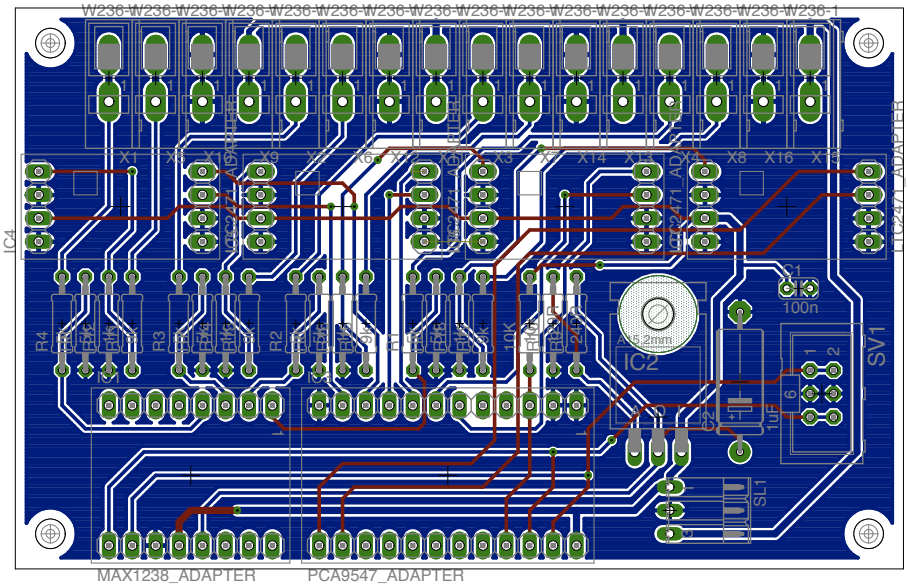

Figure A.8: PCB layout of the ADC module for hydrostatic pressure sensors. The two-sided layout has a size of 97 mm × 61 mm and has drill holes matching the layout of the CAN to I²C converter to allow stacking with 20 mm straight connectors.

for the hydrostatic pressure conversion. The same applies for the MAX1238 ADC, but there is the possibility to use an external voltage reference which can range from ground potential to the supply voltage of +5 V for IC1. Voltage regulator IC2, together with capacitors C1, C2 and resistors R9, R10, is able to provide a voltage reference in a broad range, depending on the resistor values, which is connected to pin 13 of IC1. This option was not used in the case of the ADC module for hydrostatic pressure sensors because the internal voltage reference was sufficient for liquid temperature measurement. The temperature sensor outputs are connected to X1 to X4 and the measured voltage is divided by a factor of 2 with resistors R1 to R8. The reduced voltage is directly connected to the first four channels (pins 1 to 4) of IC1.

Figure A.8 shows the PCB layout of an ADC module for hydrostatic pressure sensors. A two-sided layout was needed for proper routing. All sensitive electronic parts are include as adapters with 2.54 mm spacing. Several adapters are available as spare parts and allow swapping of broken parts without the ability of soldering SMD parts. The dimensions are 97 mm × 61 mm and the module has drill holes matching the layout of the CAN to I²C converter to allow stacking with 20 mm straight connectors.

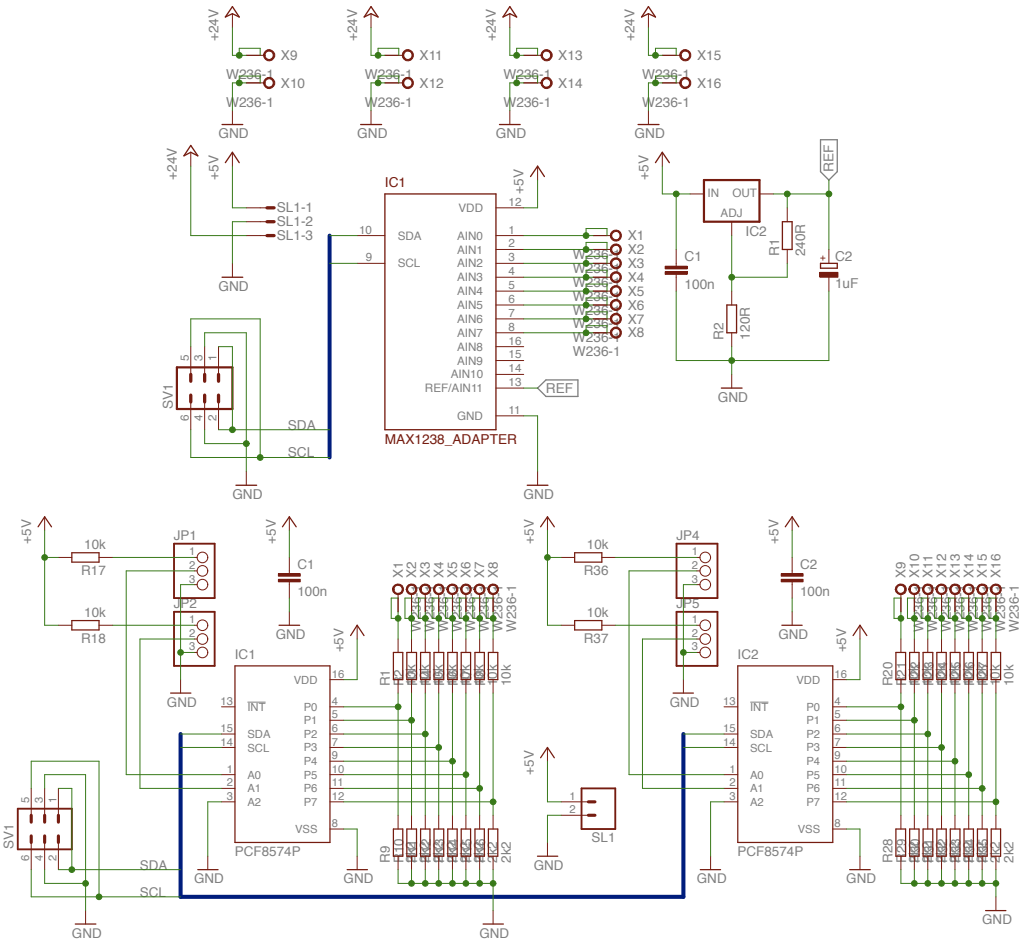

Figure A.9: Circuit diagram of the ADC module for gas pressure sensors. A detailed description of the components can be found in the text.

A.5 ADC module for gas pressure sensors

This ADC module is used to measure the value of all eight gas pressure sensors together with their sixteen so called hardware triggers, digital outputs which are pulled high if a gas pressure value exceeds a predefined limit. The values of the multichannel 12-bit ADC and the status of the hardware triggers monitored by two port expanders are available over the I^2C bus. This module is normally used together with a CAN to I^2C converter and provides +24 V power supply for the connected gas pressure sensor amplifiers.

The circuit diagram for both parts of the ADC module for gas pressure sensors is shown in figure A.9. The pin header SL1 for power supply and 6pin boxed header SV1 are common for both parts of the circuit. In the upper part, IC1 a MAX1238 multichannel 12-bit ADC is used for conversion of the measured gas pressure. The amplifiers attached to the gas pressure sensors, provide an analog voltage propor-

tional to the measured gas pressure. This voltage is directly connected to the first eight input channels of the ADC (pins 1 to 8). Since the internal voltage reference of the MAX1238 does not match the maximal analog voltage coming from the amplifiers, an external voltage reference (pin 13) is used to maximize the measurement resolution. Voltage regulator IC2, together with capacitors C1, C2 and resistors R1, R2, is able to provide a stabilized voltage reference suitable to be compared to the analog output of the amplifiers.
The lower part shows the monitoring of the hardware triggers. The output voltage is switched between 0 and +24 V, which is far to high for the used electronics. A voltage divider for each channel reduces this voltage roughly by a factor of 5. This reduced voltage acts like a logical input for a logical device driven with +5 V and is therefore directly connected to the digital input of IC1 and IC2 respectively. This are two PCF8547 port expanders which can be read over the I^2C interface. Each port expander has three address bits, so eight of them can be used on the same I^2C bus. The highest address bit A2 (pin 3) is pulled to ground, leaving four possible addresses which can be selected via JP1, JP2 and JP4, JP5. Two addresses and one jumper would be enough for the planned configuration of an ADC module for gas pressure sensors, but the second jumper leaves the possibility to extend the module with two further port expanders for monitoring or controlling other devices like horns or alert sensors.
Figure A.10 shows the PCB layout of an ADC module for gas pressure sensors. Due to the separation into two parts, an one-side layout for both part was enough. Again, the ADC is included as adapter to avoid SMD part soldering in case of a replacement. The footprint of the two stacked parts has a dimension of 97 mm × 61 mm. The shifted placement of the terminal blocks ensures accessibility of every connector even in mounted configuration. The drill holes match the layout of the CAN to I^2C converter and would allow further stacking.

A.6 ADC module for critical point sensors

This ADC module is used to measure the reflected light intensity of all CPSs together with their four so called hardware triggers, digital outputs which are pulled high if the measured intensity drops below a predefined limit. The values of the multichannel 12-bit ADC and the status of the hardware triggers monitored by a port expander are available over the I^2C bus. This module is normally used together with a CAN to I^2C converter and provides +24 V power supply for the connected CPS amplifiers.
The circuit of the ADC module for critical point sensors is shown in figure A.11. As for the other ADC modules, +5 V and +24 V power supply from the CAN to I^2C converter is connected to pin header SL1 and 6pin boxer header SV1 is used for the connection to the I^2C bus. A special feature of the amplifiers connected to the CPSs, is the ability to adjust the amplification of the analog output voltage proportional to the the measured intensity. This allows to connect the analog output directly to

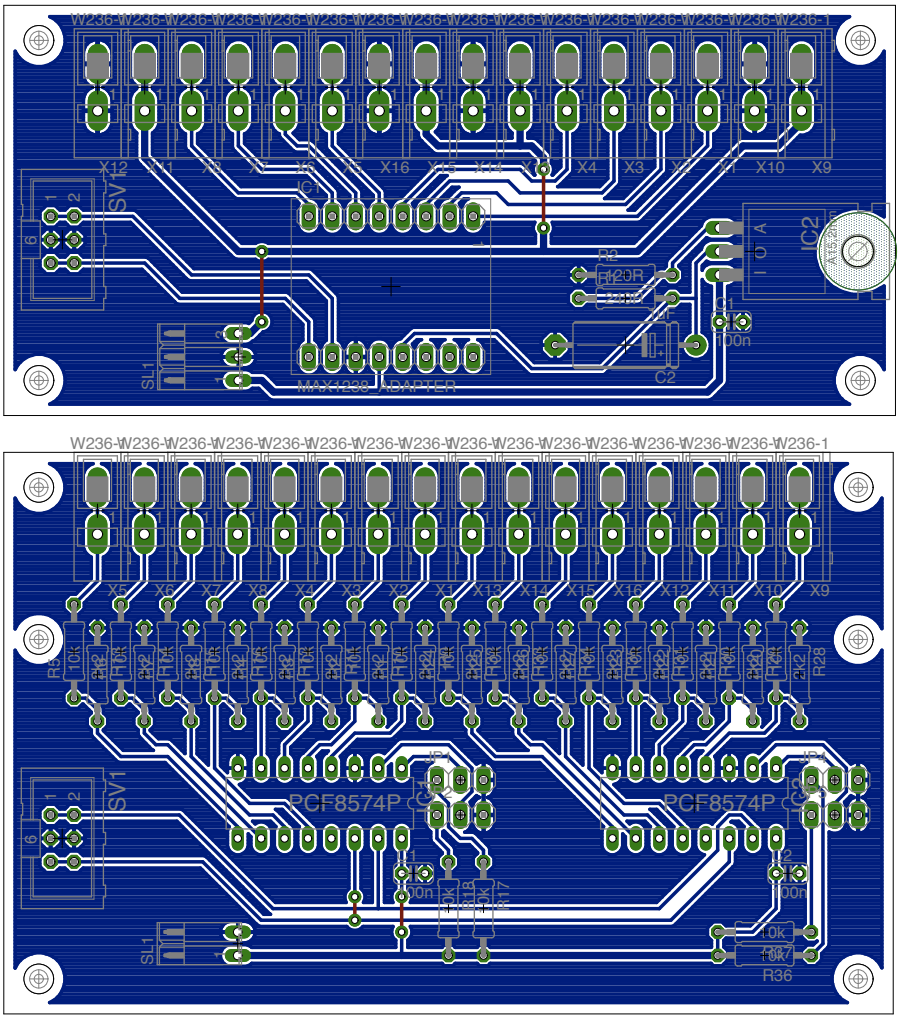

Figure A.10: PCB layout of the ADC module for gas pressure sensors. The one-sided layout has a size of 97 mm × 44 mm (upper part) and 97 mm × 61 mm (lower part). Both PCBs have drill holes matching the layout of the CAN to I²C converter and against each other to allow stacking with 20 mm straight connectors.

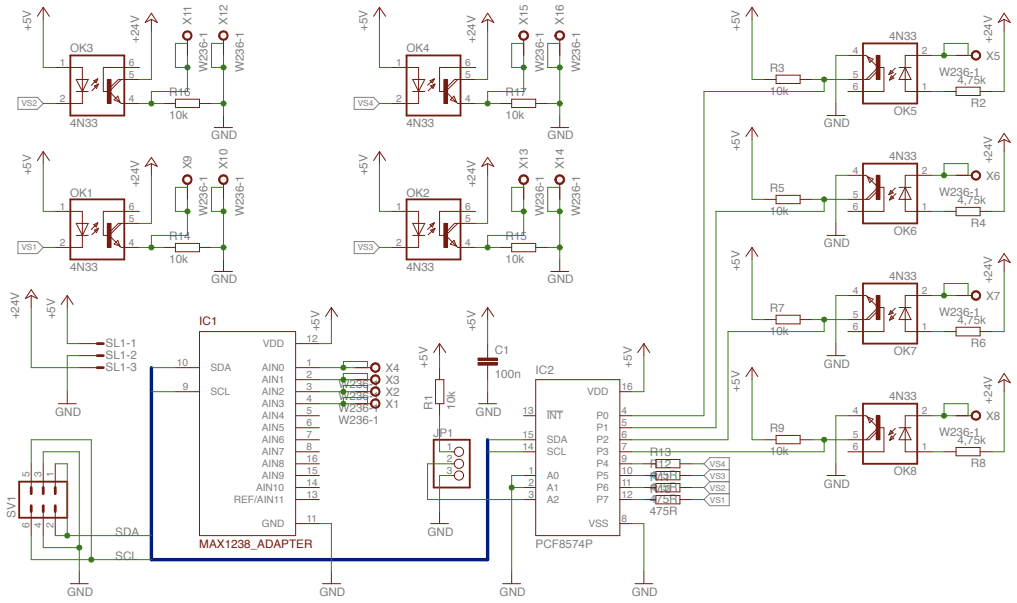

Figure A.11: Circuit diagram of the ADC module for critical point sensors. A detailed description of the components can be found in the text.

the first four channels of IC1 (pins 1 to 4) and adjust the amplifier output voltage accordingly to match the internal reference voltage of the ADC. This is also the reason for not including an external reference from a voltage regulator as for the ADC modules described before.

IC2 is a PCF8574 I^2C port expander with three selectable address bits. Here, A0 and A1 (pins 1 and 2) are pulled to ground and A2 can be changed using jumper JP1. Again this is no mandatory for only one port expander, but allows the expansion of the module with further functionality. A drawback of the used sensor amplifiers is the PNP output in contrast to the NPN outputs of all other amplifiers used in the measurement system. Because of this, there is no trick such as voltage dividers to create a logical input as shown in the case of the ADC module for gas pressure sensors. Here, optocouplers OK5 to OK8 are used to generate a logical signal connected to pins 4 to 7 of port expander IC2 used as logical input. The principle will be illustrated with optocoupler OK5. If the PNP output of the amplifier is active, X5 is pulled to +24 V and the LED between pin 1 and 2 of OK5 will stay dark. The transition between pin 4 and 5 of OK5 is blocked and pull-up R3 will create a high state on logical input P0 (pin 4) of port expander IC2. If the PNP output is inactive, the LED between pin 1 and 2 will open the transition between pin 4 and 5 and the logical input is pulled to ground.

The remaining four input/output ports P4 to P7 (pins 9 to 12) of port expander IC2 are used as logical output to control the power supply of each connected sensor separately. The LEDs of optocouplers OK1 to OK4 are connected to the logical output together with a series resistor. If the logical output is high, pin 4 of the

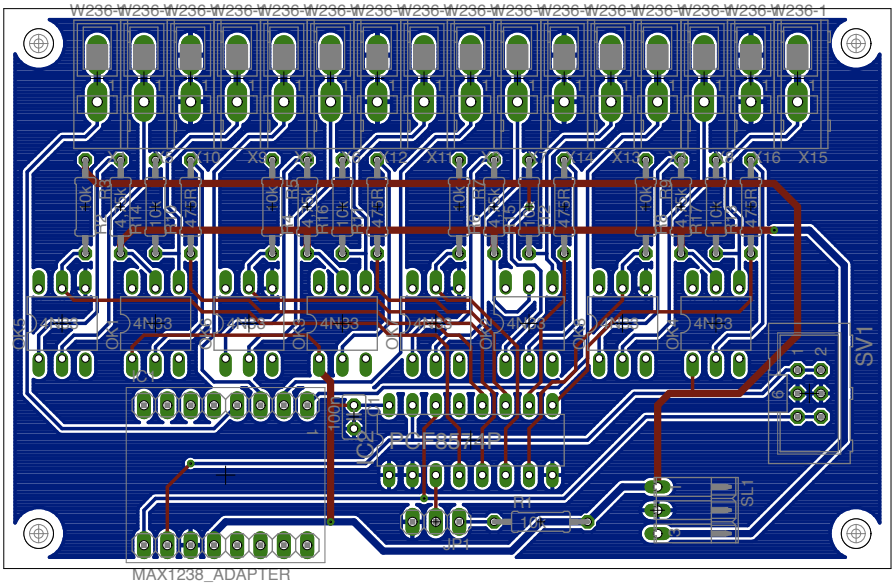

Figure A.12: PCB layout of the ADC module for critical point sensors. The two-sided layout has a size of 97 mm × 61 mm and has drill holes matching the layout of the CAN to I^2C converter to allow stacking with 20 mm straight connectors.

optocoupler will be connected to +24 V and the voltage drop around resistors R15 to R17 will be used as power supply for the sensors attached to connectors X9 to X16. If the logical output is low and the optocoupler LED is dark, the resistors will create a controlled shortcut in the sensors power supply.
Figure A.12 shows the PCB layout of an ADC module for critical point sensors. Due to the large amount of chips used for this module, a two-sided layout was required to allow proper routing. As before, the ADC is included as adapter to avoid SMD part soldering in case of a replacement. The module has a dimension of 97 mm × 61 mm and its drill holes match the layout of the CAN to I^2C converter to allow stacking with straight connectors.

B

Appendix B

Uranium and thorium decay chains

In this chapter the complete decay chains of ^{238}U and ^{232}Th are shown. Most of the decays of heavy isotopes coming from natural radioactivity, are isotopes included in this two decay chains. ^{238}U and ^{232}Th are both primordial isotopes. ^{238}U has a natural abundance of 99.3 % and ^{232}Th a natural abundance of 100 %. The short decay time of ^{214}Po can be used as coincidence measurement to tag the number of decays within the uranium decay chain or, at least, radon and its daughters. The same applies for ^{212}Po and the thorium decay chain accordingly.

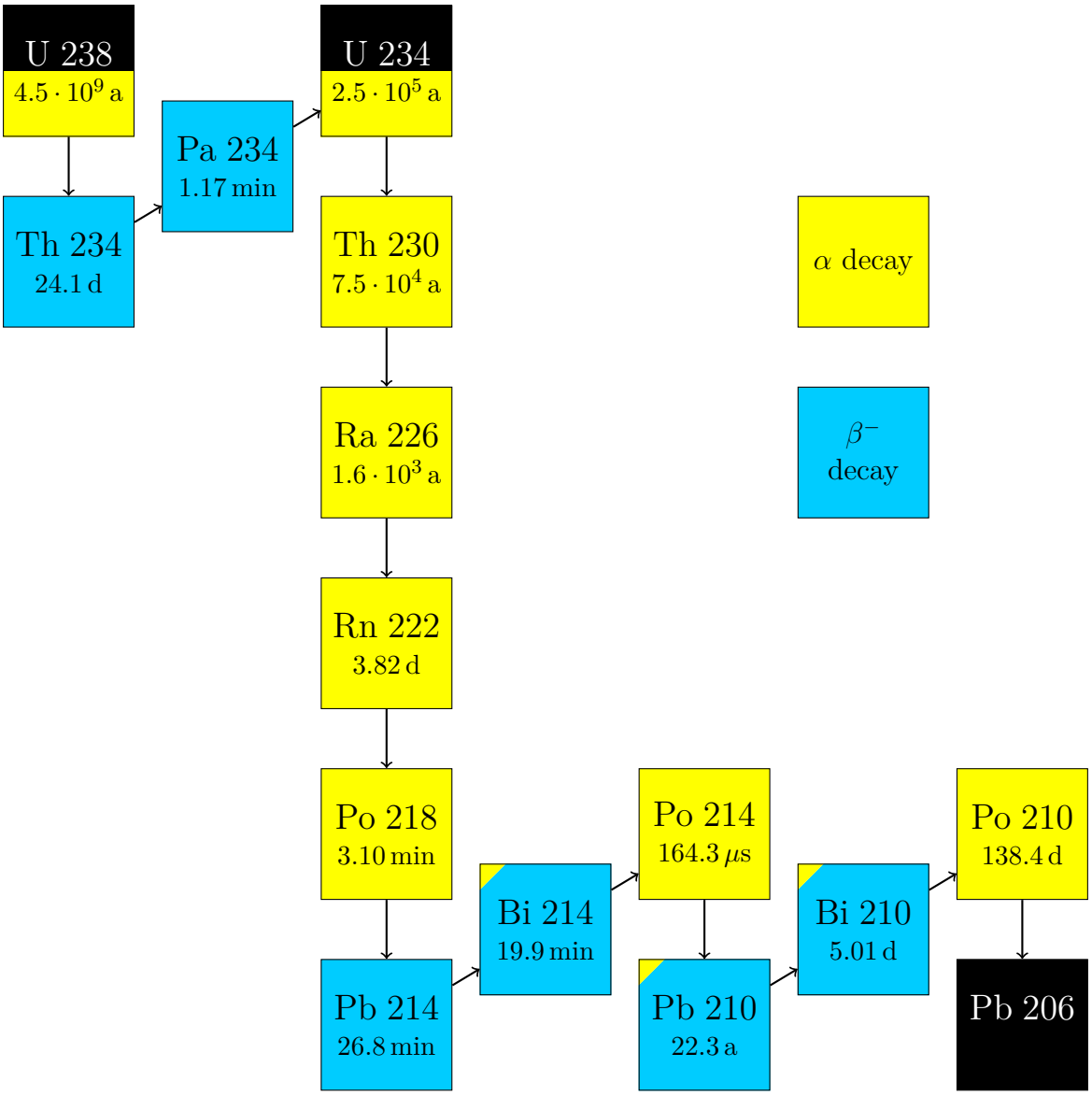

Figure B.1: Decay scheme of ^{238}U. The fast coincidence between ^{214}Bi and ^{214}Po can be used to tag radioimpurities coming from this decay chain. The chain can be broken because of the long life time for isotopes with mass number 226 or greater. Data taken from [Fir96].

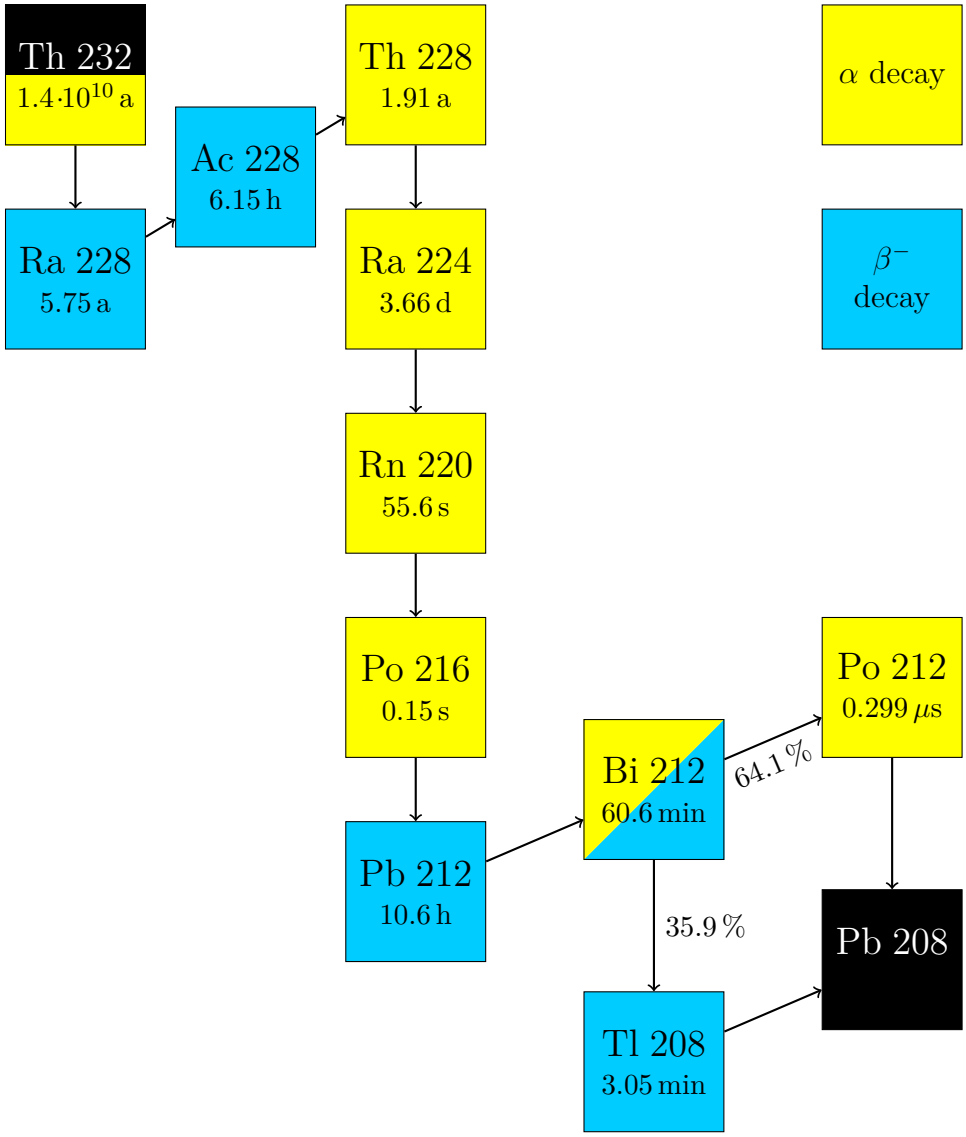

Figure B.2: Decay scheme of ^{232}Th. The fast coincidence between ^{212}Bi and ^{212}Po can be used to tag radioimpurities coming from this decay chain. Data taken from [Fir96].

List of Figures

List of Tables

Glossary

ADC analog-to-digital converter

BF buffer

CAN controller area network

controller area network bus Standard industry vehicle bus. The development was started at Robert Bosch GmbH in 1983.

CPS critical point sensor

critical point sensor Trigger for liquid level at critical filling points, see section 4.1.3 for details.

cross reference system Differential liquid level measurement system, see section 4.1.6 for details.

detector filling and operating system Arrangement of valves, filters and pumps for handling liquids during filling. There is one module for every detector volume.

DFOS detector filling and operating system

expansion tank operating system Expansion tanks connected to the inner three detector vessels. Allows liquid expansion due to temperature changes in the detector.

GC gamma catcher

HPS hydrostatic pressure sensor

hydrostatic pressure sensor Sensor for measuring liquid level and temperature, see section 4.1.1 for details.

I^2C Inter-Integrated Circuit

IBC intermediate bulk container

IBD inverse beta decay

ID inner detector

inner detector The three innermost volumes of the detector, neutrino target, gamma catcher, buffer are referred to as inner detector.

Inter-Integrated Circuit bus Serial computer bus with the possibility to connect multiple masters and slaves. It was designed by Philips Semiconductor in 1982.

ISP in-system programming

IV inner veto

LED light-emitting diode

LM level measurement

Loris Tube Inverted syphon used to translate a detector liquid level to a guide tube for laser distance measurement.

LSA liquid storage area

MV muon veto

NT neutrino target

NTP network time protocol

OV outer veto

PCB printed circuit board

PMT photomultiplier tube

PTFE Polytetrafluoroethylene

RTC real-time clock

SCL serial clock

SDA serial data

SMD surface-mounted device

USB Universal Serial Bus

XRS cross reference system

XTOS expansion tank operating system

Bibliography

[Aba12] K. N. Abazajian: *"Light Sterile Neutrinos: A White Paper"*, arXiv:hep-ph/1204.5379v1 (2012).

[Abe14a] K. Abe et al.: *"Precise Measurement of the Neutrino Mixing Parameter θ_{23} from Muon Neutrino Disappearance in an Off-Axis Beam"*, Phys. Rev. Lett. **112** (2014) 18, 181801 [arXiv:1403.1532 [hep-ex]].

[Abe14b] Y. Abe et al.: *"Background-independent measurement of θ_{13} in Double Chooz"*, Phys. Lett. B **735** (2014) 51 [arXiv:1401.5981 [hep-ex]].

[Abe14c] Y. Abe et al.: *"Improved measurements of the neutrino mixing angle θ_{13} with the Double Chooz detector"*, JHEP **1410** (2014) 086 [arXiv:1406.7763 [hep-ex]].

[Abe13a] Y. Abe et al.: *"First Measurement of θ_{13} from Delayed Neutron Capture on Hydrogen in the Double Chooz Experiment"*, Phys. Lett. B **723** (2013) 66 [arXiv:1301.2948 [hep-ex]].

[Abe13b] Y. Abe et al.: *"Direct Measurement of Backgrounds using Reactor-Off Data in Double Chooz"*, Phys. Rev. D **87** (2013) 1, 011102 [arXiv:1210.3748 [hep-ex]].

[Abe12a] Y. Abe et al.: *"Indication for the disappearance of reactor electron antineutrinos in the Double Chooz experiment"*, Phys. Rev. Lett. **108** (2012) 131801 [arXiv:1112.6353 [hep-ex]].

[Abe12b] Y. Abe et al.: *"Reactor electron antineutrino disappearance in the Double Chooz experiment"*, Phys. Rev. D **86** (2012) 052008 [arXiv:1207.6632 [hep-ex]].

[Abe11] C. Aberle: *"Optimization, simulation and analysis of the scintillation signals in the Double Chooz experiment"*, PhD thesis (2011).

[Abe08] S. Abe et al.: *"Precision Measurement of Neutrino Oscillation Parameters with KamLAND"*, Phys. Rev. Lett. **100** (2008) 221803 [arXiv:0801.4589 [hep-ex]].

[Ada14] P. Adamson et al: *"Combined Analysis of ν_μ Disappearance and $\nu_\mu \rightarrow \nu_e$ Appearance in MINOS Using Accelerator and Atmospheric Neutrinos"*, Phys. Rev. Lett. **112**, 191801 (2014).

[Aha00] B. Aharmim: *"Neutrino physics"*, arXiv:hep-ph/0001264v2 (2000).

[Alt14] G. Altarelli: *"Status of Neutrino Mass and Mixing"*, arXiv:hep-ph/1404.3859v1 (2014).

[Alt05] M. Altmann et al.: *"Complete results for five years of GNO solar neutrino observations"*, Phys. Lett. **B 616**, arXiv:hep-ex/0504037v1 (2005).

[Ams07] C. Amsler: *"Kern- und Teilchenphysik"*, Utb Verlag, 1st edition (2007).

[Apo03] M. Apollonio et al.: *"Search for neutrino oscillations on a long base-line at the CHOOZ nuclear power station"*, Eur. Phys. J. **C 27**, arXiv:hep-ex/0301017v1 (2003).

[Apo99] M. Apollonio et al.: *"Limits on Neutrino Oscillations from the CHOOZ Experiment"*, Phys. Lett. **B 466**, arXiv:hep-ex/9907037v1 (1999).

[Ard06] F. Ardellier et al.: *"Double Chooz: A Search for the Neutrino Mixing Angle θ_{13}"*, arXiv:hep-ex/0606025v4 (2006).

[Ard04] F. Ardellier et al.: *"Letter of Intent for Double-CHOOZ: A Search for the Mixing Angle θ_{13}"*, arXiv:hep-ex/0405032v1 (2004).

[Atm15] Atmel Corporation: *"Atmel 8-bit AVR Microcontroller with 2/4/8K Bytes In-System Programmable Flash"*, `http://www.atmel.com/images/atmel-2586-avr-8-bit-microcontroller-attiny25-attiny45-attiny85_datasheet.pdf` (2015).

[Bau11] C. Bauer et al.: *"Qualification Tests of 474 Photomultiplier Tubes for the Inner Detector of the Double Chooz Experiment"*, JINST **6** (2011) P06008 [arXiv:1104.0758 [physics.ins-det]].

[Ber12] J. Beringer et al. (Particle Data Group): *"Review of Particle Physics"*, Phys. Rev. **D 86**, 010001 (2012).

[Bil03] S. M. Bilenky: *"Neutrino oscillations in the framework of the three-neutrino mixing"*, arXiv:hep-ph/0307186v2 (2003).

[Bos15] Bosch Sensortec: *"BMP085 Digital pressure sensor - Data sheet"*, `https://www.adafruit.com/datasheets/BMP085_DataSheet_Rev.1.0_01July2008.pdf` (2015).

[Buc14] C. Buck: private communications (2014).

[Cea11] CEA Irfu (L. Scola): Picture taken from `http://irfu.cea.fr/en/Phocea/Album/popup.php?Affiche=1814` (2011).

[Cea10] CEA Irfu (L. Colombel): Picture taken from `http://irfu.cea.fr/en/Phocea/Album/popup.php?Affiche=1818` (2010).

[Dan62] G. Danby et al.: *"Observation of High-Energy Neutrino Reactions and the Existence of Two Kinds of Neutrinos"*, Phys. Rev. Lett. **9**, 36-44 (1962).

[Dav68] R. Davis, Jr. et al.: *"Search for neutrinos from the sun"*, Phys. Rev. Lett. **20**, 1205 (1968).

[Dec94] Y. Declais et al.: *"Study of reactor anti-neutrino interaction with proton at Bugey nuclear power plant"*, Phys. Lett. **B338**, 383 (1994).

[Don01] DONUT Collaboration: *"Observation of Tau Neutrino Interactions"*, Phys. Lett. **B 504** (2001), arXiv:hep-ex/0012035v1 (2000).

[Eid04] S. Eidelman et al.: *"Particle Data Group - The Review of Particle Physics"*, Phys. Lett. **B 592** (1) (2007).

[End15] Endress+Hauser Messtechnik GmbH: *"Operating Instructions Proservo NMS5/7 Series"*, `https://portal.endress.com/wa001/dla/5000233/0173/000/00/BA1001N08en04.09.pdf` (2015).

[Fei82] F. von Feilitzsch et al.: *"Experimental beta-spectra from ^{239}Pu and ^{235}U thermal neutron fission products and their correlated antineutrino spectra"*, Phys. Lett. **B118**, 162 (1982).

[Fir96] R.B. Firestone and V.S. Shirley: *"Table of Isotopes"*, John Wiley & Sons, 8th edition (1996).

[Fra11] M. Franke: *"Das Neutrino Experiment Double Chooz und erste Datenanalyse mit dem fernen Detektor"*, diploma thesis (2011).

[Gan13] A. Gando et al.: *"Reactor On-Off Antineutrino Measurement with KamLAND"*, Phys. Rev. **D 88** (2013) 3, 033001 [arXiv:1303.4667 [hep-ex]].

[Haa14] N. Haag et al.: *"Experimental Determination of the Antineutrino Spectrum of the Fission Products of ^{238}U"*, Phys. Rev. Lett. **112**, 122501 (2014).

[Hah89] A. Hahn et al.: *"Antineutrino spectra from ^{241}Pu and ^{239}Pu thermal neutron fission products"*, Phys. Lett. **B218**, 365 (1989).

[Hal84] F. Halzen and A.D. Martin: *"Quarks & Leptons"*, John Wiley & Sons, 1st edition (1984).

[Har15] T. Harbaum: Project description on `http://www.harbaum.org/till/i2c_tiny_usb/index.shtml` (2015).

[Hbm15a] HBM Deutschland: *"Z6... Load cell - Data sheet"*, http://www.hbmdoc.com/fileadmin/mediapool/hbmdoc/technical/b1010.pdf (2015).

[Hbm15b] HBM Deutschland: *"DWS2103 Digital scale display - Operating Manual"*, http://www.sensor-hbm.com/upload/product-file/i2935.pdf (2015).

[Hof12] M. Hofmann: *"Liquid Scintillators and Liquefied Rare Gases for Particle Detectors"*, PhD thesis (2012).

[Hub03] P. Huber: *"Reactor Neutrino Experiments Compared to Superbeams"*, Nucl. Phys. **B 665**, arXiv:hep-ph/0303232v2 (2003).

[Kaj99] T. Kajita et al.: *"Atmospheric neutrino results from Super-Kamiokande and Kamiokande: Evidence for ν_μ oscillations"*, Nucl. Phys. Proc. Suppl. **77** 123, arXiv:hep-ex/9810001 (1999).

[Key15a] Keyence Corporation: Product description on http://www.keyence.de/products/process/pressure/ap-v40/models/ap-47/index.jsp (2015).

[Key15b] Keyence Corporation: Product description on http://www.keyence.com/products/sensor/fiber-optic/fu/models/fu-93z/index.jsp (2015).

[Lan07] M. L'Annunziata: *"Radioactivity: Introduction and History"*, Elsevier Science, 1st edition (2007).

[Mak62] Z. Maki et al.: *"Remarks on the Unified Model of Elementary Particles"*, Prog. Theor. Phys. Vol. **28** No. **5**, 870-880 (1962).

[Mat11] T. Matsubara et al.: *"Evaluation of 400 low background 10-in. photomultiplier tubes for the Double Chooz experiment"*, Nucl. Instrum. Meth. **A 661**, 16 (2011) [arXiv:1104.0786 [physics.ins-det]].

[Max15] maxim integrated: *"DS1307 64 x 8, Serial, I^2C Real-Time Clock"*, http://datasheets.maximintegrated.com/en/ds/DS1307.pdf (2015).

[Mel15] MEL: *"M10L/100 Laser Abstands-Sensor"*, http://new.melsensor.com/subversion/mel/Optische-Sensoren/pdf/DB-M10.pdf (2015).

[Mep05] O. Meplan et al.: *"Nuclear power for the XXIst century: from basic research to high-tech industry"*, in ENC 2005: European Nuclear Conference (2005).

[Nak11] K. Nakamura et al. (Particle Data Group): *"Review of Particle Physics"*, J. Phys. **G 37**, 075021 (2011).

[Nea09] Nuclear Energy Agency: *"NEA-1845 MURE"*, `http://www.oecd-nea.org/tools/abstract/detail/nea-1845` (2009).

[Nob15] Royal Swedish Academy of Sciences: *"Scientfic Background on the Nobel Prize in Physics 2015"*, `https://www.nobelprize.org/nobel_prizes/physics/laureates/2015/advanced-physicsprize2015.pdf` (2015).

[Nov15a] P. Novella: *"DCIII nGd Candidates: Blessed Plots"*, internal document on Double Chooz DocDB (2015).

[Nov15b] P. Novella: private communications (2015).

[Oli14] K. Olive et al. (Particle Data Group): *"2014 Review of Particle Physics"*, Chin. Phys. **C 38**, 090001 (2014).

[Pau30] W. E. Pauli: *"Offener Brief an die Gruppe der Radioaktiven bei der Gauvereins-Tagung zu Tübingen"*, CERN archive transcription, `http://cdsweb.cern.ch/record/83282/files/meitner_0393.pdf` (1996).

[Pfa12] P. Pfahler: *"Realization of the low background neutrino detector Double Chooz: From the development of a high-purity liquid & gas handling concept to first neutrino data"*, PhD thesis (2012).

[Ptb14] Physikalisch Technische Bundesanstalt: Information system on `http://ptb.de/cartoweb3/SISproject.php` (2014).

[Ras13] Raspberry Pi Foundation: Product description on `https://www.raspberrypi.org/products/model-b/` (2013).

[Rec33] H. Rechenberg: *"Werner Heisenberg - Die Sprache der Atome"*, Part 5 / Epilog 1933: Die Brüsseler Konferenz und der Nobelpreis, p. 935 (2009).

[Rei56] F. Reines and C. Cowan: *"Detection of the Free Neutrino"*, Phys. Rev. **90**, 830-831 (1956).

[Sch85] K. Schreckenbach et al.: *"Determination of the antineutrino spectrum from ^{235}U thermal neutron fission products up to 9.5 MeV"*, Phys. Lett. **B160**, 325 (1985).

[Sha14] R. Sharankova: *"Vertex reconstruction resolution study"*, internal document on Double Chooz DocDB (2014).

[Sno02] SNO Collaboration: *"Direct Evidence for Neutrino Flavor Transformation from Neutral-Current Interactions in the Sudbury Neutrino Observatory"*, Phys. Rev. Lett. **89**, arXiv:nucl-ex/0204008v2 (2002).

[Sts15] STS Sensors: *"Pressure & temperature depth/level transmitter ATM/N/T"*, `http://www.sts-sensors.com/us/LinkClick.aspx?link=ATM_N_T_B.pdf&tabid=400&mid=896` (2015).

[Stu13] A. Stücken: *"Trigger Efficiency Distribution of Singles"*, internal document on Double Chooz DocDB (2013).

[Tos01] T. Toshito: *"Super-Kamiokande atmospheric neutrino results"*, arXiv:hep-ex/0105023v1 (2001).

[Vog99] P. Vogel and J. F. Beacom: *"The angular distribution of the reaction $\bar{\nu}_e + p \to e^+ + n$"*, Phys. Rev. **D 60**, arXiv:hep-ph/9903554v1 (1999).